

DETERMINATION OF STELLAR PARAMETERS FOR M-DWARF STARS: THE NIR
APPROACH

by

Daniel Thaagaard Andreasen

A thesis submitted in conformity with the requirements
for the degree of Doctor of Philosophy
Graduate Department of Departamento de Física e Astronomia
University of Porto

© Copyright 2017 by Daniel Thaagaard Andreasen

Dedication

*To Linnea, Henriette, Rico, and Else
For always supporting me*

Acknowledgements

When doing a PhD it is important to remember it is more a team effort than the work of an individual. This is something I learned quickly during the last four years. Therefore there are several people I would like to thank.

First and most importantly are my two supervisors, Sérgio and Nuno. They were after me in the beginning of my studies because I was too shy to ask for help; something that I quickly learned I needed to do. They always had their door open for me and all my small questions. It goes without saying that I am thankful for all their guidance during my studies. However, what I am most thankful for is the freedom I have had to explore paths and ideas on my own, and with them safely on the sideline. This sometimes led to failures and dead ends, but it made me grow as a researcher both by learning from my mistakes, but also by prioritising my time.

When I thank Sérgio and Nuno, my official supervisors, I also have to thank Elisa. She has been my third unofficial supervisor almost from the first day. Although she did not have any experience with NIR spectroscopy, she was never afraid of giving her opinion and trying to help. Elisa, your kindness, calmness, and help is priceless! It is extremely reassuring to go on this adventure with three capable supervisors ready to help at any time.

While Sérgio, Nuno, and Elisa are all very capable, they were not alone to answer all my technical questions. Often I went to Vardan to discuss science. Vardan's knowledge is immense, and it has been a pleasure to receive advice and answers when necessary. Similar has the support from Maria in my first two years been valuable. She was my friend here when I arrived, and the one I went to in the beginning with small questions since I was too shy to go with "stupid" questions to my supervisors. Thanks for all the answers you both gave me and the fruitful collaborations.

Luckily my time here in Porto has not only been about work. I have had a lot of good times with new and old friends here. In a random order I would like to thank Elisa, Maria, João, Jorge, Bárbara, Jason, Vardan, Mahmoud, Guilherme, Giancarlo, Andressa, Luisa, Solène, and the entire football team.

A very special thank you to Sofia who made my life easier here in Portugal, and has been a fantastic support and friend. All your time and effort will never be forgotten, and I appreciate all you have done for me.

Now, I know being abroad has been difficult but exciting for me. However, it has mostly been difficult for my family home in Denmark. The last part is specifically dedicated to them: Tusind tak for al jeres tålmodighed, mine kære venner og familie i Danmark. Jeg ved jeg ikke altid har været den bedste til at sende et par beskeder hjem, men alligevel har I altid mødt mig med kram når I har hentet mig i lufthavnen. Det har været en svær tid for mig her, og at tænke på jer derhjemme har virkelig holdt mig mod oppe! Jeg vil i sær gerne takke mine søstre, Henriette og Linnea for altid at have tid til at sludre lidt. Det samme gælder Rico, som også har hentet mig et par gange i lufthavnen. Selvfølgelig bliver jeg nødt til at sige tak til min kære mormor. Din støtte har været uden lige. Der har også altid været mange venner derhjemme som har fundet tid til at bruge et par timer med mig. Tusind tak til i sær Ole, Jesper, Ellen Marie, Maria, Ditte, og Sabrina.

Tusind tak alle sammen/thank you very much everybody!

Abstract

In this thesis, I describe the process of deriving stellar atmospheric parameters for FGK stars using high resolution and high signal-to-noise ratio near-IR spectra. The effort presented here is the first step towards analysing the cooler and more atmospheric complex M stars. Our own galaxy, The Milky Way, consist of around 75% M stars, thus studying these stars is a study of the galaxy: galactic archaeology. Additionally, these stars are prone to form low-mass rocky planets, making them ideal targets for habitable Earth-like planets.

In Chapter 2 and 3 I will introduce the theory needed for spectroscopic analysis and the methodology for the actual study. Especially in Chapter 3 I will present an automatic tool for deriving stellar atmospheric parameters, **FASMA**. This tool can derive parameters for solar-type stars in both the optical and the NIR and is used throughout the thesis.

After setting up the theory and methodology I will in Chapter 4 present the results from my studies in the NIR. These will start with a compilation of a NIR iron line list used for the spectroscopic analysis. This is then used to successfully study four stars with varying spectral type; the Sun, one hotter than the Sun, and two cooler. Due to lack of NIR spectra, I choose to analyse some synthetic spectra as well which is also presented in Chapter 4.

Part of the thesis was dedicated to the continuous update of SWEET-Cat, a database of planet host stars. This lead to a paper presenting 50 planet host parameters derived in a homogeneous and consistent way. The analysis of 50 planet hosts is followed by another work discovering two giant planet populations; a study I was part of.

With this thesis, another few pieces has been put in the NIR spectroscopy puzzle, preparing for the next pieces as well, which will be the study of M stars. This will then lead to the studies of the tinniest rocky planets to the galaxy.

Resumo

Algo sobre estrelas. Não sei. Eu não sou Portugues...

Contents

List of Tables	viii
List of Figures	x
1 Introduction	1
1.1 Exoplanets	2
1.1.1 Detecting exoplanets	2
1.1.1.1 Transit method	2
1.1.1.2 Radial velocity method	6
1.1.1.3 Other techniques	8
1.1.2 Towards an Earth twin	10
1.1.2.1 Detecting biosignatures on an exoplanet	11
1.2 Planet host stars	12
1.2.1 Star-planet correlations	16
1.3 Applications from knowing the stars	17
1.4 This thesis	17
2 Theory of stellar spectroscopy in a nutshell	19
2.1 Stellar atmosphere	19
2.1.1 Atmosphere models	22
2.1.2 Radiative transfer code - MOOG	22
2.1.3 The equivalent width	22
2.1.3.1 Temperature dependence	23
2.1.3.2 Pressure dependence	24
2.1.3.3 Abundance dependence	26
2.1.3.4 Microturbulence	26
3 Deriving stellar parameters	30
3.1 Photometry	30
3.1.1 InfraRed Flux Method - IRFM	30
3.1.2 T_{eff} -colour-[Fe/H] calibration	31
3.1.3 Asteroseismology	32

3.2	Spectroscopy	33
3.2.1	Synthesis	34
3.2.2	The EW method and FASMA	34
3.2.2.1	Ingredients	35
3.2.2.2	Wrapper for ARES	35
3.2.2.3	Interpolation of atmosphere models	36
3.2.2.4	Minimization	36
3.2.2.5	Error estimate	41
3.2.2.6	Testing FASMA	41
4	NIR spectroscopy of FGK stars - towards M stars	44
4.1	The creation of a NIR line list	46
4.1.1	Measuring the EWs and first filtering	46
4.1.2	Visual removal of lines	47
4.1.3	Synthetic investigation	47
4.1.4	Calibrating the line list: astrophysical $\log gf$ values	49
4.1.5	Removal of high dispersion lines	51
4.2	HD20010	52
4.3	The NIR line list - toward cooler stars	55
4.4	HD 20010 - revisited	58
4.5	Arcturus	58
4.6	10 Leo	59
4.7	Synthetic cool stars	61
5	SWEET-Cat	66
5.1	What is SWEET-Cat?	66
5.2	Data for 50 planet hosts	67
5.2.1	The data	67
5.2.2	Data collected from archive	68
5.3	Analysis of 50 planet hosts	68
5.3.1	Habitable zone	71
5.3.2	Changes to planetary parameters	72
5.3.2.1	HAT-P-46	74
5.3.2.2	HD 120084	74
5.3.2.3	HD 233604	75
5.3.2.4	HD 5583	75
5.3.2.5	HD 81688	75
5.3.2.6	HIP 107773	76
5.3.2.7	WASP-97	76
5.3.2.8	ω Serpentis (ome Ser)	76
5.3.2.9	ϕ Ursa Major (omi UMa)	76
5.4	Discovering two giant planet populations	77
5.5	Updating SWEET-Cat	80

6	Conclusions and future work	82
6.1	Conclusions	82
6.2	Future work	83
A	NIR line list	85
B	SWEET-Cat update of 50 planet hosts	88
C	FASMA and machine learning	93
	Bibliography	95

List of Tables

1.1	The median precision errors on the stellar atmospheric parameters for FGK planet hosts and M planet hosts as taken from SWEET-Cat.	14
3.1	Difference in derived parameters by Sousa et al. (2011) and FASMA. The second column is the mean difference with EWs measured by ARES in FASMA, while the third column is the mean difference using 20 randomly stars with the exact same EWs from Sousa et al. (2011).	43
4.1	Summary of the four stars used in this thesis. The stellar parameters are an average from the PASTEL catalogue (Soubiran et al., 2016) (see text for details), except the parameters for the Sun.	44
4.2	Selection of literature values for the atmospheric parameters for HD 20010. The mean and a 3σ standard deviation is presented at the end of the table from the literature values included, which was used as a reference for the derived parameters.	52
4.3	The derived parameters for HD20010 with and without fixed surface gravity.	54
4.4	Results for the three stars where first set of parameters are the literature values as presented in Table 4.1, second set of parameters are results with $\log g$ set to the same value during the minimization procedure as found in the literature (fixed), and last set of parameters are with all parameters free during the minimization procedure.	58
5.1	Columns in SWEET-Cat	67
5.2	Spectrographs used for this paper with their spectral resolution, wavelength coverage, and mean S/N from the spectra used.	68
5.3	Host star and planetary properties of GJ 785, HD 37124, and KELT-6; all which have an exoplanet in the habitable zone.	71
A.1	The NIR iron line list. The $\log g$ are calibrated with FASMA using the ATLAS9 model atmospheres by Kurucz (1993).	85
A.1	continued.	86
A.1	continued.	87
B.1	Derived parameters for the 50 stars in our sample. The S/N was measured by ARES.	88
B.1	continued.	89
B.1	continued.	90

B.2 Previous parameters from SWEET-Cat.	91
B.2 continued.	92

List of Figures

1.1	Confirmed exoplanets with the derived masses (relative to Jupiter) and the semi-major axis. The position of Mercury, Earth, and Jupiter are also shown, however the symbols are not to scale. The size of the symbols for the different detection methods are different in order to clearly see the methods which did not yet detect many exoplanets such as <i>Imaging</i> or <i>Astrometry</i> . Note that the masses discovered solely by the radial velocity (RV) method are the minimum masses. The data is from http://exoplanet.eu	3
1.2	<i>Upper plot</i> : The lightcurve of a star with an exoplanet transiting. <i>Lower plot</i> : The phase folded curve of the above lightcurve using the period of 3.259 days.	4
1.3	Period and radius of all exoplanets discovered by the transit method from the http://exoplanet.eu database. The desert at high-period/low-radius is clearly evident here. This is where an Earth twin would be found around a Sun twin.	5
1.4	<i>Upper panel</i> : RV time series of K2-29 b from the SOPHIE spectrograph. <i>Lower panel</i> : Phase curve of the time series above, using the period of 3.259 days. The fit is a simplistic sinusoidal for visual guidance.	7
1.5	A model of the Rossiter-McLaughlin effect on a phase folded RV time series. This is a simple circular prograde orbit.	8
1.6	The mass of exoplanet since the detection of the first exoplanet until now. The horizontal lines indicate the mass of Jupiter (upper), Neptune (middle), and Earth (lower).	10
1.7	The effective temperature of all host stars are shown against the luminosity. The colour represents the temperature, while the size of the symbols is a measure of the radius, or with other words, the evolutionary state. The smallest points are the dwarf stars. The green star in the plot show the location of the Sun.	13
1.8	Comparison between an optical and NIR part of the spectrum of HD 79210 obtained by the CARMENES spectrograph. This clearly illustrate why NIR spectra are preferred over optical spectra for cool stars, where absorption lines are less blended. HD 79210 is a K7 dwarf star.	15
1.9	Metallicity correlation for giant planets, comparing planet hosts and non host stars from the sample of Sousa et al. (2008) . It is clear that planet host stars have higher metallicities than non hosting stars. The histograms are normalised.	16
2.1	Energy levels for hydrogen, $E_n = \frac{-13.6 \text{ eV}}{n^2}$	21

2.2	An absorption line centred at λ_0 normalised at the flux level F_c . The area of the absorption line to the left is equal to the blue shaded area in the rectangle to the right with width EW.	23
2.3	The EW for a Fe I and Fe II line with increasing T_{eff} . The two lines have similar EW in the Sun and are found in the optical part of the spectrum. The vertical line show the solar T_{eff} .	25
2.4	<i>Upper panel:</i> Curve of growth for same Fe II used in Figure 2.3 for four different $\log g$ values. Here it is the weak lines mostly affected by the change in $\log g$. <i>Lower left panel:</i> Synthetic spectra of the same line. The colour scale is the same. <i>Lower right:</i> The abundance for the line at different $\log g$. A strong correlation (0.40) is seen.	27
2.5	<i>Upper panel:</i> Curve of growth of the same Fe I line as used in Figure 2.3. Four points are marked which is shown in the <i>lower panel</i> as a synthetic spectral line. The RW (proxy for EW) is clearly increasing with abundance.	28
2.6	Curve of growth for three different values of ξ_{micro} . The EW is increasing with increasing ξ_{micro} .	29
3.1	Measured and calculated flux from the Sun at infrared wavelengths. Data from Table 2 in Blackwell and Shallis (1977). Mean solar radius from this data is $1.011R_{\odot}$, and mean solar $T_{\text{eff}} = 5963 \text{ K}$ using Equation 3.3.	31
3.2	Mass and radius from asteroseismic scaling relation. The colour is the mass and radius for the upper and lower panel, respectively. The location of the Sun is added for reference.	33
3.3	Model atmosphere grid from Kurucz (1993) at $[\text{Fe}/\text{H}] = 0.00$ between 3000 K and 10 000 K. The grid extends to higher T_{eff} , but these are not considered in this thesis.	37
3.4	The abundances of Fe I for the planet host star: HATS-1. Upper plot: Converged parameters (see text for stellar parameters for this star). Middle plot: Converged parameters with 0.5 km/s added to ξ_{micro} . Lower plot: Converged parameters with 500 K added to T_{eff} .	38
3.5	ξ_{micro} dependence on T_{eff} and $\log g$ for a sample of 583 stars.	40
3.6	Overview of the minimization for FASMA. Credit: Andreasen et al. (2017b).	41
3.7	Stellar atmospheric parameters derived by FASMA compared to the sample by Sousa et al. (2011). The x-axis in all plots shows the results from FASMA, while the y-axis shows the parameters derived by Sousa et al. (2011).	42
4.1	Spectrum of HD 20010 (blue), the Sun (orange) 10 Leo (green), and Arcturus (red) in two different spectral regions. The spectra are all normalised to 1, but the flux of HD 20010, the Sun, and 10 Leo is added with 0.2, 0.4, and 0.6, respectively, for visual effect. The <i>upper</i> panel is part of the J band, while the <i>bottom</i> panel is part of the H band.	45
4.2	Solar spectrum (blue) with all iron lines in the spectral region (green) and other elements (orange). The depths and transparencies of the vertical lines are a measure of the line strengths (see Equation 4.1 for details). This is a case where the iron line is discarded due to blending, which is clear in the left wing of the central absorption line.	48

4.3	The three coloured curves represent different iron abundance, $\{-0.20; 0.00; 0.20\}$ compared to solar abundance. The grey curve is the solar atlas for reference. In this case the iron line at $15\,550.439\,\text{\AA}$ was investigated. <i>Upper panel</i> : Synthetic spectra were computed using the full VALD line list in the spectral range for the three different iron abundances. <i>Lower panel</i> : Same as the upper panel, but with the iron line removed from the line list. Since the synthetic spectra shows no features at this absorption line anymore, it is a fair assumption to say the iron line is the cause of this absorption line.	49
4.4	Line abundance of all iron lines before calibrating the $\log gf$ values. The green points are the points with a deviation less than 1.0 dex from the solar iron abundance. All the red points are discarded. The horizontal line shows the solar iron abundance.	50
4.5	The most disperse lines. <i>Upper panel</i> : The MAD versus the original EW. The red points are the outliers which were discarded during this process. <i>Lower plot</i> : Same as above with the de-trended MAD by the exponential fit as shown in the upper panel.	52
4.6	Line identification in piece of Arcturus spectrum with PHOENIX model and telluric model for correcting RV.	54
4.7	Difference in abundance for HD 20010 when multiple measurements of EW were obtained. The differences are between the lowest and highest measured EW in case of multiple measurements. This is shown against the wavelength (<i>upper panel</i>) and in a histogram (<i>lower panel</i>).	55
4.8	Comparison of the EW from the first version of the line list (measured with ARES), EW_1 , and the second version, EW_2 (measured with IRAF). The EWs are generally higher in the second version, with an average difference between the two version of $(2.1 \pm 11.1)\text{ m\AA}$. The three horizontal lines show the average value and the standard deviation.	57
4.9	Top figure: Difference of the automatic EW measurements between the summer observations and winter observations from the Arcturus spectra. Bottom figure: Same as above, but with manual measurements from ARES (summer) and automatic measurements (summer).	60
4.10	Derived parameters of 12 synthetic PHOENIX spectra with varying T_{eff}	62
4.11	Derived parameters of 12 synthetic PHOENIX spectra with varying T_{eff} . Here $\log g$ is fixed at 4.5 dex and ξ_{micro} fixed according to an empirical relation, thus only deriving T_{eff} and $[\text{Fe}/\text{H}]$	63
4.12	Common EWs between Arcturus and the synthetic spectrum with closest parameters (see text for details). The EWs are getting more disperse with increasing EW which is expected when seeing the direct comparison of the spectrum in Figure 4.13.	64
4.13	Comparison between the Arcturus atlas and a PHOENIX synthetic spectrum with similar parameters to Arcturus (see text for details).	64
4.14	Derived $[\text{Fe}/\text{H}]$ with respect to the true T_{eff} for runs that reached convergence. <i>Top panel</i> : $\log g$ fixed at 4.5 dex and ξ_{micro} to the empirical relation (see text for details). <i>Lower panel</i> : All parameters free.	65
5.1	A Hertzsprung-Russell diagram of the sample of 50 planet host stars added to SWEET-Cat. The parameters were derived using optical high resolution and high S/N spectra in tandem with FASMA and an optical line list. The colour scale shows the derived $\log g$ for each star.	69
5.2	The new atmospheric parameters of 50 exoplanet hosts against the previous parameters.	70

5.3	The habitable zone for the updated SWEET-Cat stars. The coloured line shows the theoretical habitable zone, while the dots shows the location of the planets in the actual system. The blue lines show the habitable zone of the three stars where a planet is located within it (green points). The red dots and orange lines are systems which does not lie within the habitable zone. Finally, the green line shows the location of the Sun’s habitable zone and the first five planets placement. In this model both Earth and Mars are within the habitable zone.	72
5.4	Stellar radius on both axes calculated based on Torres et al. (2010) . The x-axis shows the stellar radius based on the atmospheric parameters from the literature, while the y-axis indicates the new homogeneous parameters presented here. The colour and size indicate the surface gravity. This clearly shows that the disagreement is biggest for more evolved stars.	73
5.5	Giant planet masses for the full sample and constrained sample (see text for details). This study was performed by Santos et al. (2017) to distinct two giant planet populations. . . .	78
5.6	[Fe /H] distributions for the lowest and highest exoplanet masses. These are divided into different stellar mass ranges.	79
C.1	Mean absolute error on each parameter after 1000 runs.	94

Chapter 1

Introduction

Every atom in your body came from a star that exploded. And, the atoms in your left hand probably came from a different star than your right hand. It really is the most poetic thing I know about physics: You are all stardust.

Lawrence M. Krauss

Ever since the dawn of time, the humankind have looked at the stars and wondered if we are alone in this Universe. To answer this question, one must look toward the field of extrasolar planets (exoplanets). This is a rapidly growing field in astronomy and science in general. Ever since the first confirmed discovery of an exoplanet around a millisecond pulsar in 1992 by [Wolszczan and Frail \(1992\)](#) and three years later, exoplanet 51 Peg b was discovered around a solar-type star by [Mayor and Queloz \(1995\)](#), more than 3600 exoplanets have been discovered at the time of writing, July 2017¹.

With the discoveries of exoplanets, the main focus of observational exoplanetology is now mainly on finding a twin of Earth; that is a planet that can harbour life as we know it. An Earth twin will be of similar size (both in mass and radius), and be located in a distance from its host star where liquid water may exist on the surface. When speaking of detecting similar life as we know it, it is important to note that it is the biosignatures that life will cause on the exoplanet's atmosphere that the astronomers are and will be looking for. These biosignatures are the subtle changes life can cause on its host planet's atmosphere. Generally we refer to e.g. animals here on Earth which produce carbon-dioxide, while plants produce oxygen. Before even start the search for these biosignatures on another exoplanet, the exoplanet must be carefully characterised so we do not end up looking blindly for the biosignatures. Such a search will be extremely costly. Additionally, it may not be necessary to find an Earth replica in order to find conditions for life (see e.g. [Alibert \(2014\)](#) for a discussion on habitable planets unlike the Earth). Lastly, are the compositions and origins interesting in this era of exoplanetary science. However, in order to accurately and precisely characterise an exoplanet, it is crucial to characterise its host star. This is commonly known as “know the star, to know the exoplanet”. It is only possible to obtain planetary global parameters such as its radius and mass if the stellar parameters are accurately known. With sufficiently high precision it is even possible to distinguish between different planetary bulk compositions

¹ <http://exoplanet.eu/>

such as water-worlds, rocky planets, gaseous planets, iron planets, or exotic combinations of the above (e.g. [Thiabaud et al., 2014](#); [Dorn et al., 2015](#)). [Dorn et al. \(2015\)](#) found that stellar elemental abundances (Fe, Si, Mg) are key to reduce the degeneracy in interior structure models and mantle composition.

In this chapter there will be a general introduction to exoplanets, detection methods, and characterisation (Section 1.1). Then a throughout introduction on the exoplanet host stars (Section 1.2), which is the main focus of this thesis. In the end of this chapter, the importance of stellar studies will be discussed along with its wide-spread applications (Section 1.3) before a general overview of this thesis (Section 1.4).

1.1 Exoplanets

The holy grail in the field of exoplanets is to find the first exoplanet with biosignatures. This is by no means an easy task. To give an idea of the difficulty of detecting biosignatures on an exoplanet, it is important to understand all the difficulties when simply detect and confirm the presence an exoplanet. This will shortly be described in the sections below where several detection techniques will be introduced.

1.1.1 Detecting exoplanets

There are six main techniques for detecting exoplanets around main sequence stars, some with advantages over others. These advantages depends strongly on the advancement of the instruments used for the different techniques, but also on the physical properties of the exoplanetary system. A lot of information about the exoplanets can be extracted when more than one of these techniques is used and combined. The success of the different methods can be seen in Figure 1.1. Here all the detected planets (with measured masses) are shown divided into which group was used for detecting the exoplanets into different detection methods. The most exoplanets are discovered with the transit method and the radial velocity method, both which will be explained in more detail below. Additionally, the figure also includes Mercury, Earth, and Jupiter (size of the symbols are not to scales) that are here presented as a reference for the comparison with the known exoplanets.

It is important to note, that different phenomena might mimic planetary signals, such as stellar activity, or the contaminating light from a fainter stellar companion (see e.g. [Queloz et al., 2001](#); [Oshagh et al., 2013, 2014](#)). However, they will not be described in this thesis. For more details on the description of these techniques see e.g. [Seager \(2010\)](#).

1.1.1.1 Transit method

The most successful method, if based on numbers of exoplanets detected, is the transit method. The way to use this method is to measure the integrated light of a star is continuously monitored in order to detect a transit. This kind of data is called a photometric time-series, and has wide applications in stellar astrophysics. It is not enough to monitor a star to detect a transiting exoplanet. It has to be aligned with the line of sight from the observer, thus the probability of detecting exoplanets depends on the geometry of the system.

Transit photometry is a well-known method in astronomy, however only used recently for detecting exoplanets. Before this, it has been used extensively for finding and characterising eclipsing binary stars. The difference here is, that the exoplanet is extremely small and does not radiate (or at least emit very little radiation compared with the host star). An example of an exoplanet transiting a star can be seen

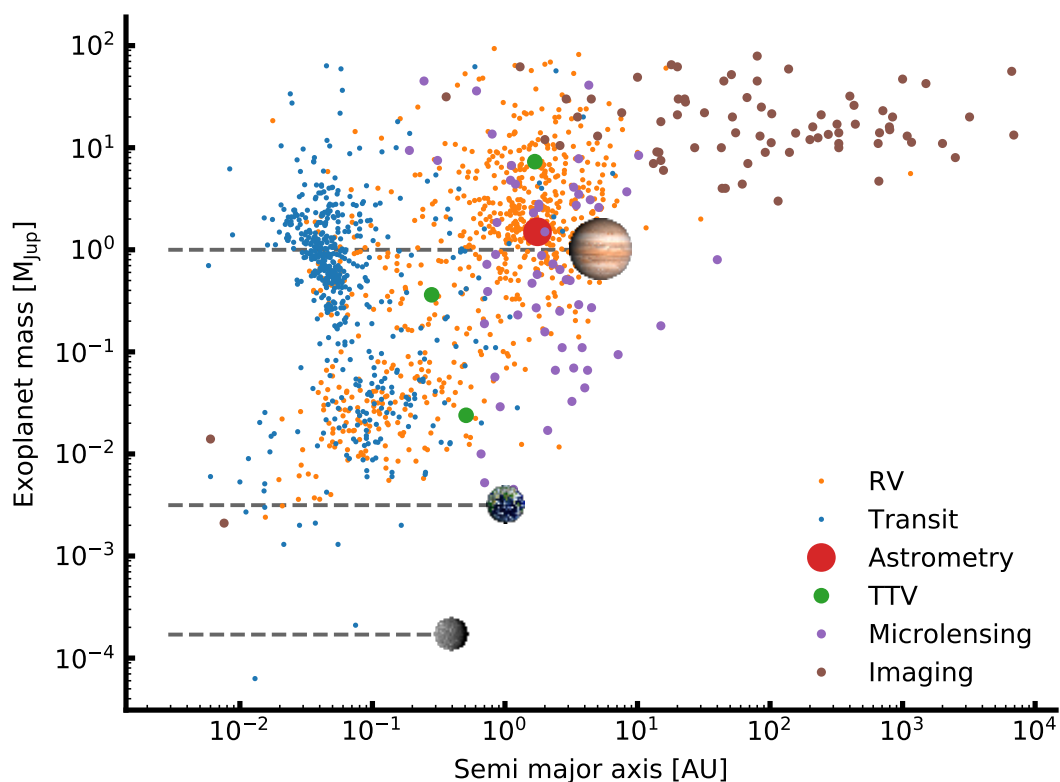


Figure 1.1: Confirmed exoplanets with the derived masses (relative to Jupiter) and the semi-major axis. The position of Mercury, Earth, and Jupiter are also shown, however the symbols are not to scale. The size of the symbols for the different detection methods are different in order to clearly see the methods which did not yet detect many exoplanets such as *Imaging* or *Astrometry*. Note that the masses discovered solely by the radial velocity (RV) method are the minimum masses. The data is from <http://exoplanet.eu>

in Figure 1.2 for K2-29 b. The data is from a summer school², which was prepared from Santerne et al. (2016).

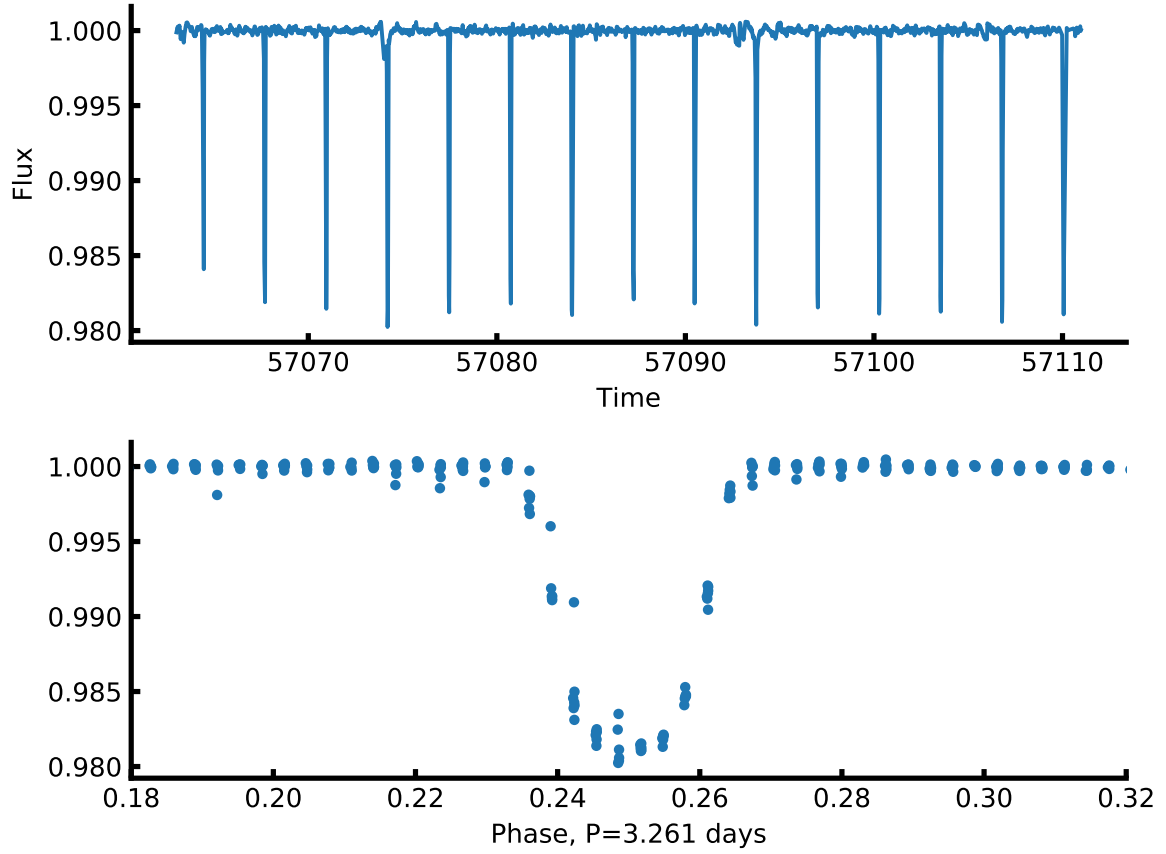


Figure 1.2: *Upper plot:* The lightcurve of a star with an exoplanet transiting. *Lower plot:* The phase folded curve of the above lightcurve using the period of 3.259 days.

When an exoplanet transits its host star, the total brightness observed from the system will decrease, as the exoplanet blocks some of the light from the star. This dimming in brightness will be seen periodically as the exoplanet orbits its host star. The decrease in brightness as the planet transit the star is directly related to the ratio between the stellar radius R_* and the planetary radius R_p :

$$k = \sqrt{\frac{R_p}{R_*}}, \quad (1.1)$$

where k is the depth of the transit compared to the normalised stellar brightness. This in turn means that the transit method is most sensitive to exoplanets with a large radius, and often in close orbits as these exoplanets are more likely to be aligned with the observer (us), and its host star. In Figure 1.3 all detected exoplanets with the transit method is shown. In particular the radius against the period (two parameters that will always be measured by this method). Especially due to the *Kepler* space mission, exoplanets with low radius have been found, but it is evident as the period for a exoplanet increases, the detectability decreases, hence the desert in the high-period/low-radius quadrant in the figure.

² Data can be found here: <https://github.com/iastro-pt/AzoresTE1>

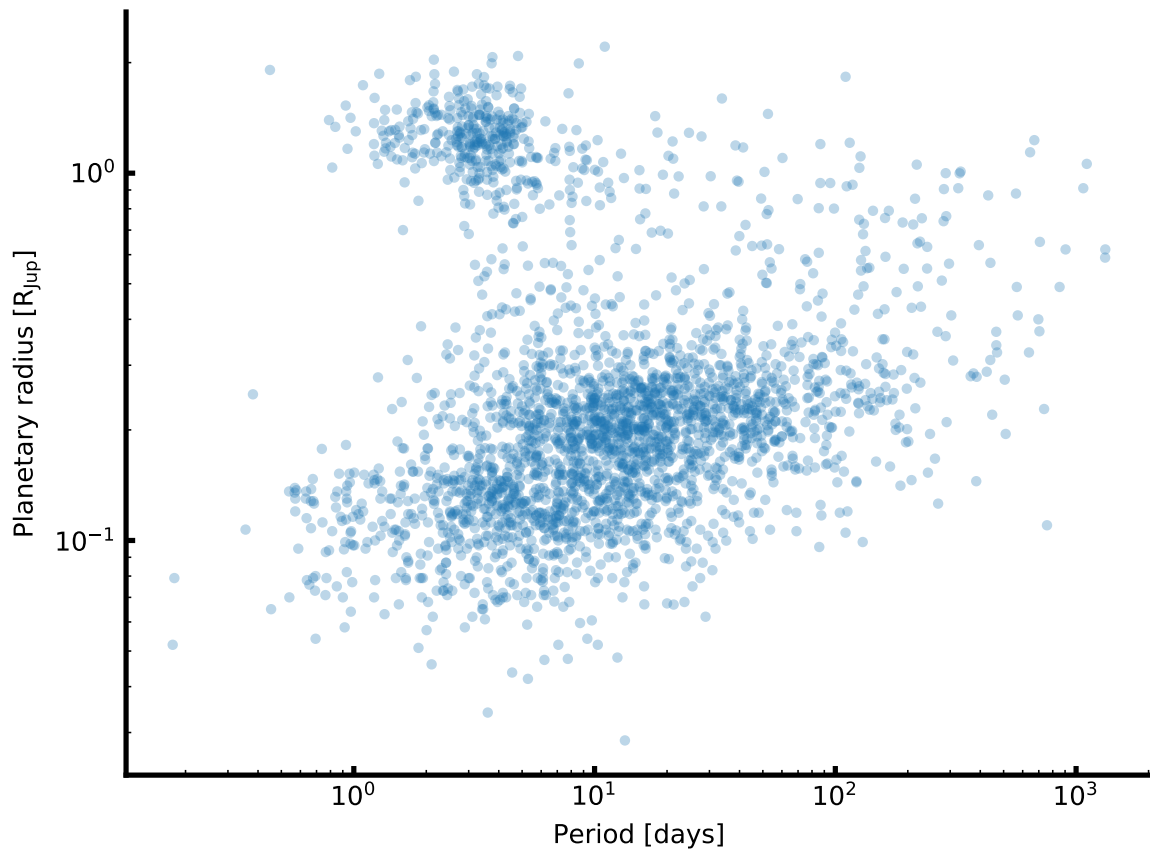


Figure 1.3: Period and radius of all exoplanets discovered by the transit method from the <http://exoplanet.eu> database. The desert at high-period/low-radius is clearly evident here. This is where an Earth twin would be found around a Sun twin.

This method allows to determine the radius of the planet as far as the radius of the star is known. Furthermore, detailed analysis of the phase curve³ of an exoplanet can additionally reveal the surface temperature of the exoplanet. The transit described above is also known as the primary transit. The secondary transit is when the exoplanet is behind its host star as seen from Earth. This lead to a faint dimming of the total brightness observed from the system. This dimming is due to the reflected light missing from the exoplanet and its self-irradiation caused by its surface temperature. It is difficult to observe secondary transits. This is mainly due to the low flux from the exoplanet compared to its host.

While transit photometry can be done from Earth, the best results are from space with e.g. *Kepler* (Borucki et al., 2010) and CoRoT (Baglin et al., 2006), while ground-based surveys have been successful as well, e.g. WASP (Pollacco et al., 2006), and HAT-P (Bakos et al., 2004) to mention just a few.

1.1.1.2 Radial velocity method

When an exoplanet orbits a star, they both orbit the centre of mass. Since the star is more massive than the exoplanet, the centre of mass is much closer to the star. The radial velocity method is the study of the motion of the host star around the centre of mass using the Doppler effect caused by an orbiting exoplanet⁴. This together with the transit method described above are by far the most successful methods to detect and characterise exoplanets with the current instruments. The periodic signal created by the exoplanet on the host star depends on the mass ratio between the star M_* and the planet M_p :

$$K = \frac{28.4329 \text{ m/s } M_p \sin i}{\sqrt{1-e^2} M_{\text{Jup}}} \left(\frac{M_* + M_p}{M_{\odot}} \right)^{-2/3} \left(\frac{P}{1 \text{ year}} \right)^{-1/3} \quad (1.2)$$

where K is the semi-amplitude of the sinusoidal, e is the eccentricity, i is the inclination of the orbital plane compared to the line of sight from Earth, P is the orbital period, and M_{Jup} is the mass of Jupiter. Since $M_* \gg M_p$, the term $M_* + M_p \simeq M_*$ in order to simplify the equation. The sinusoidal motion of the star can be seen in Figure 1.4 where both the time series and the phase curve is presented for the exoplanet, K2-29 b. The data used is from the same source as the lightcurve above in Section 1.1.1.1.

In order to apply the radial velocity method for detecting exoplanets, it is necessary to collect a time series of spectra in order to cover most part of the phase of the orbit. These spectra need to be obtained with high spectral resolution in order to obtain a high precision measurement of the RV. The RV is obtained when the observed spectrum is compared with a reference spectrum of the star at $RV = 0 \text{ km/s}$. The Doppler shift needed to be applied to the observed spectrum to cause the maximum overlap between the two spectra corresponds to the measured RV. The instrument needs to be stable for the same reason (see e.g. Bouchy et al., 2001). These spectra can be used for the analysis and characterisation of the host star if combined in order to increase the signal-to-noise (S/N). The spectra traditionally used for exoplanet detection have a high resolution, which typically is more than 50 000. The spectral resolution is key, as the precision is strongly dependent on this parameter.

The currently most precise radial velocity spectrographs are HARPS (ESO) (Mayor et al., 2003) and HARPS-N (La Palma) (Cosentino et al., 2012), able to achieve long term precision below 1 m/s (see e.g. Pepe et al., 2013).

Very interestingly the RV measurements might be used to detect what is known as the Rossiter–McLaughlin

³ A phase curve is here a light curve cut at every period of the planet and plotted on top of itself. This is equivalent to a single transit at a very high sampling rate

⁴ As the transit method, this method has been known for decades in the study of e.g. binary stars.

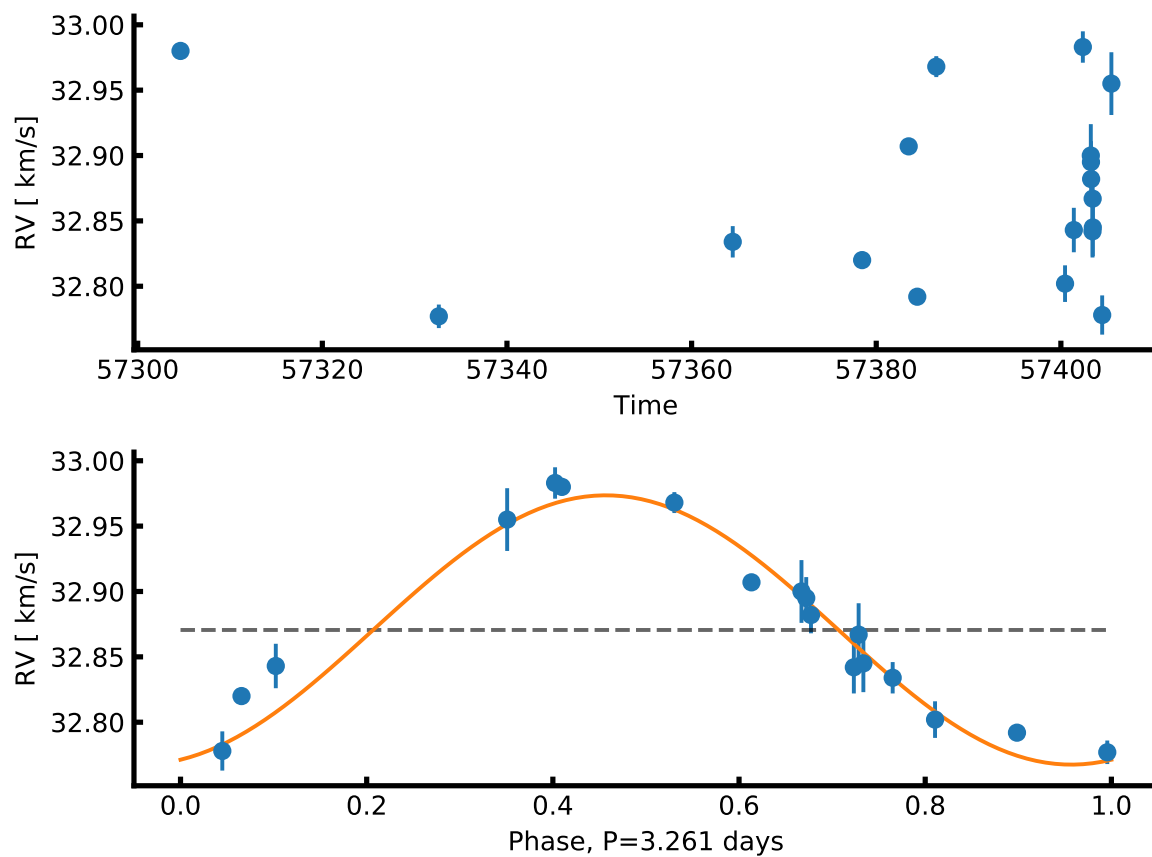


Figure 1.4: *Upper panel:* RV time series of K2-29 b from the SOPHIE spectrograph. *Lower panel:* Phase curve of the time series above, using the period of 3.259 days. The fit is a simplistic sinusoidal for visual guidance.

effect. This effect is a combination of two things. First, the rotation of the host star slightly cause a red-shift of one side (the side rotating away from us), while the other side of the rotating star is slightly blue-shifted. The net effect is zero. Second, if an exoplanet transit its host, it might block some of the blue-shifted light, thus the net effect will suddenly be ever so slightly red-shifted. While the exoplanet transit over the surface of the star the net effect will change from slightly red-shifted to slightly blue-shifted. This effect is used to determine the orbital configuration, i.e. the orbital inclination and whether the orbit is prograde or retrograde. This effect have been used in several studies (Winn et al., 2005; Triaud et al., 2010, to mention just a few). An illustration on how they RV phase curve might look like is illustrated in Figure 1.5.

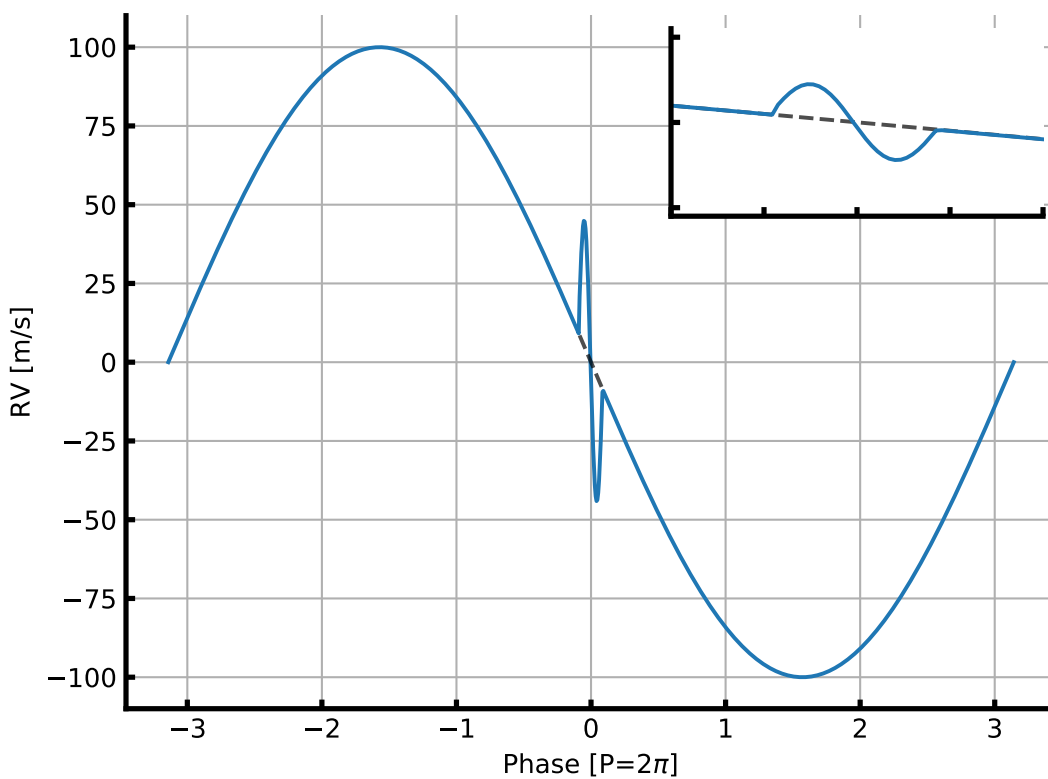


Figure 1.5: A model of the Rossiter-McLaughlin effect on a phase folded RV time series. This is a simple circular prograde orbit.

1.1.1.3 Other techniques

The following four techniques have all detected exoplanets, however, they are currently not widely used and neither have the same level of success as the two methods described above. This is something that will change in the future with new and up-coming instruments.

Direct imaging Direct imaging is probably the easiest method to understand, however it is quite difficult to actually use this technique due to the immense difference in luminosity between a star and

an exoplanet. In its core, by carefully blocking the light of a star, it is possible to directly image the exoplanets around it. However, it is extremely difficult to block the light of the host star and find the emitted light of the exoplanet(s) in orbit. One has to deal with residual light from the host star, which are orders of magnitudes brighter than the exoplanets. With SPHERE at VLT it is expected that more exoplanets will be found with this technique (Beuzit et al., 2008). The first exoplanet detection with SPHERE have already been made (Vigan et al., 2016; Bonnefoy et al., 2016; Apai et al., 2016; Maire et al., 2016; Zurlo et al., 2016, see e.g.).

Astrometry Astrometry is the measurement of the position of a star on the sky, i.e. its coordinates. The coordinates for a star may change over time due to its relative motion compared to our Solar System. Additionally, an exoplanet might cause minute changes in the coordinates due to the orbit of the star and exoplanet around the centre of mass. Using astrometry to detect exoplanets is very similar to the RV method described above in Section 1.1.1.2. The Gaia mission (Gaia Collaboration et al., 2016) will provide many exoplanets detected with astrometry. Perryman et al. (2014) estimates that $21\,000 \pm 6\,000$ high-mass ($1 - 15M_{\text{Jup}}$) long-period planets will be discovered to a distance of 500 pc with the Gaia mission for the nominal 5 year mission.

This technique is more sensitive to massive, long period exoplanets as they cause a larger motion compared to lighter, short period companions. See e.g. Figure 1 by Perryman et al. (2014) for the astrometric signatures produced by a range of exoplanets at different period.

Transit timing variation This technique of detecting exoplanets is a highly indirect method of detecting exoplanets. Here a transiting exoplanet has to be detected first as explained in Section 1.1.1.1. Then variations in the occurrence of mid-transit can be detected if a second non-transiting exoplanet interact with the primary transiting exoplanet (known as planet-planet interaction). This interaction will periodically cause the mid-transit to happen ahead/behind of the time if only one exoplanet would be present (Agol et al., 2005; Holman and Murray, 2005).

A careful analysis of the transit timing variations (TTV) can give the mass of the transiting exoplanet. Most of these exoplanets pairs which shows TTV are in an orbital resonance. This technique as well, is more sensitive to massive exoplanets as they will induce a higher signal. However, it is also sensitive to exoplanets with comparable semi-major-amplitudes.

Microlensing This technique is very exotic and not widely used, however since a few exoplanets have been discovered by this technique it deserves to be mentioned. The core theory in this technique is the well-known General Relativity by Einstein (1916). With this method an observer looks at a distant star as a star between the observer and the distant star passes in between the line of sight. The intermediate star will act as a lens and increase the magnitude of the distant star. This increase of magnitude will reach its maximum as the two stars are most aligned as seen from Earth.

To use this method for detecting exoplanet, there will have to be an exoplanet orbiting intermediate star. The exoplanet act as a microlens, momentarily make a secondary increase in magnitude. The amount of increase in magnitude is related to the mass of the exoplanet and its configuration in the orbit around its host star. The higher the mass, the higher the effect, however it is possible to detect quite low-mass exoplanets with this technique.

While this exotic technique is interesting and has detected exoplanets, it is not as useful as the RV and transit detection methods in individual studies of planets since it only occurs once. The stars observed

with this technique are often faint, thus making follow-up RV detection very difficult if not impossible with the current instruments.

1.1.2 Towards an Earth twin

The above mentioned techniques will be used to find an Earth twin. Especially will the two first techniques (transit and RV method) be the ones finding the smallest exoplanets as a wide range of instruments are being developed dedicated for this. Since the detection of the first exoplanet around a solar-type star by [Mayor and Queloz \(1995\)](#), the community has been able to detect lower mass exoplanets as seen in [Figure 1.6](#) and the regime of Earth-mass exoplanets have been reached very recently.

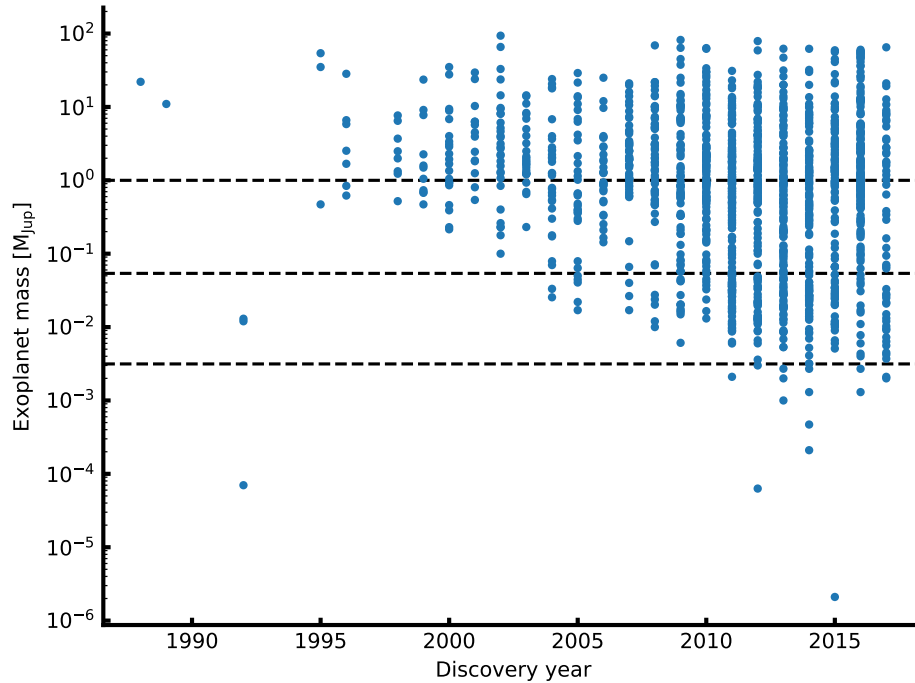


Figure 1.6: The mass of exoplanet since the detection of the first exoplanet until now. The horizontal lines indicate the mass of Jupiter (upper), Neptune (middle), and Earth (lower).

While the first many discoveries of exoplanets were the (at the time) exotic and strange hot Jupiter-like exoplanets in close orbits, the time have come to detect exoplanets with both lower mass and wider orbits. It is crucial to have high precision instruments and long surveys to detect these exoplanets. Missions as *Kepler* and *CoRoT* have been excellent for this, since they have focused on few fields of the sky for a long time.

The first place to naively look for a Earth's twin would be in a system similar to our own Solar system. That means around a G dwarf like our own Sun. However, due to the high surface temperature of these stars⁵, the habitable zone will be far from the host star (see e.g. [Kasting et al., 1993](#)). The habitable zone is the distance interval from a star where liquid water can be found. This zone is not only dependent on stellar parameters, but also on the atmospheres of exoplanets since a exoplanet with a dense atmosphere

⁵ Very few effort have been made to look for exoplanets around OB stars as these are both few in numbers and hostile environments for exoplanets.

can keep the heat, thus be further away from its host star and still have liquid water, compared to an exoplanet with a lighter atmosphere. Indeed, to detect a copy of our own Sun-Earth system we would need to detect the minute signature of an exoplanet in a 1 year orbit around its host star (a solar twin). For the RV method, this minute signature will be 10 cm/s, while the current level of precision is around 1 m/s. For photometry a precision of 100 ppm is required to detect an Earth sized planet around a solar-type star (Borucki, 2017). These signatures can be measured with the next generation of ultra stable high resolution spectrographs such as ESPRESSO (Pepe et al., 2010) and future photometric space missions such as PLATO (Rauer et al., 2014). If detected with the transit method, more than one transit is needed, hence this will take at least two years, and probably even longer. Moreover, this is all assuming that the geometry of the system aligns in such a way that a transit can even be seen from Earth. The endeavour to get the follow-up RV afterwards will also be extremely challenging with today’s technology, and only the next generation of instruments will be able to detect these signals. In conclusion, even with perfect instruments, it will take years to detect an Earth twin around a Sun-twin with the RV and transit methods.

Therefore, it is not a surprise that an effort has been towards detecting Earth-like planets around the lightest stars. These stars (M stars) are also cooler, hence the habitable zone will be closer to its host compared to the more massive and hotter stars (Kasting, 1997), and ultimately the period for habitable exoplanets will be shorter. The nature has been kind, since it seems that the M stars are prone to form rocky planets rather than giant gaseous planets (Bonfils et al., 2013; Delfosse et al., 2013). The shorter period means that the surveys can be shorter for these exoplanets. Moreover, since the host stars are smaller the signal from a transit will be easier to detect (see Equation 1.1). Similarly will the RV signal be larger for an Earth-like planet in the habitable zone around an M star compared to a similar exoplanet around a G star⁶. Both due to the lower period and due to the lower mass of the host star (see Equation 1.2).

While M stars seems to be the place to look for the Earth’s twin, there are still some challenges to tackle. Foremost is the detailed characterisation of the host star, which are particular troublesome for these stars. This is something that will be focused on in Section 1.2.

1.1.2.1 Detecting biosignatures on an exoplanet

The best hope to indirectly detect life is by finding biosignatures (Kasting and Siefert, 2002; Snellen et al., 2013, see e.g.) in the exoplanet’s atmosphere. Transmission spectroscopy and lightcurves in different pass bands are the techniques to study the atmosphere of exoplanets. For transmission spectroscopy a spectrum is obtained of the star during transit. This spectrum will thereby contain signals of the atmosphere of the transiting exoplanet. Later, a spectrum of the star can be obtained, e.g. during the secondary transit. The difference in these two spectra will reveal the exoplanetary spectrum. This was e.g. done by Charbonneau et al. (2002).

An interesting test to look for biosignatures from the Earthshine on the Moon was performed by Arnold et al. (2002) where they clearly see the blue colour of the Earth’s atmosphere due to Rayleigh scattering. This was done by obtaining a Moon spectrum and an Earthshine spectrum using the 80 cm telescope at OHP. They also observed signatures for oxygen, ozone, and water vapours; all important biosignatures in a planetary atmosphere supporting life.

⁶ For a solar twin, with an Earth twin at 1 AU the semi-amplitude will be close to 10 cm/s while it would be roughly 50 cm/s for an Earth twin around a $0.3M_{\odot}$ M dwarf at 0.1 AU.

These signatures, especially oxygen, are from microorganisms through photosynthesis (see e.g. [Kasting and Siefert, 2002](#)). However, there might be conditions outside the habitable zone which might sustain life. Here on Earth, extremophiles such as the water bears are known to thrive in extreme places such as boiling water, acid, ice, etc. This might eventually lead to a new window of opportunity in the search of extraterrestrial life ([Cavicchioli, 2002](#)).

1.2 Planet host stars

With the present diversity of exoplanets it becomes increasingly important to get an accurate and precise characterisation of the exoplanets in order to study them in samples and on an individual level. An accurate and precise characterisation can give us an idea whether the planet is rocky, composed of water, gaseous, or some other more exotic combination, by comparing fixed density profiles (based on different compositions) to the planetary mass and radius (see [Dorn et al., 2015](#), e.g.). As mentioned above, it is crucial to characterise the host stars in order to characterise the exoplanets. The host stars discovered so far are mainly FGK dwarf stars, although some are more evolved. This can be seen in Figure 1.7 where the effective temperature of all host stars are shown against the luminosity. The colour represents the temperature, while the size of the symbols is a measure of the radius, or with other words, the evolutionary state. The smallest points are the dwarf stars. The luminosity was derived combining the following equations:

$$g = \frac{GM}{R^2}$$

$$L = 4\pi R^2 \sigma T_{\text{eff}}^4,$$

into

$$\frac{L}{L_{\odot}} = \frac{M}{M_{\odot}} \left(\frac{T_{\text{eff}}}{5777 \text{ K}} \right)^4 10^{4.44 - \log g}, \quad (1.3)$$

where σ is Boltzmann's constant, G is Newton's gravitational constant, and $\log g$ is the surface gravity. The data for Figure 1.7 is obtained from SWEET-Cat⁷.

To make an in-depth characterisation of stars it is common to use several different methods to gain knowledge about different aspects of a star. If the effective temperature is needed, the reliable determination comes from the analysis of a high resolution and high signal-to-noise (S/N) spectrum or the infrared flux method (see Section 3.1.1 for more details). Spectroscopy is also used to identify chemical abundances of the photosphere of the star, while a method like asteroseismology⁸ is used to determine the mass and radius of a star with higher precision; two parameters crucial to characterise the orbiting exoplanet. More of these methods are described in greater detail in Chapter 3.

In the example given above, the effective temperature is needed before asteroseismology can be used to determine the mass and radius. In order to perform a successful detailed asteroseismic analysis a long time series is needed like the ones obtained from CoRoT and *Kepler* which are months and years long time series. The light curves provided by these dedicated missions are used both for the detection of exoplanets and stellar oscillation studies. Likewise will the spectra obtained from the RV method

⁷ <https://www.astro.up.pt/resources/sweet-cat/>

⁸ Asteroseismology is the study of stellar oscillations. See Section 3.1.3 for details on this method.

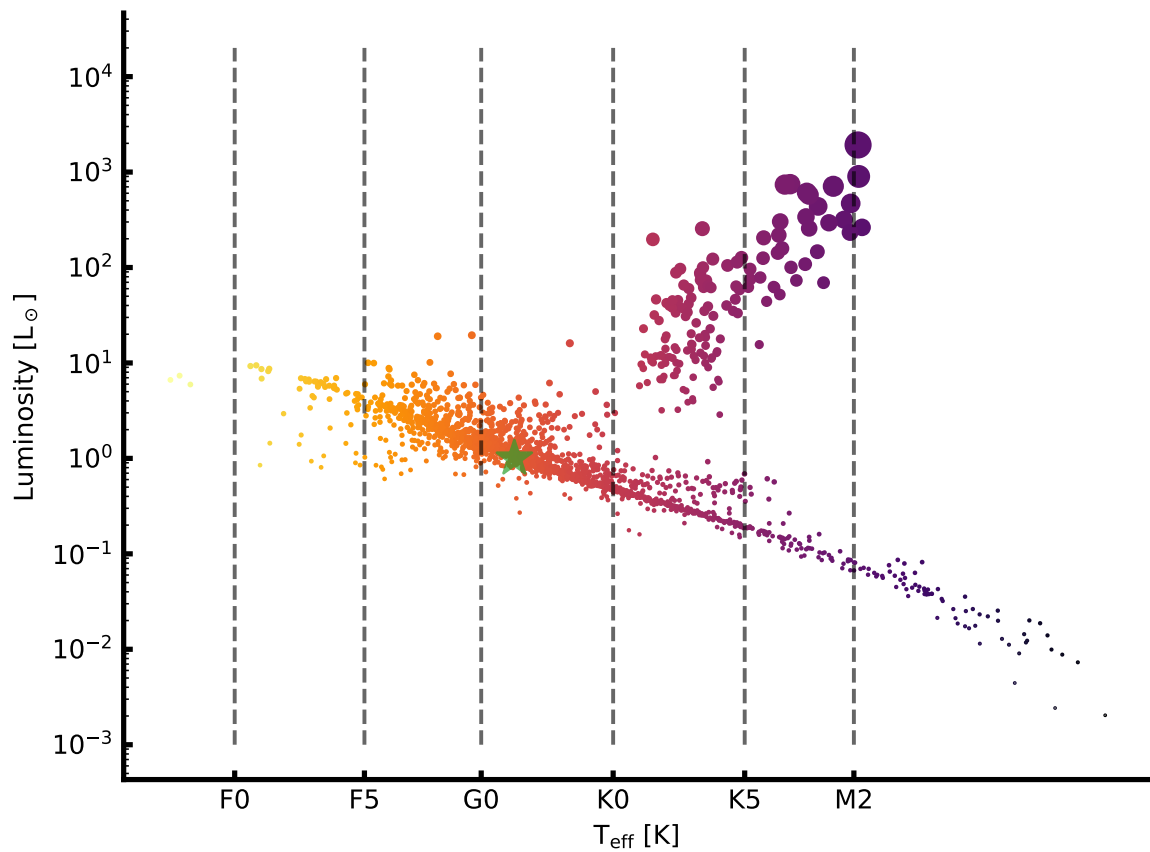


Figure 1.7: The effective temperature of all host stars are shown against the luminosity. The colour represents the temperature, while the size of the symbols is a measure of the radius, or with other words, the evolutionary state. The smallest points are the dwarf stars. The green star in the plot show the location of the Sun.

to detect/confirm an exoplanet be used for the stellar characterising afterwards by combining them to increase the S/N. This combined high S/N spectrum is ideal for the spectral analysis of stars.

The synergy between a spectroscopic analysis and asteroseismology have proven very successful (see e.g. Huber et al., 2013) for characterising an exoplanet system (host star and exoplanet). However, it does have its limitations. It can be difficult to detect solar-like oscillations as the stars get colder than the Sun. The community has yet to detect any solar-like oscillations in M dwarf stars (Rodríguez et al., 2016; Berdiñas et al., 2017). Many of the detected exoplanets are from the *Kepler* mission, where many of the host stars are very faint. While it is not impossible to make high resolution and high S/N spectroscopic observations, it is extremely time consuming. Therefore brighter targets are often prioritised, unless there is an exceptional case.

With the search for an Earth twin around the small cool M dwarf stars, it is important to develop reliable methods for the analysis of these stars. The methods to analysis typical planet hosts (FGKM stars) currently works best for the FGK dwarf stars compared to M dwarf stars. To illustrate this the median errors on the atmospheric parameters can be seen in Table 1.1. The parameters are from SWEET-Cat, and for the FGK stars only parameters analysed by the Porto group are presented. It is important to note that there are 138 M stars while there are 538 FGK stars (after only using stars analysed here). More details on SWEET-Cat will follow in Chapter 5.

Table 1.1: The median precision errors on the stellar atmospheric parameters for FGK planet hosts and M planet hosts as taken from SWEET-Cat.

Atmospheric parameter	FGK	M
$T_{\text{eff}}[\text{K}]$	44	60
$\log g[\text{cgs}]$	0.090	0.04
$[\text{Fe}/\text{H}]$	0.035	0.10

The detailed characteristics of M dwarfs are currently a problem, however, with the advance of NIR spectrographs this is slowly changing. It is general believed that a NIR analysis is needed to characterise M stars. The reason is simple that these stars are so intrinsic faint, that it is important to collect as much flux as possible. This happens in the NIR. Since M stars are intrinsically faint in the visible, it is advantageous to use NIR spectrographs where M stars emit most of their light. Moreover, for spectroscopic studies, the optical spectrum of these stars are severely contaminated by molecular absorption lines, which depress the continuum. It is crucial to get the continuum placement correct during spectroscopic studies. In the NIR the continuum depression is less severe, however still challenging. This can clearly be seen in Figure 1.8 where the optical and NIR part of the spectrum for HD 79210, a K7 dwarf star⁹, is plotted. The spectra were obtained by CARMENES simultaneously and have therefore the same exposure time. During a spectroscopic analysis, which will be the applied method in this thesis, it is important to observe isolated absorption lines. The more contaminated and blended a absorption line is, will result in more uncertain results at the end of the analysis. This will be described in detail in Section 3.2.2. In Figure 1.8 it is clear that the NIR spectrum is far less contaminated by absorption lines.

The main goal of this thesis is to work towards a consistent derivation of stellar atmospheric parameters for M stars in NIR. Before tackling the M stars, it is important to have a method that work well for solar-like stars (FGK), which are better known during countless studies.

⁹ Note that there are very little difference between a K7V and M0V. For the latter case, the situation raised in Figure 1.8 will be more clear.

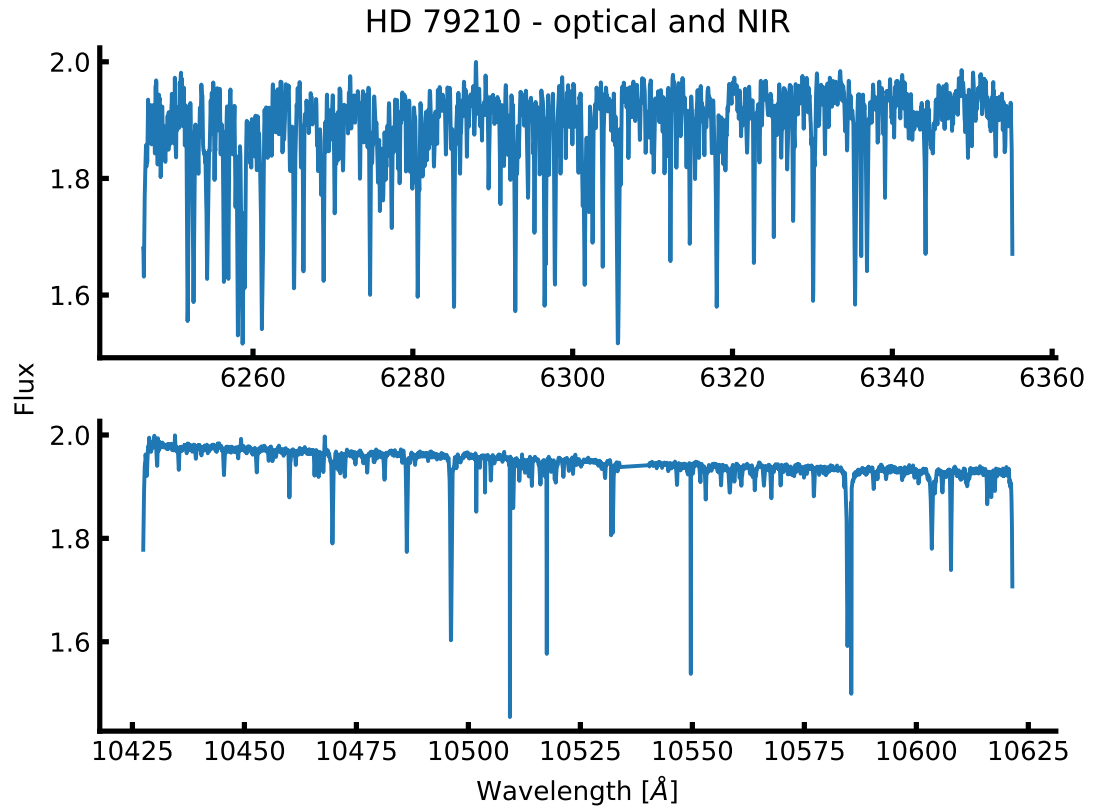


Figure 1.8: Comparison between an optical and NIR part of the spectrum of HD 79210 obtained by the CARMENES spectrograph. This clearly illustrate why NIR spectra are preferred over optical spectra for cool stars, where absorption lines are less blended. HD 79210 is a K7 dwarf star.

1.2.1 Star-planet correlations

While the stellar parameters are used to determine the planetary parameters, they can also be used to reveal correlations between planets and their host stars. This might give insight in the formation and evolution of the planets. Indeed, several important correlations have been found already.

Giant planet and metallicity correlation Since the first discoveries of exoplanets, it became evident that giant planets were systematically orbiting more metal-rich stars compared to stars with no planets. This correlation have been confirmed by several studies (Gonzalez, 1997; Santos et al., 2004; Fischer and Valenti, 2005; Sousa et al., 2008; Mortier et al., 2013b) and can be seen in Figure 1.9 using the data from Sousa et al. (2008). This correlation in turn establish that core accretion is likely the main formation mechanism among giant exoplanets (Pollack et al., 1996; Ida and Lin, 2004; Mordasini et al., 2012) and not disc instability (Boss, 2002).

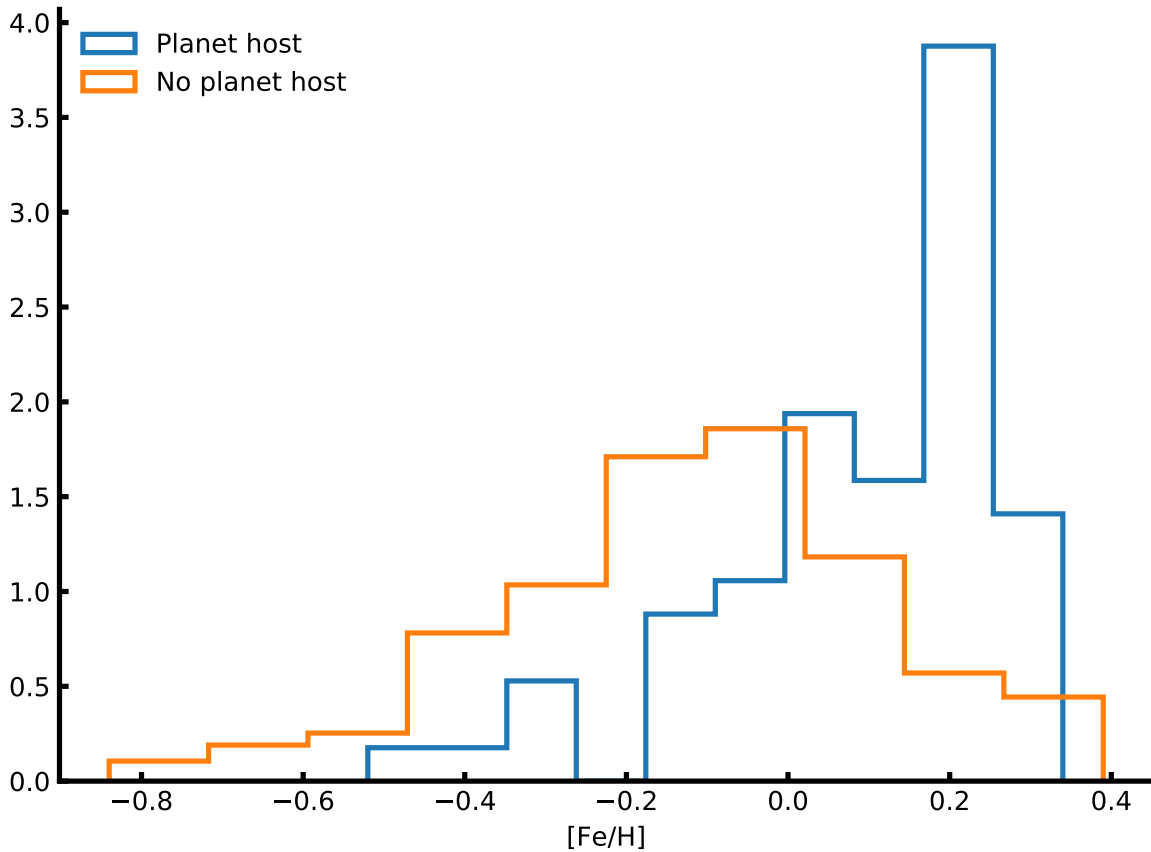


Figure 1.9: Metallicity correlation for giant planets, comparing planet hosts and non host stars from the sample of Sousa et al. (2008). It is clear that planet host stars have higher metallicities than non hosting stars. The histograms are normalised.

It is important to note that recent studies find this correlation for Neptune-like and super-Earth planets as well (Adibekyan et al., 2012a; Wang and Fischer, 2015; Zhu et al., 2016) even if a debate exists (Sousa et al., 2011; Buchhave et al., 2012).

It has been shown that metal-poor stars harbouring gas planets are enhanced in alpha elements¹⁰ (see e.g. [Adibekyan et al., 2012a](#)). This means that other elements than iron also have a role to play in planet formation in iron-poor environments.

Lithium and the presence of planets It has been shown by [Israelian et al. \(2004\)](#); [Delgado Mena et al. \(2014\)](#); [Figueira et al. \(2014a\)](#); [Gonzalez \(2015\)](#); [Takeda and Kawanomoto \(2005\)](#) that stars hosting planets are significantly more Li depleted compared to stars without planets. This correlation seems to be physically related with the occurrence of planets and not e.g. age, mass, or metallicity of the stars ([Sousa et al., 2010](#)). Other studies does not find any correlation between Li depletion and stars with planets ([Baumann et al., 2010](#); [Ramírez et al., 2012](#)).

1.3 Applications from knowing the stars

While “know the star, to know the exoplanet” is the main motivation behind this thesis, it is obviously not the only application behind detailed stellar characterisation. Working towards a better understanding of especially M stars, which consist of to 70% of all the stars in the Milky Way ([Bochanski et al., 2010](#)), will also open a new window into the study of different galactic components and galactic chemical evolution. Such a study was done by e.g. [Adibekyan et al. \(2012b\)](#); [Delgado Mena et al. \(2017\)](#) where spectra of 1111 FGK dwarf stars from the HARPS GTO sample was used to derive chemical abundances of 12 refractory elements. It is possible to separate different galactic populations (thin disk, thick disk, and the halo) by studying the chemical abundances of stars as was shown in [Adibekyan et al. \(2012b\)](#).

In order to do a detailed chemical analysis¹¹, it is crucial to have reliable and homogeneously derived stellar atmospheric parameters. If the parameters are homogeneously derived, i.e. with the same method, then errors when comparing populations are minimised and in case of known offsets it is easy to correct for them (this is the case for the method used throughout this thesis, where the surface gravity will be corrected based on another method).

1.4 This thesis

This thesis will be focused on deriving stellar atmospheric parameters for FGK stars, making the bridge towards M stars. This task will be accomplished utilising high resolution and high S/N NIR spectra; a methodology using a wavelength domain still in its infant stage. The theory of stellar atmospheres in a nutshell is described in Chapter 2, setting up all the tools to derived them as described in Chapter 3. In Chapter 3 the description of other useful and commonly used methods for deriving parameters are also presented. Thereafter the knowledge will all be used in Chapter 4. First by obtaining a NIR line list containing Fe I and Fe II lines, then by the derivation of parameters for HD 20010 (F sub-giant). Before deriving parameters for two K giants, the NIR line list will be revisited.

After focusing on the NIR spectra, the optical counterpart of the method described below will be used to derive parameters for 50 planet-host stars for an online catalogue of homogeneously derived parameters (SWEET-Cat) in Chapter 5.

¹⁰ These are elements formed by fusion of a helium core; C, N, O, Ne, Mg, Si, S, Ar, Ca, and Ti.

¹¹ See also references within [Adibekyan et al. \(2012b\)](#) for other similar studies.

Last in Chapter 6 the future of the work established here will be discussed along with the results already obtained. This will round of the thesis.

After the last chapter there will be a few appendices with large tables that would otherwise distract the reader from the main points. One appendix, Chapter C, will be on derivation of stellar atmospheric parameters using machine learning, which was a side project during the thesis. This appendices are followed by the bibliography for this thesis.

Theory of stellar spectroscopy in a nutshell

“Begin at the beginning,” the King said, very gravely, “and go on till you come to the end: then stop.”

Lewis Carroll, *Alice in Wonderland*

To encompass all theory regarding stellar atmospheres is far beyond the scope of this thesis. Rather the theory needed is presented below with highlights on the most important aspects.

2.1 Stellar atmosphere

Much of this Section is inspired by [Gray \(2005\)](#). While all the figures here were made by the author of this thesis, most of them can be found in [Gray \(2005\)](#) as well.

Stellar atmospheres are rather complex. This is where the energy produced in the interior of the stars is released. However, the atmosphere of a star is not completely transparent to all light, and some of the light is absorbed or scattered in the atmosphere. In the case of absorption the light will later be emitted in a random direction. This is seen as an absorption line in the stellar spectrum. The different elements in the atmosphere is the reason for absorbing light at specific wavelength. The strength of the absorption depends on the physical conditions in the atmosphere, the effective temperature (T_{eff}), the pressure/gravity ($\log g$), the chemical abundances, and the atomic characteristics of the transition making the absorption line.

The strength of a line depends on the fraction of atoms excited to the n th energy level, N_n , on which the electron that produces the absorption is. This fraction is proportional to the statistical weight g_n and the Boltzmann factor and is described as:

$$\frac{N_n}{N} = \frac{g_n}{u(T)} 10^{-\theta \chi_n} \quad \text{Boltzmann}$$

This equation is also called the Boltzmann equation. Here N is the total number of atoms per unit volume, $u(T) = \sum g_i e^{-\chi_i/kT}$ is the partition function, k is Boltzmann’s constant, T is the temperature, and χ_n is the excitation potential for the lower energy level.

While atoms can get excited following Boltzmann’s equation above, they can also get ionized. The

ionization ratio for a collision dominated gas (which is a good approximation for FGKM stars, when assuming Local Thermodynamic Equilibrium, LTE¹) is described by the Saha equation. This equation relate the ratio of atoms in state r to atoms in the excited state above for the same element, $r + 1$, in the following way:

$$\frac{N_{r+1}}{N_r} = \frac{1}{P_e} \frac{(2\pi m_e)^{3/2} (kT)^{5/2}}{h^3} \frac{2u_{r+1}(T)}{u_r(T)} e^{-I/kT} = \frac{\Phi(T)}{P_e} \quad \text{Saha}$$

here m_e is the electron mass, h is Planck's constant, I is the ionization potential of the neutral atom, and $\Phi(T)$ is all not related to the electron pressure, P_e .

The atomic lines are characterised by a few quantum mechanical descriptors.

- **The wavelength**, λ , of an absorption (or emission) describes the energy difference between the two energy levels where the transition occurs.
- **The ionization state**, e.g. Fe I describes iron in its atomic form, while Fe II describes iron in its first ionized form.
- **The excitation potential**, χ , is the excitation energy level of the lower state in the transition. A atomic line with a high χ is formed in the deeper layers of the atmosphere, since the higher temperatures there can excite the element. This is compared to the atomic lines with lower χ which are formed higher in the atmosphere at lower temperatures.
- **The oscillator strength**, $\log gf$, is related to the atomic transition probability.
- **The damping coefficients**, Γ , is a natural damping (also known as radiation damping) caused by the uncertainty of lifetime in an energy level according to Heisenberg's uncertainty principle. This is related to a uncertainty in the energy level and thus a natural broadening is introduced.

These are essential to know from either theoretical calculations or experiments. The oscillator strength is a quantity that is difficult to measure, and these values are often changed when absorption lines are matched with real observations of e.g. the Sun. This is a way of calibrating a line list and will be described in detail in Section 4.1.

It is important to mention that one of the main differences between absorption lines at different wavelengths is the excitation potential. The energy levels of an atom gets denser packed as the energy level increase as shown in Figure 2.1 for hydrogen. For hydrogen the energy levels E_n follow the very simple formula from Bohr's atomic model, $E_n = \frac{-13.6 \text{ eV}}{n^2}$, where n is the principal quantum number, and 13.6 eV is the ionization energy for hydrogen, i.e. the minimum amount of energy required to ionize hydrogen. The energy levels for heavier atoms show a similar structure. The outer electron for a multi-electron atom is partially shielded from the nucleus by the inner electrons, and thus does not experience the full charge Z but rather an effective charge Z_{eff} , giving the expression

$$E_n = -hcR_\infty \frac{Z_{\text{eff}}^2}{n^2}, \quad (2.1)$$

where h is Planck's constant, c is the speed of light, and R_∞ is Rydberg's constant.

¹ LTE is obtained in stellar atmospheres, when the length scale at which temperatures are changing are larger than the mean free path. This is a good approximation for dwarf stars, where the mean free path is small, compared to the larger mean free path in evolved stars, where LTE is no longer a good assumption.

With increasing n the energy levels get closer, or in other words the photon required to excite an electron from one energy level to a neighbouring state will get redder. These redder photons used for exciting an atom are the absorption lines seen in the NIR. However, the excitation to the lower state is related to the temperature and pressure according to the Boltzmann and Saha equations. Since tight energy levels require a highly excited lower state, the temperature required here are similar high, which means that the NIR lines are typically formed in the deeper layers of the atmosphere compared to absorption lines seen in the optical part of the spectrum.

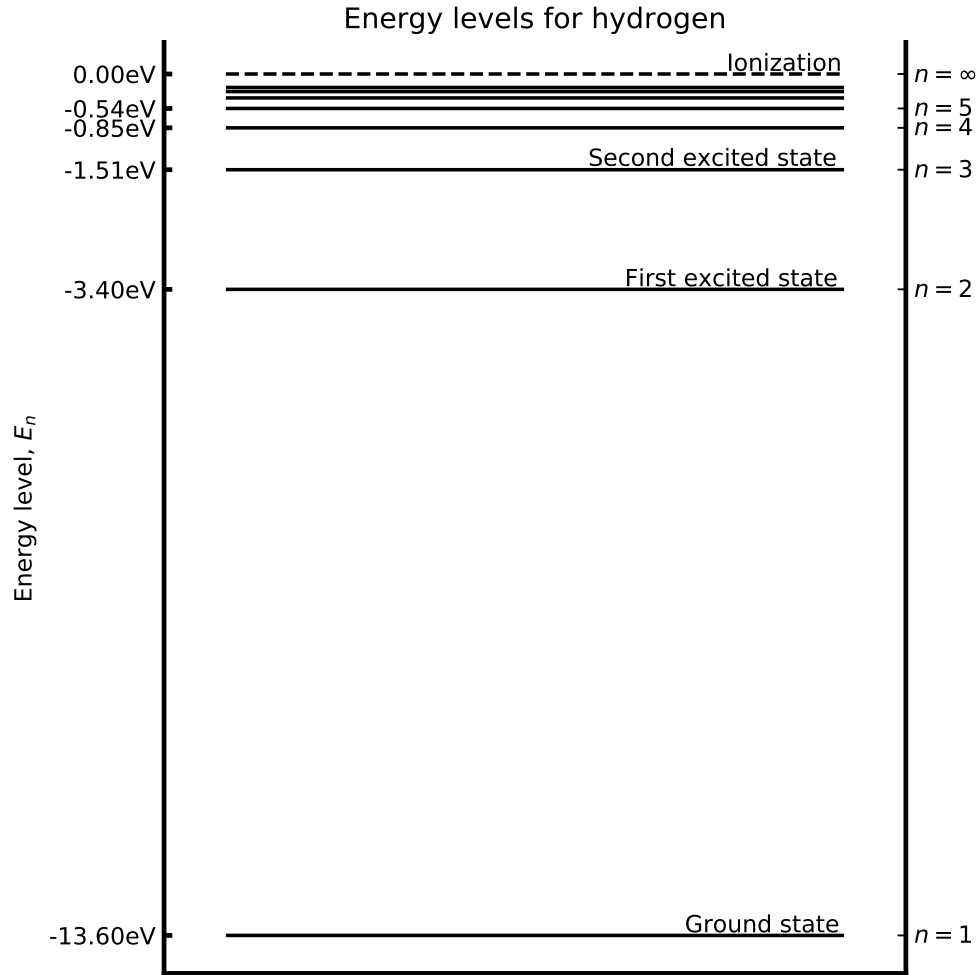


Figure 2.1: Energy levels for hydrogen, $E_n = \frac{-13.6 \text{ eV}}{n^2}$.

The above discussed energy transitions are purely electronic, however there exists so called fine structure transitions as well. This is due to the spin of the electron (or magnetic moment) interacting with the orbital angular momentum of the electron. This leads to a splitting of the absorption line. In atoms there also exists an even finer structure, commonly known as the hyperfine structure. This structure arise due to the interaction between the magnetic field created by the electrons and the nuclear spin. These splittings are important to consider for some transitions and some atoms. For Fe the hyperfine structure is not important since the net nuclear spin of protons is 0 because there is an even number of protons, hence hyperfine structure is only important for atoms with an odd number of protons. There

are other splitting and shift for spectral absorption lines like the Zeeman splitting caused by an external magnetic field, and the Stark effect splitting a line due to an external electric field. These two last effect are minor and will not be discussed more, however it is worth noting that the Zeeman splitting can be used to measure the strength of a magnetic field in a star if this is strong enough.

2.1.1 Atmosphere models

In order to derive abundances or calculate a synthetic spectrum, two main things are needed: 1) An atmosphere model, and 2) a radiative transfer code that solves the equations above. There are different atmosphere models available. Throughout this thesis the ATLAS9 model atmosphere are used (Kurucz, 1993). Other atmosphere models includes MARCS models (Gustafsson et al., 2008) and the PHOENIX models (Husser et al., 2013). An atmosphere model is a description of the structure of the atmosphere. This description has a number of quantities. The Kurucz atmosphere model grids that are available and used here have 72 layers. Each layer includes physical quantities such as temperature, gas and electron pressure, and the optical depth. The models can be calculated on the fly, but it is common practise because of computational reasons to pre-calculate a grid of atmosphere models at certain T_{eff} , $\log g$, and $[\text{Fe}/\text{H}]$. A specific atmosphere model is then obtained from this grid by interpolating from nearest neighbours. The interpolation code used throughout this work includes the four nearest neighbours in the T_{eff} -space, and the two nearest neighbours in both the $\log g$ - and $[\text{Fe}/\text{H}]$ -space, in total $4 \times 2 \times 2 = 16$ atmosphere models to generate a single interpolated atmosphere model.

2.1.2 Radiative transfer code - MOOG

There exists many different codes that solves the radiative transfer equations. In this thesis the MOOG² code is used by Sneden (1973) which assumes LTE. This code has different drivers, only some are used here.

- Derive a theoretical equivalent width (see Section 2.1.3 for details) for a given star, i.e. atmosphere model with a given set of atmospheric parameters.
- Derive line abundance from a measured equivalent width for a given model atmosphere.
- Calculate a synthetic spectrum for a given model atmosphere and atomic line list.
- Calculate the curve-of-growth for an atomic line.

There exists other drivers as well, but these are the ones used here. Some only for visualising the figures below.

2.1.3 The equivalent width

Measuring the equivalent width (EW) of spectral lines are important for some analysis of stellar spectra. The EW is a measure of the strength of the line, and dependent on the atmospheric conditions in where the spectral line is formed, such as T_{eff} , $\log g$, $[\text{Fe}/\text{H}]$, and ξ_{micro} .

² <http://www.as.utexas.edu/~chris/moog.html>

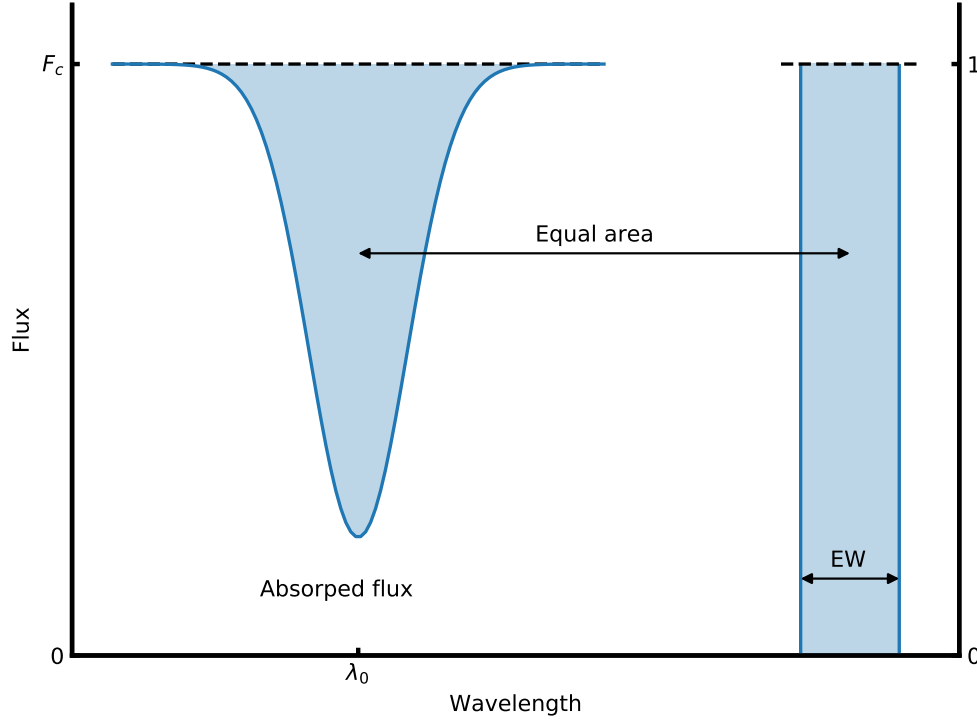


Figure 2.2: An absorption line centred at λ_0 normalised at the flux level F_c . The area of the absorption line to the left is equal to the blue shaded area in the rectangle to the right with width EW.

The EW is mathematically described as integrating over the entire line, and assign this area to a rectangle from 0 to the normalised continuum flux (F_c) with the width, EW. This is illustrated in Figure 2.2 and the equation below:

$$EW = \int_0^\infty \frac{F_c - F(\lambda)}{F_c} d\lambda, \quad (2.2)$$

where λ is the wavelength. In the integral above it is assumed that there is only one single line, hence the integral is over all wavelength. In practice the integral is calculated in small windows around a spectral line. See Section 3.2.2.2 for more details on how this is performed in practice. The unit of the EW is the same as the wavelength used. Throughout this thesis we will use Ångström ($1 \text{ Å} = 0.1 \text{ nm}$) for the wavelength, and mÅ for the EW.

2.1.3.1 Temperature dependence

As mentioned above, the theory presented here is the bare minimum. For the full derivations of the equations presented below see Chapter 13 in Gray (2005).

As mentioned above the EW depends on the atmospheric parameters. At low T_{eff} neutral elements, say Fe I, are the strongest lines as the number of ionized atoms are too small to contribute significantly to the EW. This is the result the Saha equation. As T_{eff} increases Fe I is converted into ionized Fe II. Slowly, as the number of Fe I decreases so does the EW, and likewise as the number of Fe II increases so does the EW. This goes on until second ionized atoms, Fe III, are formed and the same situation arise again.

This is illustrated in Figure 2.3 where the EW of two iron lines, one neutral and one ionized, are plotted against T_{eff} . These two lines have similar EW in the Sun: 46.2 mÅ and 53.9 mÅ for the Fe I and Fe II line respectively.

This can be explained with four simple cases:

Case 1 Weak line of a neutral species (e.g Fe I) with the element mostly neutral

Case 2 Weak line of a neutral species with the element mostly ionized

Case 3 Weak line of an ion species (e.g Fe II) with the element mostly neutral

Case 4 Weak line of an ion species with the element mostly ionized

The behaviour of the line strength R is shown in the equations below for the four different cases

$$\frac{1}{R} \frac{dR}{dT} = \frac{2.5}{T} + \frac{\chi + 0.75}{kT^2} - \Omega \quad \text{Case 1}$$

$$\frac{1}{R} \frac{dR}{dT} = \frac{\chi + 0.75 - I}{kT^2} \quad \text{Case 2}$$

$$\frac{1}{R} \frac{dR}{dT} = \frac{5}{T} + \frac{\chi + 0.75 + I}{kT^2} - 2\Omega \quad \text{Case 3}$$

$$\frac{1}{R} \frac{dR}{dT} = \frac{2.5}{T} + \frac{\chi + 0.75}{kT^2} - \Omega, \quad \text{Case 4}$$

where χ is the excitation potential, I is the ionization energy, and Ω can be considered a constant as it mildly depends on pressure. The four cases are also shown in Figure 2.3.

2.1.3.2 Pressure dependence

Pressure dependence in the stellar atmosphere can be related to the gravity dependence. There are many ways to measure the pressure, and thus the gravity which is what is ultimately the goal with the measurement of $\log g$. Below are listed some of the most common methods to measure $\log g$ from spectroscopy.

- Continuum: The Balmer jump is the only continuum feature sensitive enough to estimate the $\log g$.
- Hydrogen lines: Hydrogen profiles are pressure and temperature sensitive and can therefore be used to estimate $\log g$. However, the gravity dependence rapidly diminishes for temperatures above 10 000 K.
- Other strong lines: There exists other strong lines with pressure-broadened wings such as the Ca II H and K lines. These are better for cooler stars than the hydrogen lines described above.
- Weak lines: By comparing two stages of ionization for the same element it is possible to obtain $\log g$ using weaker or modestly strong lines.

In this thesis weak lines are used to measure $\log g$. More specifically a comparison between Fe I and Fe II lines are used. For FGK stars, as the atmosphere contracts (i.e. $\log g$ increases) the pressure likewise increases, which in turn means that both the gas pressure, P_g , and electron pressure, P_e , increases. However, the electron pressure is much smaller than the gas pressure because hydrogen, as the main

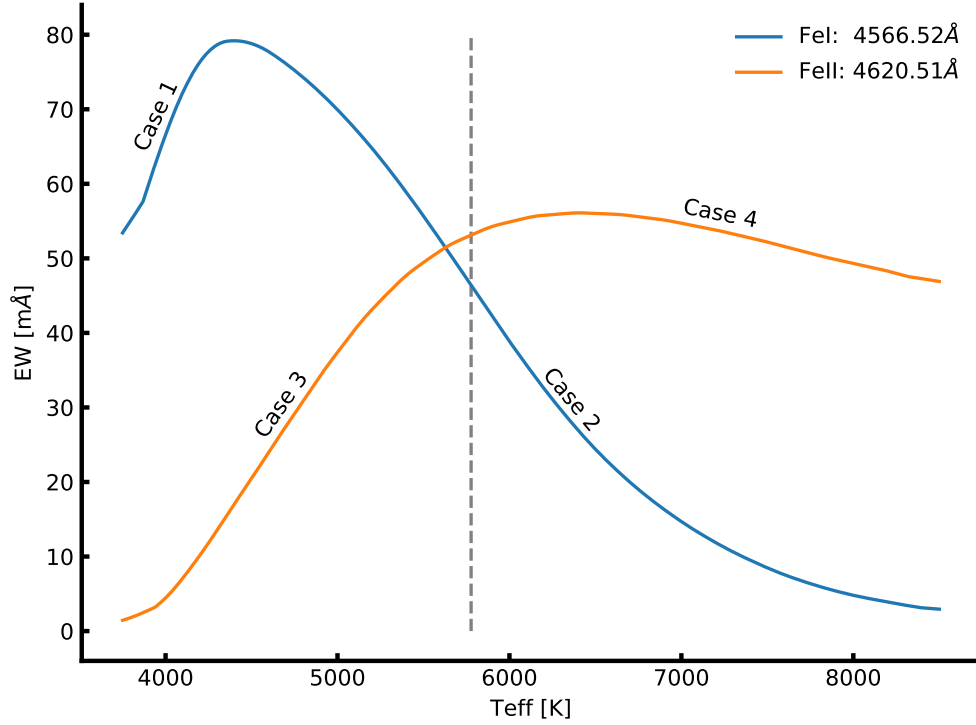


Figure 2.3: The EW for a FeI and FeII line with increasing T_{eff} . The two lines have similar EW in the Sun and are found in the optical part of the spectrum. The vertical line show the solar T_{eff} .

electron contributor, is not fully ionized. The gas pressure follow a simply empirical approximation with gravity:

$$P_g \approx \text{constant } g^{2/3}, \quad (2.3)$$

where g is the gravity. The electron pressure is in turn given by

$$P_e \approx \text{constant } g^{1/3}. \quad (2.4)$$

There are three cases for which a line show dependence on gravity, when considering only weak lines:

1. A weak line formed by any ion or atom, where most of the element is in the next higher ionized state.
2. A weak line formed by any ion or atom, where most of the element is in the same ionized state.
3. A weak line formed by any ion, where most of the element is in the next lower ionized state.

Using the [Saha](#) Equation for case 1, it is important to note that the number of the atoms in the highest state is roughly equal to the total number of atoms of that element, $N_{r+1} \approx N$. Hence

$$N_r \approx \text{constant } P_e \quad (2.5)$$

which means that the line absorption coefficient is

$$l_\nu \approx \text{constant } N_r \approx \text{constant } P_e. \quad (2.6)$$

The strength of a weak line, R , is proportional to the ratio of the line to the continuous absorption coefficient, κ_ν

$$R = \frac{F_c - F_\lambda}{F_c} = \text{constant } \frac{l_\nu}{\kappa_\nu}. \quad (2.7)$$

When negative hydrogen dominates κ_ν which is the case here it is proportional to the electron pressure, $\kappa_\nu \propto P_e$ which means the line strength is not proportional to electron pressure:

$$R = \frac{l_\nu}{\kappa_\nu} \approx \text{constant}. \quad (2.8)$$

For case 2, the approach is the same, here $N_r \approx N_{r+1} \approx N = \text{constant}$. This leads to $l_\nu \approx \text{constant}$, eventually giving

$$R = \frac{l_\nu}{\kappa_\nu} \approx \frac{\text{constant}}{P_e} \approx \text{constant } g^{-1/3}. \quad (2.9)$$

Only the first two cases are relevant for solar-type stars used in this thesis, and the relation for the third case will be omitted.

In Figure 2.4 is shown how the Fe II line used previously change with $\log g$. The curve of growth is shown in the upper panel, while a synthetic spectrum for each $\log g$ is presented in the lower left panel. It is clear that the ionized line is sensitive to $\log g$ as shown in the lower right panel, where the correlation between the abundance and $\log g$ is 0.40. This is expected as can be seen in Gray (2005, Table 16.1). There is used $\delta \log A / \delta \log g$ as an indicator, and for neutral elements the correlation is much weaker. It is important to note that the correlation does change with T_{eff} and the element used.

2.1.3.3 Abundance dependence

The abundance of a given element obviously has an effect on the EW. The more abundant an element is, the more photons can be absorbed thus increasing the EW. However, the relationship is not strictly linear. For weak lines (see Figure 2.5) EW is approximately linear with the abundance, however it reach a plateau where the core of the line saturates. In this regime the EW only increases slowly, until the absorption “spills” into the wings and the increase is again linear. However, for these strong lines the profile is no longer Gaussian. The curve of growth for the same Fe I line used in Figure 2.3 is shown in Figure 2.5. Instead of EW it is common to use the reduced EW, $\log(EW/\lambda)^3$, which we will use more later.

2.1.3.4 Microturbulence

Small-scale motion, that is motion of material at length scales small compared to the unit optical depth, are called microturbulence, ξ_{micro} . This is not to be confused with macroturbulence, which is motion of material at scales larger than the unit optical depth. The latter is associated with granulation and

³ The reduced EW is useful since it normalises Doppler-dependent phenomena, such as microturbulence and thermal broadening.

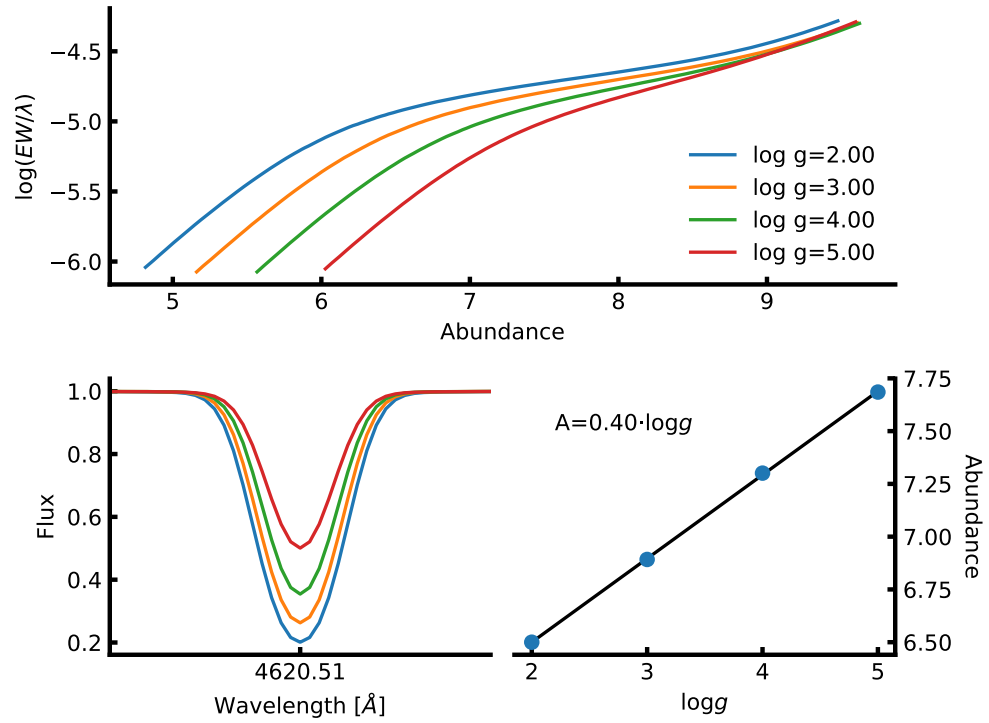


Figure 2.4: *Upper panel:* Curve of growth for same Fe II used in Figure 2.3 for four different $\log g$ values. Here it is the weak lines mostly affected by the change in $\log g$. *Lower left panel:* Synthetic spectra of the same line. The colour scale is the same. *Lower right:* The abundance for the line at different $\log g$. A strong correlation (0.40) is seen.

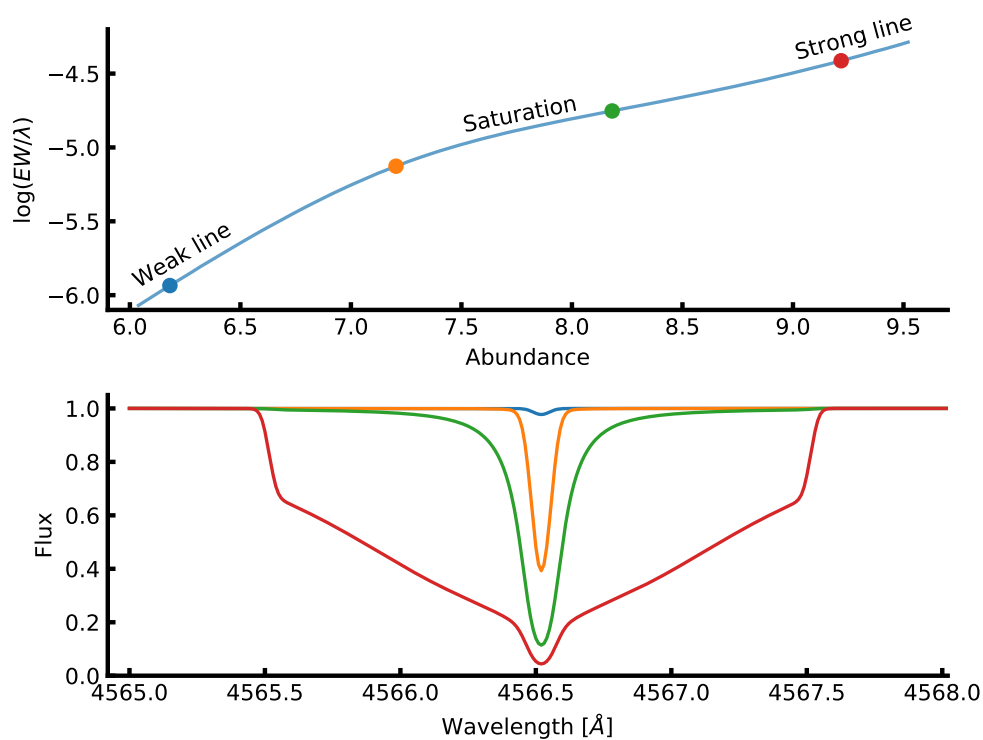


Figure 2.5: *Upper panel:* Curve of growth of the same FeI line as used in Figure 2.3. Four points are marked which is shown in the *lower panel* as a synthetic spectral line. The RW (proxy for EW) is clearly increasing with abundance.

will not be discussed further in this thesis. ξ_{micro} comes into play when looking at the curve of growth for saturated lines (i.e. between green and red points in Figure 2.5). If no ξ_{micro} is assumed, then the measured abundance is higher than predicted by models based on thermal and damping broadening alone. In Figure 2.6 is shown three curves of growth with $\xi_{\text{micro}} = 0.5 \text{ km/s}$, 2.5 km/s , 5.0 km/s . As ξ_{micro} increases, so does the EW and hence the abundance.

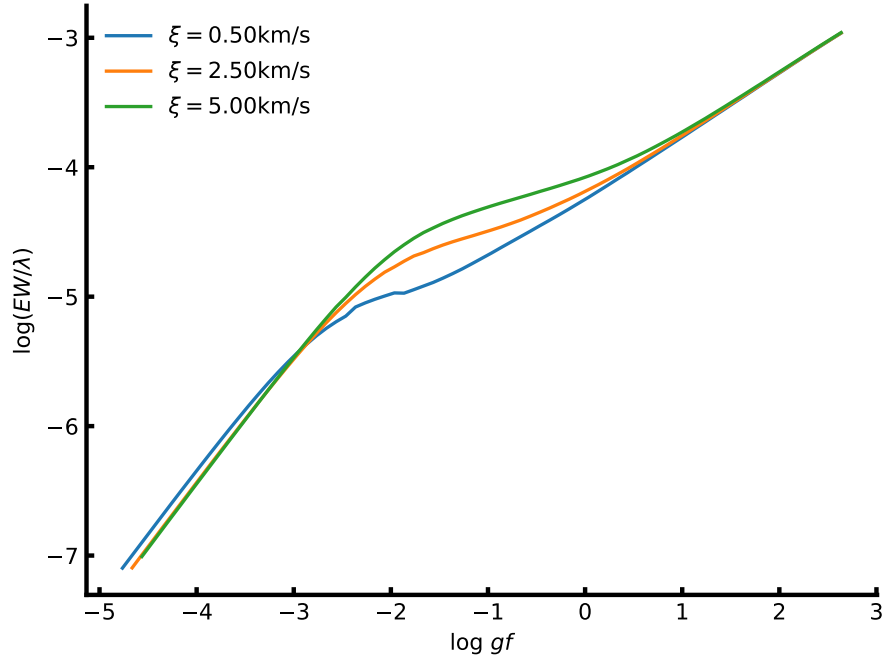


Figure 2.6: Curve of growth for three different values of ξ_{micro} . The EW is increasing with increasing ξ_{micro} .

The broadening of an absorption line measured by the shift in wavelength, $\Delta\lambda$, when ξ_{micro} is included is defined as:

$$\Delta\lambda = \frac{\lambda_0}{c} \sqrt{\frac{2kT}{m} + \xi_{\text{micro}}^2}, \quad (2.10)$$

where c is the speed of light, λ_0 is the rest wavelength of the given line, k is Boltzmann's constant, T is the temperature, and m is the mass of the atom. Setting $\xi_{\text{micro}} = 0 \text{ km/s}$, we end up with thermal broadening.

Deriving stellar parameters

The best way to learn is by doing. The only way to build a strong work ethic is getting your hands dirty.

Alex Spanos

There are different methods for obtaining stellar atmospheric parameters. Here follows a short description of some of the most common methods, however the spectroscopic method will be explained in much greater detail later in this chapter.

3.1 Photometry

Photometry can be used in different ways to estimate the effective temperature. In this section two methods will be mentioned; a colour calibration, and asteroseismology. There are other methods, e.g. SED fitting but this will not be discussed further.

3.1.1 InfraRed Flux Method - IRFM

The InfraRed Flux Method (IRFM) was first described by [Blackwell and Shallis \(1977\)](#). From IRFM it is possible to measure the stellar radius and T_{eff} with a measurement of the angular diameter, θ , derived from infrared photometry. T_{eff} is derived from the angular diameter from the simple relation

$$\sigma T_{\text{eff}}^4 = \frac{4\mathcal{F}_E}{\theta^2}, \quad (3.1)$$

where \mathcal{F}_E is the monochromatic flux measured at Earth, and σ is Boltzmann's constant. The angular diameter is calculated from the following equation:

$$\theta = 2\sqrt{\mathcal{F}_E/\mathcal{F}_S}, \quad (3.2)$$

where \mathcal{F}_S is the calculated monochromatic flux from the star. This flux is based on a model atmosphere with an effective temperature based on the spectral energy distribution (SED). The calculated flux show a strong dependence on T_{eff} in the visible, however this dependence is much weaker in the infrared. Hence

a poor first estimation of T_{eff} will lead to a reliable angular diameter. From this new angular diameter T_{eff} can be re-derived, a new model atmosphere can be used with a new set of \mathcal{F}_S can be calculated. Iteratively the angular diameter and T_{eff} can be calculated. If the distance d is known of the star, the stellar radius is $R_* = \frac{\theta d}{2}$. The solar flux, both measured and calculated, from [Blackwell and Shallis \(1977\)](#) are shown in Figure 3.1. Using the data provided the solar radius and T_{eff} were derived using the equations above: $R = 1.011R_{\odot}$ and $T_{\text{eff}} = 5963\text{ K}$. This was simply done for each wavelength, and the results presented here are just a simple average value.

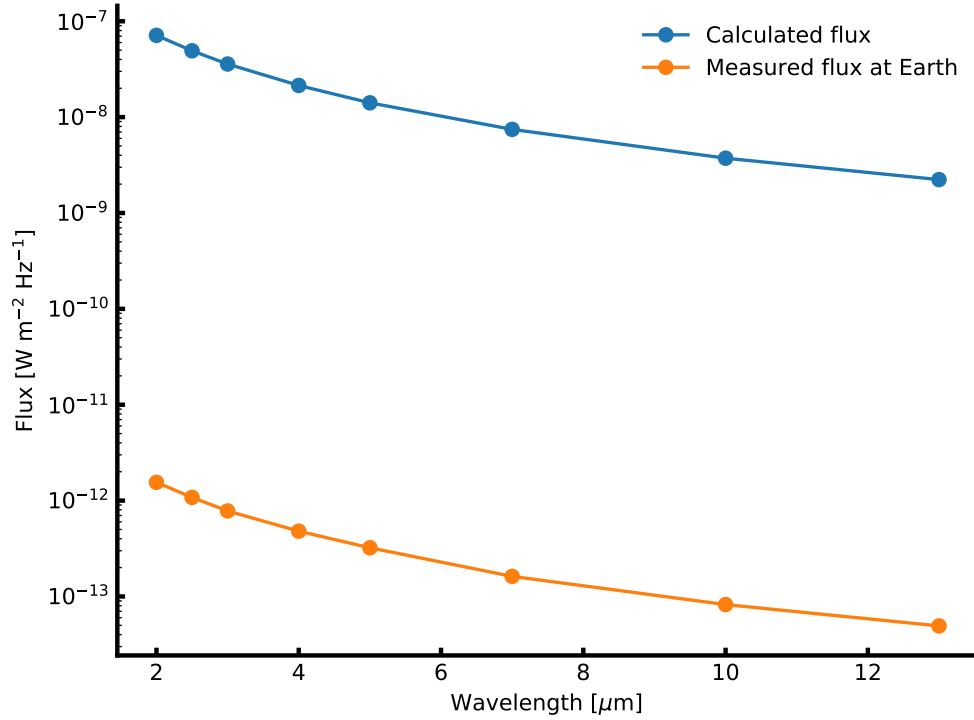


Figure 3.1: Measured and calculated flux from the Sun at infrared wavelengths. Data from Table 2 in [Blackwell and Shallis \(1977\)](#). Mean solar radius from this data is $1.011R_{\odot}$, and mean solar $T_{\text{eff}} = 5963\text{ K}$ using Equation 3.3.

The main drawbacks of the IRFM is the model dependence, a drawback many methods share, and the need of high precision infrared photometry. For the model atmosphere a metallicity and surface gravity is assumed which has an effect on \mathcal{F}_S , and hence on the final derived T_{eff} and R . A more in-depth description of the IRFM can be seen in e.g. [Casagrande et al. \(2006, section 4\)](#).

3.1.2 T_{eff} -colour-[Fe/H] calibration

Photometry can be used for deriving T_{eff} using existing colour calibrations like that of for example [Ramírez and Meléndez \(2005\)](#) where adopted T_{eff} and [Fe/H] in combination with colours X such as $B - V$, $V - S$, etc. are used to fit a polynomial such that the T_{eff} can easily be estimated with a simple relation:

$$\theta_{\text{eff}} = a_0 + a_1X + a_2X^2 + a_3X[\text{Fe}/\text{H}] + a_4[\text{Fe}/\text{H}] + a_5[\text{Fe}/\text{H}]^2, \quad (3.3)$$

where $\theta_{\text{eff}} = 5040/T_{\text{eff}}$. A polynomial fit was performed on the residuals in order to deal with spectroscopic features such as the Balmer lines, the Paschen jump, etc. This polynomial fit, $P(X, [\text{Fe}/\text{H}])$ is added to Equation 3.3 so the calibration finally reads:

$$T_{\text{eff}} = \frac{5040}{\theta_{\text{eff}}} + P(X, [\text{Fe}/\text{H}]), \quad (3.4)$$

After obtaining the coefficients (a_i) for different combinations of colours, it is trivial to obtain T_{eff} if the metallicity and a colour is known of the star.

3.1.3 Asteroseismology

Asteroseismology is the study of stellar pulsations. For main sequence stars (which will be the only focus here), these pulsations propagate as sound waves throughout a star, their origin and amplitude is determined by the characteristics of the star. Hence the study of the pulsations, which are seen on the surface, will thus be a study of the stellar properties. In order to study these a time series is needed. This can both be radial velocities as it was used in the recent results from the SONG telescope (Grundahl et al., 2017), or photometry like the numerous results from e.g. the space telescopes *CoRoT* and *Kepler* (see e.g. Christensen-Dalsgaard et al., 2010; Chaplin et al., 2011; Huber et al., 2014). The analysis is identical for either time series, however the amplitudes in the power spectrum will be different.

After determining the frequencies of a range of pulsations from a power spectrum of the time series, a pattern emerge at every $\Delta\nu$ (the so-called large frequency separation). A finer pattern also occur described by $\delta\nu$. Last the frequency at maximum power is also measured from the power spectrum, ν_{max} . The frequency at maximum power is used to obtain $\log g$ via

$$\nu_{\text{max}} \propto \frac{g}{\sqrt{T_{\text{eff}}}} \quad (3.5)$$

$$= \frac{M/M_{\odot}}{(R/R_{\odot})^2 \sqrt{T_{\text{eff}}/5777}} 3.05 \text{ mHz}, \quad (3.6)$$

where $\nu_{\text{max},\odot} = 3.05 \text{ mHz}$ is the frequency of maximum amplitude for the Sun. A similar equation exists for the determination of the stellar density:

$$\Delta\nu = (M/M_{\odot})^{-1/2} (R/R_{\odot})^{-3/2} 134.9 \mu\text{Hz}. \quad (3.7)$$

These simple scaling relation are described in detail in Kjeldsen and Bedding (1995) for main sequence stars. These two equations can be used together to determine the mass and radius of the star, often to a high precision. These scaling relations are applicable for stars which shows solar-like oscillations, mostly found in main sequence FGK stars, but can also be found in red giant stars. The mass and radius for a range of ν_{max} and $\Delta\nu$ can be seen in Figure 3.2, where $T_{\text{eff}} = 5777 \text{ K}$. The star located at $\{\Delta\nu = 134.9 \mu\text{Hz}; \nu_{\text{max}} = 3.05 \text{ mHz}\}$ is the Sun.

The small frequency separation, $\delta\nu$, is sensitive to the sound-speed gradient in the core which in turn is sensitive to the composition. Thus the small frequency separation is a very important diagnostic for stellar evolution. An interesting case is that of Bedding et al. (2011), where it was shown it is possible to distinguish between hydrogen- and helium-burning cores in red giant stars.

A drawback of asteroseismology is the dependence of T_{eff} in Equation 3.6 which has to be provided

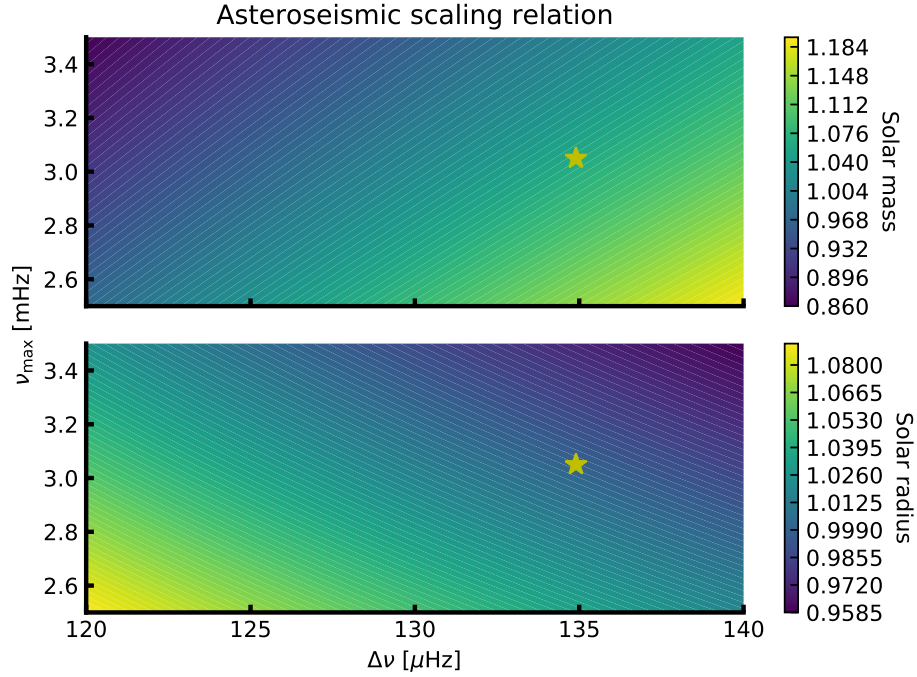


Figure 3.2: Mass and radius from asteroseismic scaling relation. The colour is the mass and radius for the upper and lower panel, respectively. The location of the Sun is added for reference.

from another method. Ideally this will come from spectroscopy for which the determination of T_{eff} is often reliable. This drawback is minor compared to the weak model dependence which is one of the strongest advantages of asteroseismology.

For both of the mentioned photometric methods to determine some atmospheric parameters a disadvantage is the dependence on the knowledge of other atmospheric parameters which usually comes from spectroscopy (e.g. metallicity). However, as will be discussed in Section 3.2 $\log g$ is often difficult to determine reliably and synergies are welcomed between different methods.

3.2 Spectroscopy

A spectrum can be analysed with a range of different methods. The method finally chosen depend on quality of the spectrum, i.e. high/low resolution and high/low S/N, the spectral type of the star, the region that was observed, e.g. UV, optical, NIR, etc., some stellar properties, e.g. fast-rotator, activity, etc. In practise, no methods work for all cases, but sometime several methods can be used for on case.

Since this thesis is focused on FGKM stars, and mainly dwarfs, three methods will be described; synthesis, spectral indices, and the EW method. The latter method will be described in a separate section since this is the main method used for the analysis in this thesis.

3.2.1 Synthesis

The synthesis fitting method is a standard method for obtaining stellar atmospheric parameters from a wide range of spectra, that is with different spectral resolution, spectral parameters such as T_{eff} , $\log g$, $v \sin i$ the projected rotational velocity, etc., and S/N (see e.g. [Tsantaki et al., 2017](#)). The synthetic fitting method is in simple terms a comparison between the observed spectrum and a synthetic spectrum, which is either calculated on the fly like Spectroscopy Made Easy (SME) ([Valenti and Piskunov, 1996](#)), or using a pre-calculated grid like Starfish ([Czekala et al., 2015](#)). By analysing the

$$\chi^2 = \sum_i^N \frac{(y_{\text{obs},i} - y_{\text{model},i})^2}{\sigma_i^2}, \quad (3.8)$$

the synthetic spectrum that best match the observed spectrum can be found. Here the y_{obs} is the observed spectrum, y_{model} is the synthetic spectrum, and σ is the error on the measurement.

The synthetic fitting can be done by utilising small windows around sensitive spectral features such as ionized lines or hydrogen lines for obtaining the surface gravity, iron lines for obtaining the effective temperature, a series of different atomic lines for obtaining the overall metallicity. This approach is used by SME and FASMA ([Valenti and Piskunov, 1996](#); [Tsantaki et al., 2017](#), respectively) and is a compromise between fitting the entire spectral range and calculating the synthetic spectra on the fly which is time consuming. On the other hand the entire spectrum can be fitted if a pre-calculated grid of synthetic spectra are available. By masking small windows, one can also exclude different features that are troublesome, this can be telluric lines, bad reduction of the spectra, or real spectral features where there currently is poor atomic/molecular data such as the oscillator strength and thus it is not possible to reliably fit this feature.

This method is affected by the different approaches one can use, that is which atmosphere models are used (ATLAS, MARCS, etc.), atomic data and whether this has been calibrated, the radiative transfer code in the case the synthetic spectra are calculated on the fly, and the minimization procedure chosen. With these things in mind it is important to stress the wide range spectra and spectral classes this method works with.

The advantage of the synthetic fitting method over the curve-of-growth analysis (see Section 3.2.2) is that it allows for the analysis of lower resolution and with a higher rotational velocity, $v \sin i$.

3.2.2 The EW method and FASMA

The EW method or curve-of-growth analysis is another standard method for obtaining stellar atmospheric parameters from spectra as the synthetic fitting method (Section 3.2.1). Since this is the method used throughout this thesis it will be explained in detail. This analysis follow a chain of tasks, each has been made automatic in the software “Fast Analysis of Spectra Made Automatically” (FASMA¹) which was developed during this thesis ([Andreasen et al., 2017b](#)). FASMA is made of three **drivers**:

1. EW measurement driver
2. Obtain stellar atmospheric parameters driver
3. Abundance driver

¹ Greek for spectrum

An additional driver is under development; a synthetic fitting driver (Tsantaki et al., 2017). FASMA has been made available to the community via a web application at <http://www.iastro.pt/fasma/>.

3.2.2.1 Ingredients

FASMA is written in the Python programming language and glue together other software and model atmospheres necessary for obtaining stellar atmospheric parameters from high quality spectra. These software and models are described in greater detail in the following sections. In short, the curve-of-growth analysis require measured EWs where the latest version² of ARES is used (Sousa et al., 2015). These EWs are used to derive line abundances using model atmosphere like the ATLAS9 (Kurucz, 1993), MARCS models (Gustafsson et al., 2008), or PHOENIX models³ (Husser et al., 2013) to mention the most popular for this analysis. Note that the PHOENIX models are relative new and not as widely used yet. In tandem with model atmospheres a radiative transfer code is also needed. FASMA uses MOOG (Snedden, 1973) for this. The model atmosphere usually comes in a pre-calculated grid in the $\{T_{\text{eff}}, \log g, [\text{Fe}/\text{H}]\}$ parameter space. These are interpolated in order to access the requested combination of parameters. Last, FASMA consist of a minimization routine which looks for the best matching parameters given a spectrum.

3.2.2.2 Wrapper for ARES

There are two ways to measure the EW of an absorption line, “manually” or automatically. There are advantages and disadvantages for both approaches: For the manual, an advantage is that we can inspect the lines and try to measure lines in different ways (which is useful if a absorption line is blended). We have more control over how blended lines are fitted, and which profiles are used. Disadvantages are that it is very time consuming, and it is prone to errors, as a measurement might change drastically by the eyes measuring it. Even for the same person, the measurement can change. By mentioning the advantages and disadvantages of the manual method, it should be clear that the advantages and disadvantages of the automatic method is the opposite of those. Especially the time to measure the lines are orders of magnitudes faster, which is crucial when dealing with more than a handful of spectra. However, most important is the fact that the EWs of the lines are measured consistently throughout the entire spectral range, allowing a homogeneous analysis of the lines.

When a line is measurement by hand (manually) it is in this thesis done using the `splot` command in IRAF. Here the deblending mode is used whenever necessary. It is often necessary to fit one spectral lines with several Gaussians, as neighbouring lines might contaminate the line of interest.

Throughout this thesis line EWs are automatically measured with ARES (Sousa et al., 2007, 2015). When using ARES it is important to use a correct value of the `rejt` parameter. This parameter is used for placing the continuum level, and is thus directly related to the final measurement EW. It is difficult to get this parameter right, however the newest version of ARES has the option to analyse a few absorption free regions and measure the S/N. The `rejt` is then calculated as:

$$\text{rejt} = 1 - \frac{1}{\text{S/N}}.$$

ARES is used via the first driver of FASMA. All the options available for ARES can be accessed by FASMA. The options are

² The latest version can be found here: <https://github.com/sousasag/ARES>

³ The PHOENIX models are currently not a part of FASMA, however it is planned to implement these models with MOOG.

- Setting the spectral window, λ_{\min} and λ_{\max}
- RV correction to be applied or a mask to measure the RV and automatic make this correction
- Minimum and maximum EW to be considered (5 mÅ and 150 mÅ respectively by default)
- Minimum acceptable distance between two consecutive lines
- Smoothing applied with a `boxcar` filter before measuring the EWs. This is only for automatic line identification.

An in-depth description of these options can be found in [Sousa et al. \(2007, 2015\)](#).

Rarely `ARES` crash when measuring an absorption line. The reason is not clear, however when dealing with a large amount of spectra, it is important that the analysis moves on. However, a closer inspection usually reveal strange spectral features such as zero flux, sharp peaks in the spectra, etc. To deal with this problem, `FASMA` finds the last line which `ARES` tried to measure in the log file. This line is temporarily removed from the line list and `ARES` is restarted. The line list used for deriving parameters consists of numerous iron lines, thus removing one line will have a negligible effect on the final derived parameters.

3.2.2.3 Interpolation of atmosphere models

`FASMA` has access to both ATLAS9 models by [Kurucz \(1993\)](#) and MARCS models by [Gustafsson et al. \(2008\)](#), both are in a pre-calculated grid as described above. Let this grid be described by $\{T_{\text{eff},g}, \log g_g, [\text{Fe}/\text{H}]_g\}$, where subscript g is one of the grid points. Such a grid can be seen in [Figure 3.3](#) for $[\text{Fe}/\text{H}] = 0.00$ in the T_{eff} range; 3000 K to 10 000 K. For visualisation the location of the Sun is shown as well. The colour scale corresponds to the temperature in the first layer of each model atmosphere, i.e. the uppermost layer. The requested value will be $\{T_{\text{eff},r}, \log g_r, [\text{Fe}/\text{H}]_r\}$. The task is now to find the surrounding grid points in the parameter space of the requested parameters. For $\log g$ and $[\text{Fe}/\text{H}]$ two neighbouring grid point are used, and for T_{eff} four surrounding grid point are used, in total $4 \times 2 \times 2 = 16$ model atmospheres for the interpolation. `FASMA` use the four surrounding grid points for T_{eff} instead of two, since the model atmosphere changes most with T_{eff} . This is common in other interpolations as well (see e.g. [Valenti and Piskunov, 1996](#)).

When the 16 model atmosphere have been located, the interpolation goes through each layer of the model atmosphere, where there typical are 72 layers, and each column of which there are six. The columns are described in [Section 2.1.1](#). The interpolation are done using the `griddata` function from `SciPy`⁴. The interpolation is linear in the parameter space. After the interpolation, the result is saved to a file in the format expected by `MOOG`.

3.2.2.4 Minimization

With the measured EWs for all the lines in the line list, we choose an atmosphere model to determine the abundances. If there is no prior knowledge of the star it is common simply to choose an atmosphere model with solar parameters as a starting point. Once the line abundances of all the iron lines has been determined, the linear correlation between the abundances and the reduced EWs (RW) a_{RW} , and the abundances and the excitation potential a_{EP} is calculated. If there is a correlation it means the model atmosphere used is wrong. Moreover, we also have to check if the mean abundance of Fe I and Fe II lines

⁴ <https://scipy.org/>

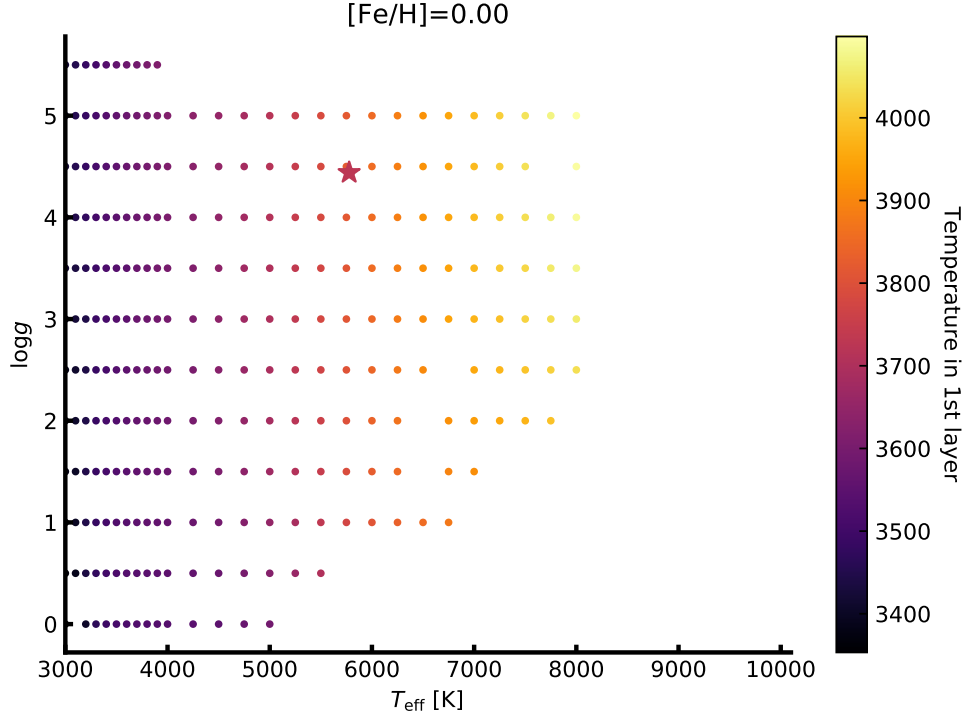


Figure 3.3: Model atmosphere grid from Kurucz (1993) at $[\text{Fe}/\text{H}] = 0.00$ between 3000 K and 10 000 K. The grid extends to higher T_{eff} , but these are not considered in this thesis.

are equal, and last if mean abundance of the Fe I lines is equal to the input $[\text{M}/\text{H}]$ of the atmosphere model⁵. If one of these four criteria does not pass, then the atmosphere model is wrong, and we have to search for a new one. A common way to do this, is by combining the indicators into a scalar value:

$$f(\{T_{\text{eff}}, \log g, [\text{Fe}/\text{H}], \xi_{\text{micro}}\}) = \sqrt{a_{\text{EP}}^2 + a_{\text{RW}}^2 + \Delta\text{Fe}^2}, \quad (3.9)$$

where a_{EP} is the correlation between abundances and excitation potential, a_{RW} is the correlation between abundances and RW, and ΔFe is the difference between the mean abundances of Fe I and Fe II. This scalar function can be minimized using standard minimization procedures as the simplex downhill among others. However, there is another approach that takes into the account the information stored in these indicators. For example, if a_{EP} is positive it means T_{eff} has to be increased by an amount correlated by the numerical value of a_{EP} . In the same way, a non-zero a_{RW} means ξ_{micro} has to be changed, and ΔFe is an indicator for $\log g$. In the end it is a vector function being minimized which are more difficult, however we are not minimizing this using standard mathematical methods, but rather using the physical knowledge. This minimization is useless for anything else, but it is excellent for this. The vector function has the form:

$$f(\{T_{\text{eff}}, \log g, [\text{Fe}/\text{H}], \xi_{\text{micro}}\}) = \{a_{\text{EP}}, a_{\text{RW}}, \Delta\text{Fe}, \text{Fe I}\}. \quad (3.10)$$

The abundances of Fe I lines versus EP and RW are shown in Figure 3.4 for the planet host star

⁵ We use Fe I instead of Fe II lines for this, since they are more numerous.

HATS-1. The three rows are for three different model atmospheres. From upper to lower:

- Converged: $T_{\text{eff}} = 5959 \text{ K}$, $\log g = 4.59$, $[\text{Fe}/\text{H}] = -0.04$, and $\xi_{\text{micro}} = 1.05 \text{ km/s}$.
- Converged with 0.5 km/s added to ξ_{micro} .
- Converged with 500 K added to T_{eff} .

Left column show the abundances against the EP, and the right column is abundances against RW.

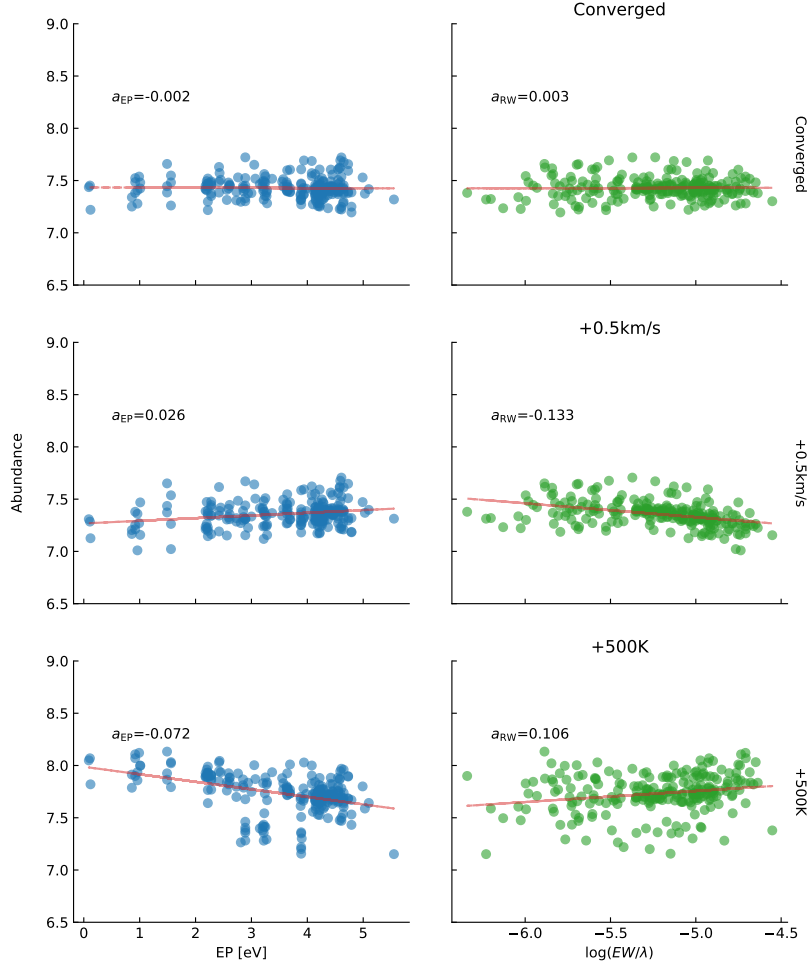


Figure 3.4: The abundances of Fe I for the planet host star: HATS-1. Upper plot: Converged parameters (see text for stellar parameters for this star). Middle plot: Converged parameters with 0.5 km/s added to ξ_{micro} . Lower plot: Converged parameters with 500 K added to T_{eff} .

Option: outliers - The minimization with the different options is depicted in Figure 3.6. In each iteration where convergence is not reached, the input metallicity is changed to that of the average output metallicity using the Fe I lines. FASMA is able to set one or all of the four atmospheric parameters to a fixed value, and when it reach convergence it checks if there are any outliers in the abundances. These outliers are likely to come from a bad measurement of the EW of the given line. This can be due to line blending or a poor spectral reduction. These can be removed, either:

- All outliers above 3σ once; minimization routine is restarted after removal of outliers.
- All outliers above 3σ iteratively; minimization routine is restarted after removal of outliers each time.
- One outlier above 3σ (with the highest deviation) is removed iteratively; minimization routine is restarted after removal of outliers each time.

It is optional to remove any outliers, but recommended.

All restarts of the minimization will start at the previous best found parameters. For the latter two where outliers are removed iteratively, this will continue until no outliers are present. An optical line list like the ones by [Sousa et al. \(2008\)](#); [Tsantaki et al. \(2013\)](#) have been tested thoroughly and due to the large amount of lines it is safe to remove a larger amount of lines and still obtain reliable parameters, thus using the first option is common here. However, with a less tested line list, like the one by [Andreasen et al. \(2016\)](#) (and refined in [Andreasen et al. \(2017a\)](#)), one should remove outliers more carefully, and it is recommended that one outlier is removed iteratively.

Option: fix ξ_{micro} - Sometimes the minimization can not reach convergence with all parameters free. The first approach to progress is to fix ξ_{micro} to a value. This parameter is known to depend on the spectral type (see e.g. [Tsantaki et al., 2013](#), and references therein). This is also shown in Figure 3.5 for a sample of 583 stars analysed with FASMA. FASMA use one of two empirical relations to fix ξ_{micro} if this is close to either 0km/s or 5km/s and $|a_{\text{RW}}| > 0.050$ at the end of the minimization. The empirical relations are:

$$vt = \begin{cases} 6.935 \cdot 10^{-4} T_{\text{eff}} - 0.348 \log g - 1.437 & \text{For } \log g \geq 3.95 \\ 2.72 - 0.457 \log g + 0.072 \cdot [\text{Fe} / \text{H}] & \text{For } \log g < 3.95, \end{cases} \quad (3.11)$$

where the first case is from [Tsantaki et al. \(2013\)](#) and the latter case is from [Adibekyan et al. \(2015\)](#). In this way ξ_{micro} is changed in each iteration according to one of these relations. This option is called `autofixvt` in Figure 3.6.

Option: Change line list - After the minimization, it happens that the derived T_{eff} is below 5200 K. At this temperature it is well known that the line list by [Sousa et al. \(2008\)](#) does not work well. Some of the lines start to be blended for lower T_{eff} , thus giving poor measurements of some EWs. This is something that was corrected by [Tsantaki et al. \(2013\)](#), who created a subset of the previous iron line list. This smaller line list are able to successfully derive T_{eff} below 5200 K. Therefore, if the option `teffrange` is on (which is highly recommended), the line list by [Sousa et al. \(2008\)](#) will simply be converted to the smaller line list by [Tsantaki et al. \(2013\)](#) if T_{eff} is below this threshold, and the minimization will be restarted. This conversion happens after the convergence.

Option: Refine results - Last there is an option, `refine`. This apply more strict criteria for the indicators to reach convergence, thus making the minimization less sensitive to the initial guess since it

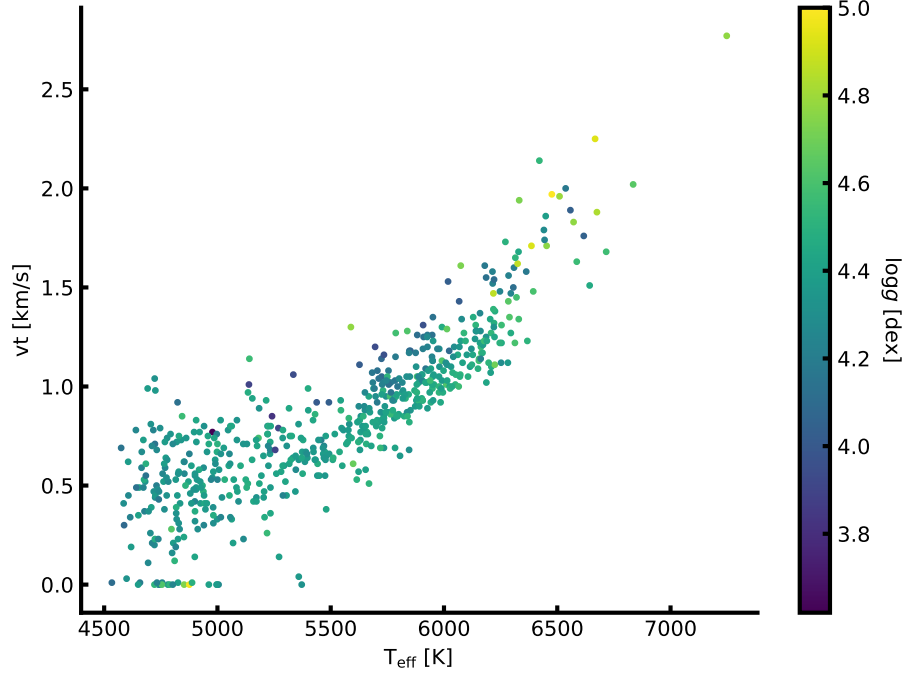


Figure 3.5: ξ_{micro} dependence on T_{eff} and $\log g$ for a sample of 583 stars.

could otherwise reach convergence from one “side” of the parameter space. The default criteria are:

$$a_{\text{EP}} = 0.001$$

$$a_{\text{RW}} = 0.003$$

$$\Delta\text{Fe} = 0.001.$$

The criteria for a_{RW} is not as strict as a_{EP} since this indicator can change rapidly with small changes in ξ_{micro} , thus a very strict criteria might never lead to convergence. Convergence is reached once all of the above criteria are met, and the input and output metallicity are identical. If one or more of the parameters are fixed, the corresponding criterion is simply set to 0 and effectively ignored, thus not changing the parameter.

Stepping in each iteration - For each iteration, the change to be applied for the atmospheric parameters are defined by adding the following:

$$T_{\text{eff}} : 2000 \text{ K} \cdot a_{\text{EP}} \tag{3.12}$$

$$\xi_{\text{micro}} : 1.5 \text{ km/s} \cdot a_{\text{RW}} \tag{3.13}$$

$$\log g : -\Delta\text{Fe} \tag{3.14}$$

to each parameter. Note again that metallicity is simply changed to the the output metallicity of the previous iteration. These are empirical relations. Note that by changing e.g. T_{eff} not only is a_{EP} affected, but the other indicators as well as seen in Figure 3.4. This inter-dependency between the parameters

is ignored by FASMA as it is not a simple problem to solve. The stepping presented above is chosen to rapidly reach convergence, without causing problems for the inter-dependency. This minimization is thus build to apply a standard method, curve-of-growth analysis, using as few calls to the time consuming part, which is the calculation of the abundances with MOOG.

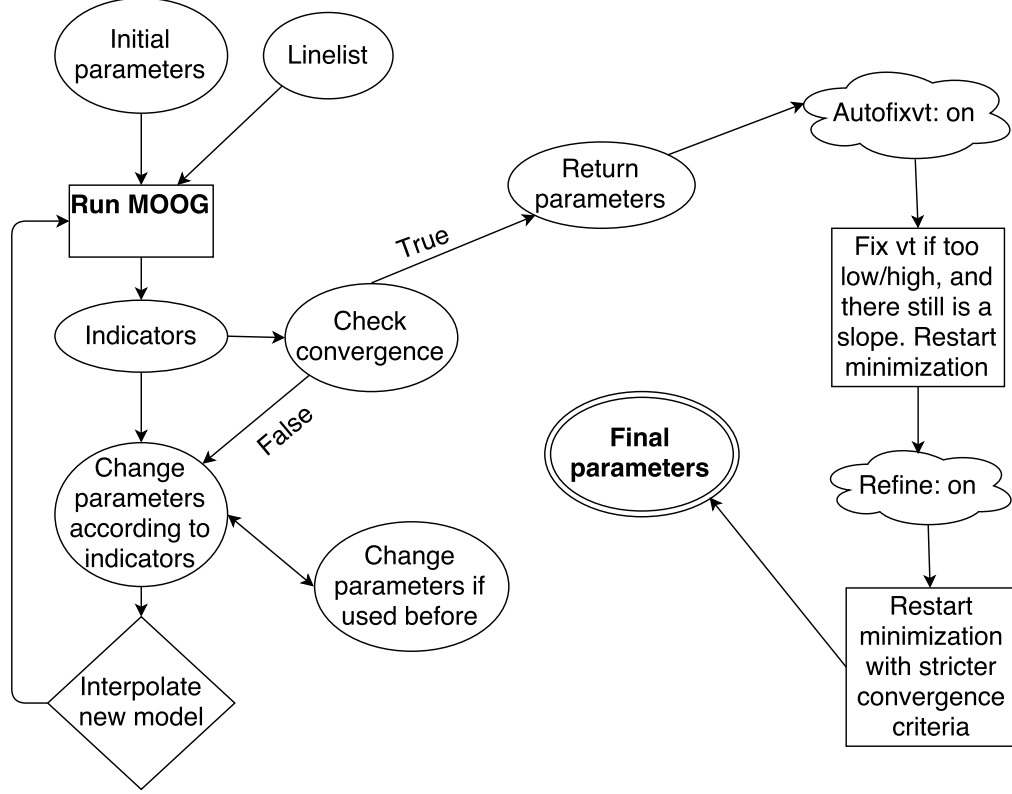


Figure 3.6: Overview of the minimization for FASMA. Credit: [Andreasen et al. \(2017b\)](#).

3.2.2.5 Error estimate

The error estimate is based on the same method presented in [Neuforge-Verheecke and Magain \(1997\)](#). The error on ξ_{micro} corresponds to the 1σ statistical error on the slope of the linear regression between Fe I abundances and RW. The error on T_{eff} is the statistical error on the slope between Fe I abundances and EP as well as the uncertainty in ξ_{micro} . The error for $[\text{Fe}/\text{H}]$ corresponds to the dispersion of the Fe I abundances as well as the uncertainties in ξ_{micro} and T_{eff} . The error in $\log g$ corresponds to the dispersion in the pressure sensitive Fe II abundances.

3.2.2.6 Testing FASMA

Parameters were derived for a 582 sample presented in [Sousa et al. \(2011\)](#) with FASMA as a test. The results were compared with [Sousa et al. \(2011\)](#) since the method is the one previously used in the Porto group, thus making a fair test.

ARES was used to measure the EWs. ARES can give an estimate of the S/N by analysing the continuum in certain intervals. For solar-type stars the following intervals work well: 5764-5766 Å, 6047-6053 Å, and

6068–6076 Å. From the estimated S/N, **ARES** can give an estimate on the very important **rejt** parameters (see [Sousa et al., 2015](#), for more information).

After measuring the EWs with **ARES**, **FASMA** was used to determine the stellar atmospheric parameters. The results are presented in Figure 3.7 which shows T_{eff} , $\log g$, $[\text{Fe}/\text{H}]$, and ξ_{micro} for **FASMA** against those of [Sousa et al. \(2011\)](#). The sample contains stars with T_{eff} too cold for the line list used. As described in Section 3.2.2.4 the line list by [Sousa et al. \(2008\)](#) should be converted to the line list presented in [Tsantaki et al. \(2013\)](#). However, since this line list was not available when [Sousa et al. \(2011\)](#) derived parameters, the **teffrange** option was left off in order to make a fair comparison for **FASMA**.

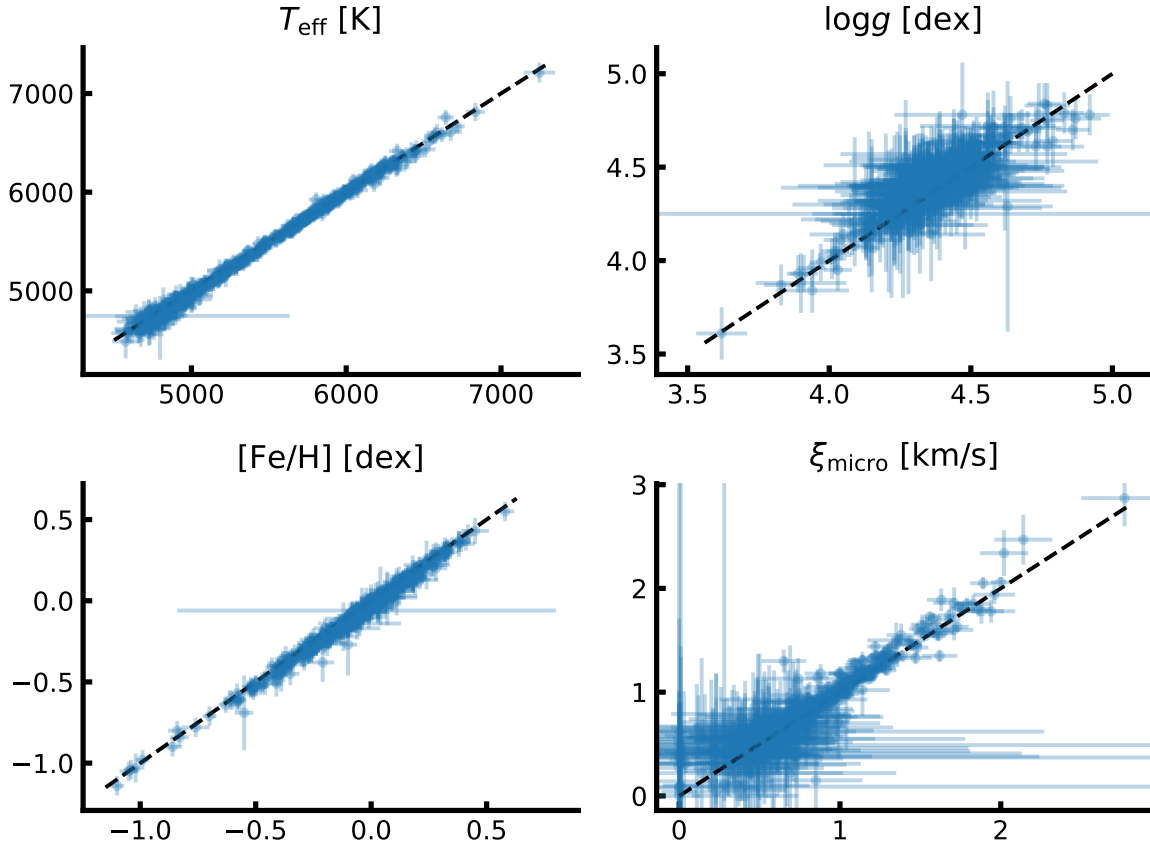


Figure 3.7: Stellar atmospheric parameters derived by **FASMA** compared to the sample by [Sousa et al. \(2011\)](#). The x-axis in all plots shows the results from **FASMA**, while the y-axis shows the parameters derived by [Sousa et al. \(2011\)](#).

The mean of the difference between parameters from [Sousa et al. \(2011\)](#) and those by **FASMA** are presented in Table 3.1. The comparison is very consistent, as expected, and the small offsets are within the errors except for metallicity. This can be due to different versions of **MOOG**, measured line lists (i.e. using slightly different settings/version of **ARES** to measure the EWs), interpolation of atmosphere grid, and minimization routine. Most likely the difference will be due to the different **rejt** parameters used in **ARES**, which can alter the EWs systematically and hence the metallicity. To test this hypothesis 20 randomly stars with different T_{eff} were selected and the EWs directly from [Sousa et al. \(2011\)](#) were used to derive parameters. The results are presented in the last column of Table 3.1. Note that the *log gf*

values from the original line lists by [Sousa et al. \(2011\)](#), which used the MOOG 2002 version, were not changed for the 2014 version of MOOG. This might lead to some errors as well. However, the offsets are very small and are compatible with the errors on parameters normally obtained from high-quality spectra.

Table 3.1: Difference in derived parameters by [Sousa et al. \(2011\)](#) and FASMA. The second column is the mean difference with EWs measured by ARES in FASMA, while the third column is the mean difference using 20 randomly stars with the exact same EWs from [Sousa et al. \(2011\)](#).

Parameter	Mean difference	Same line list
T_{eff}	$(16 \pm 36) \text{ K}$	$(21 \pm 11) \text{ K}$
$\log g$	$(-0.04 \pm 0.07) \text{ dex}$	$(-0.007 \pm 0.009) \text{ dex}$
$[\text{Fe} / \text{H}]$	$(0.03 \pm 0.02) \text{ dex}$	$(0.004 \pm 0.009) \text{ dex}$
ξ_{micro}	$(-0.04 \pm 0.14) \text{ km/s}$	$(0.04 \pm 0.02) \text{ km/s}$

NIR spectroscopy of FGK stars - towards M stars

Promises are only words until more than words are required.

Terry Brooks

It is time to apply the theory and methodology on some real data. The tools presented above will be used on NIR spectra of three stars. The goal is to derive parameters in the NIR. The reason for using the NIR part of the spectrum rather than the optical part is, that it is better suited for characterisation of the coolest stars, M stars. These stars are interesting for many reasons (see Chapter 1): 1) They make up around 75% of the stars in our galaxy and 2) they are known to be prone to form small rocky planets rather than giant planets. There is the compilation of a NIR iron line list for deriving stellar atmospheric parameters. This line list was tested against the well-studied solar-type star, HD 20010 in [Andreasen et al. \(2016\)](#). Later a second version of the line list was made. This was tested again on HD 20010 and additionally on two cooler stars, Arcturus and 10 Leo in [Andreasen et al. \(2017a\)](#). A small summary of the stars and their characteristics can be found in Table 4.1. A plot of the spectra of the four stars analysed in this chapter is shown in Figure 4.1. More details are provided in the individual sections below for each star. Last is the analysis of a range of synthetic spectra from the PHOENIX spectral library ([Husser et al., 2013](#)), with T_{eff} lower than analysed in previous stars with the methodology described above in Section 3.2.2. However, before diving into the results of the analysis it is important to describe how the NIR line list was compiled, and why and how it was later refined.

Table 4.1: Summary of the four stars used in this thesis. The stellar parameters are an average from the PASTEL catalogue ([Soubiran et al., 2016](#)) (see text for details), except the parameters for the Sun.

Star	Spectrographs	Resolution	T_{eff} (K)	$\log g$ (dex)	ξ_{micro} (km/s)	[Fe/H] (dex)
Sun	FTS	600 000	5777	4.44	1.00	0.00
Arcturus	FTS	100 000	4300 ± 111	1.60 ± 0.29	1.93 ± 0.17	-0.54 ± 0.11
HD 20010	CRIRES	100 000	6152 ± 95	3.96 ± 0.11	1.17 ± 0.24	-0.27 ± 0.06
10 Leo	CRIRES	100 000	4742 ± 61	2.76 ± 0.17	1.45 ± 0.08	-0.03 ± 0.02

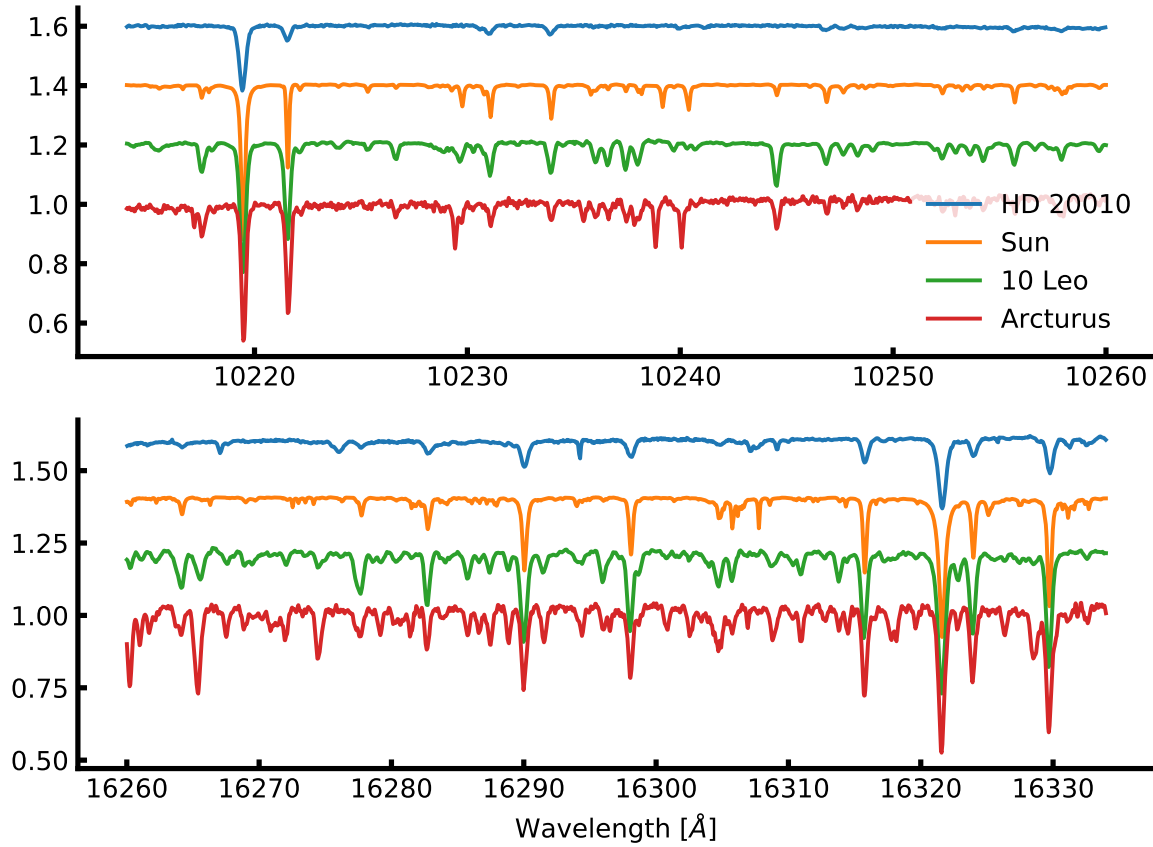


Figure 4.1: Spectrum of HD 20010 (blue), the Sun (orange) 10 Leo (green), and Arcturus (red) in two different spectral regions. The spectra are all normalised to 1, but the flux of HD 20010, the Sun, and 10 Leo is added with 0.2, 0.4, and 0.6, respectively, for visual effect. The *upper* panel is part of the J band, while the *bottom* panel is part of the H band.

4.1 The creation of a NIR line list

Although previous work (see e.g. [Önehag et al., 2012](#); [Shetrone et al., 2015](#); [Lindgren et al., 2016](#)) have compiled some NIR line lists for different purposes, there still does not exist an iron line list to determine stellar atmospheric parameters from high S/N and high resolution spectra. With the advancement of NIR high resolution spectrographs the time has arrived to compile such a line list, which should be properly tested (used to determine parameters of well known stars).

As discussed extensively in Chapter 2 and Chapter 3, an atomic line list is needed for employing the method of deriving the stellar atmospheric parameters used in this thesis. This line list is composed by neutral and ionized iron lines in the NIR. This has already been mentioned in Chapter 2. Here the process will be explained in greater detail below for the two versions presented in [Andreasen et al. \(2016\)](#) and [Andreasen et al. \(2017a\)](#), respectively.

4.1.1 Measuring the EWs and first filtering

The first version of a NIR iron line list for determining stellar atmospheric parameters of high resolution and high S/N spectra were presented in [Andreasen et al. \(2016\)](#). Other NIR line lists exist such as the one from [Önehag et al. \(2012\)](#); [Lindgren et al. \(2016\)](#) for utilising the synthetic method described above of high resolution spectra. Their line list covers the J band in the NIR and consists of 48 lines of different elements. For the line list presented here all iron transitions between 10 000 Å to 25 000 Å¹ were downloaded from the VALD database ([Piskunov et al., 1995](#); [Kupka et al., 2000](#)), only including Fe I and Fe II transitions. In total were 50 198 Fe I and 28 339 Fe II lines respectively acquired.

The EW of all lines were measured in the solar atlas obtained by ([Hinkle et al., 1995b](#)). The EWs were measured using ARES due to the large amount of lines and to be as consistent as possible in the measurements. Since ARES expects a 1D spectrum with equidistant wavelength step², the solar spectrum was interpolated onto a regular wavelength grid of 0.01 Å. This did not change the appearance, and hence not the EW, of the final spectrum. This wavelength step is equivalent to a spectral resolution of 1 500 000 at 15 000 Å. The S/N for the solar atlas varies between 300 to 2000 across the spectrum, but is generally of a very high quality.

The EWs were measured by fitting Gaussian profiles to the spectral lines. For a given line, ARES outputs the central wavelength of the line (provided in the line list), the FWHM maximum of the fitted line, the number of lines fitted for the final result (in case of blending), the depth of the line, and the EW of the line. In the latest version of ARES, the error of the EW is also provided ([Sousa et al., 2015](#)).

As a first selection step, lines were discarded according to the following four criteria:

- Lines with EW lower than 5 mÅ: these lines can be problematic to see in spectra with lower S/N or spectra with many spectral features. Therefore the measurements of these lines are less reliable than stronger lines.
- Lines with EW higher than 200 mÅ: These lines are too strong to be fitted with a Gaussian profile. These lines might also be saturated and do not fall in the linear regime of the curve-of-growth (see Figure 2.5).
- Lines where the total number of fitted lines are 10 or higher meaning the presence of severe blending.

¹ That is equivalent to the YJHK bands.

² This is changed in the newer version of ARES ([Sousa et al., 2015](#)).

- If the fitted central wavelength is more than 0.05 \AA away from the wavelength provided by VALD3 to avoid false identification. This should also remove some blended lines.
- Removal of lines with EP higher than 5.5 eV . This cut was inspired by available EPs in the optical (see e.g. [Sousa et al., 2008](#)), thus the optical method is being reproduced for the NIR which is one of the goals with this thesis.

After this removal the number of Fe I and Fe II lines were reduced to 6060 and 2735, respectively.

4.1.2 Visual removal of lines

At this point a visual inspection was necessary. All atomic data for possible transitions from all elements were downloaded from the VALD3 database in a 3 \AA window around each of the nearly 9000 iron lines from the previous step. For each small spectral window, all absorption lines (including the iron line(s)) were located in a plot of the solar spectrum. An iron line was discarded if another line had the same central wavelength and/or the absorption line were severely blended. Most of the discarded iron lines had high EP, which are weak compared to the low EP lines. Therefore, it is fair to assume that many of these iron lines were falsely identified as another stronger line from another element. After the visual removal the number of Fe I and Fe II lines were reduced to a mere 593 and 22, respectively. In Figure 4.2 is a case where too many lines are present near the iron line of interest (green line in the middle). The green lines are all iron lines in the spectral region, while the orange lines are other elements or molecules. The depth and transparency is a measure by the line strength given by

$$\text{strength} = \log gf - \chi\Theta, \quad (4.1)$$

where $\Theta = 5040 \text{ K}/T_{\text{eff}}$ (solar temperature is used here). Note that this strength of the lines does not include any abundance information, and should therefore be a guide rather than an actual measure.

For some of the absorption lines it was not clear which element was causing it. These lines were marked for further investigation with synthesis as described below.

4.1.3 Synthetic investigation

For the lines marked above for further investigation an even broader window of 6 \AA was used. Once again, all atomic data for possible transitions were downloaded from the VALD3 database in these spectral windows. MOOG was used with the `synth` driver to create a synthetic spectrum using a solar atmosphere model with $T_{\text{eff}} = 5777 \text{ K}$, $\log g = 4.438$, $A(\text{Fe}) = 7.47$, and $\xi_{\text{micro}} = 1.00 \text{ km/s}$. The iron abundance (7.47) is from [Gonzalez and Laws \(2000\)](#), while the overall metallicity for the solar atmosphere model is $[\text{M}/\text{H}] = 0.00$ by definition. This step is different from the step visual inspection done in Section 4.1.2 since synthetic spectra were created here. This was done for all spectral windows for three different iron abundances $[\text{Fe}/\text{H}] = \{-0.20; 0.00; 0.20\}$ in order to identify iron lines and their impact on the synthetic spectra. The metallicity, $[\text{M}/\text{H}]$, was kept fixed at 0.0. Before creating a synthetic spectrum all elements which are more than singly ionised were removed since MOOG does not allow these. An example of the three synthetic spectra can be seen in Figure 4.3. Here the neutral iron line at 1550.439 \AA was investigated. The three coloured curves are synthetic spectra with the three different $[\text{Fe}/\text{H}]$. The upper plot shows the result with the full VALD3 line list, while in the lower plot the iron line was removed from

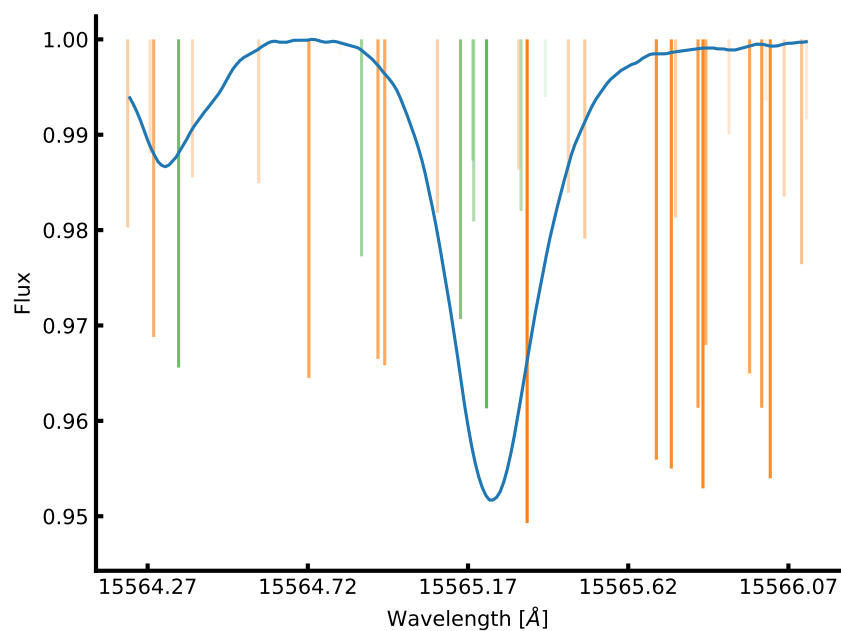


Figure 4.2: Solar spectrum (blue) with all iron lines in the spectral region (green) and other elements (orange). The depths and transparencies of the vertical lines are a measure of the line strengths (see Equation 4.1 for details). This is a case where the iron line is discarded due to blending, which is clear in the left wing of the central absorption line.

the line list. The grey curve is the solar atlas for reference. Note that it is not the purpose to match a synthetic spectrum to the solar atlas.

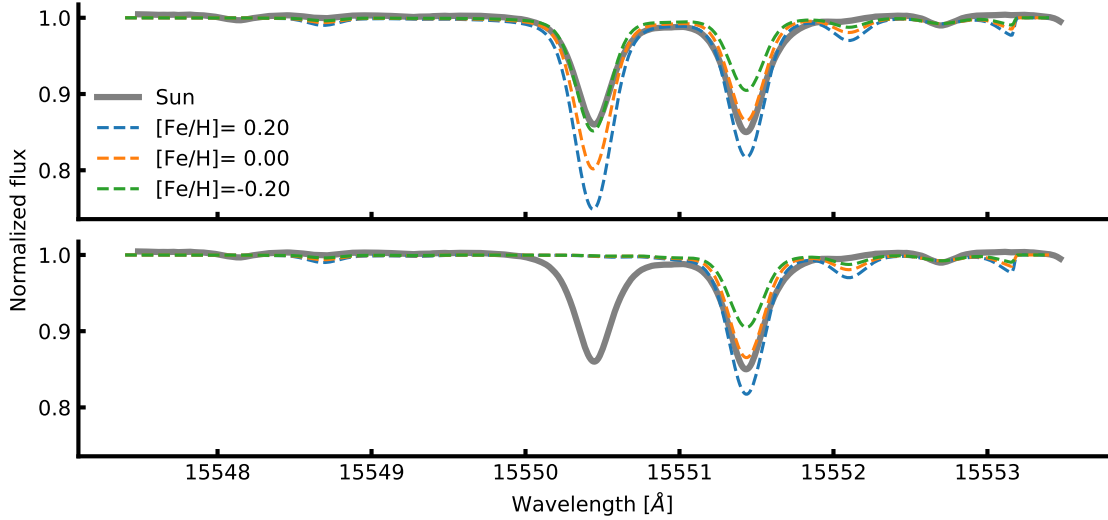


Figure 4.3: The three coloured curves represent different iron abundance, $\{-0.20; 0.00; 0.20\}$ compared to solar abundance. The grey curve is the solar atlas for reference. In this case the iron line at 15 550.439 Å was investigated. *Upper panel:* Synthetic spectra were computed using the full VALD line list in the spectral range for the three different iron abundances. *Lower panel:* Same as the upper panel, but with the iron line removed from the line list. Since the synthetic spectra shows no features at this absorption line anymore, it is a fair assumption to say the iron line is the cause of this absorption line.

If the synthetic spectra shows variation at the iron line of interest, then it is assumed that the iron line is the cause for the absorption line. As a simple test, the iron line was also removed from the line list used to create the synthetic spectra. If the iron line in the synthetic spectra disappeared, it was a clear signal that this line can be used in the final iron line list (this can be seen clearly in the lower plot of Figure 4.3). In some cases two iron lines had the same or very similar wavelength, and this technique was used to include the correct iron line. In cases where both iron lines causes the absorption line, they were both discarded since they are blended. In theory both iron lines will contribute to the absorption, however one of the contributions might be negligible, hence only one of the lines will be discarded.

In a few cases two iron lines had the same wavelength and EP but different $\log gf$. In these cases the two iron lines they can be combined into a single line by adding their gf values. After this step, there were 414 Fe I lines and 12 Fe II lines, respectively.

4.1.4 Calibrating the line list: astrophysical $\log gf$ values

These lines were collected into a single line list in the format required by MOOG (Snedden, 1973) and the line abundance were measured by all lines using the solar atmosphere model described above. If the derived abundance for a single line differs by more than 1.0 dex from the solar iron abundance, the line was discarded. All lines before this step can be seen in Figure 4.4 with all lines discarded marked in red.

After the removal of the lines mentioned above, the final line list is almost compiled. At this point the line list has to be calibrated. This is done by changing $\log gf$ so the line abundance for all iron lines

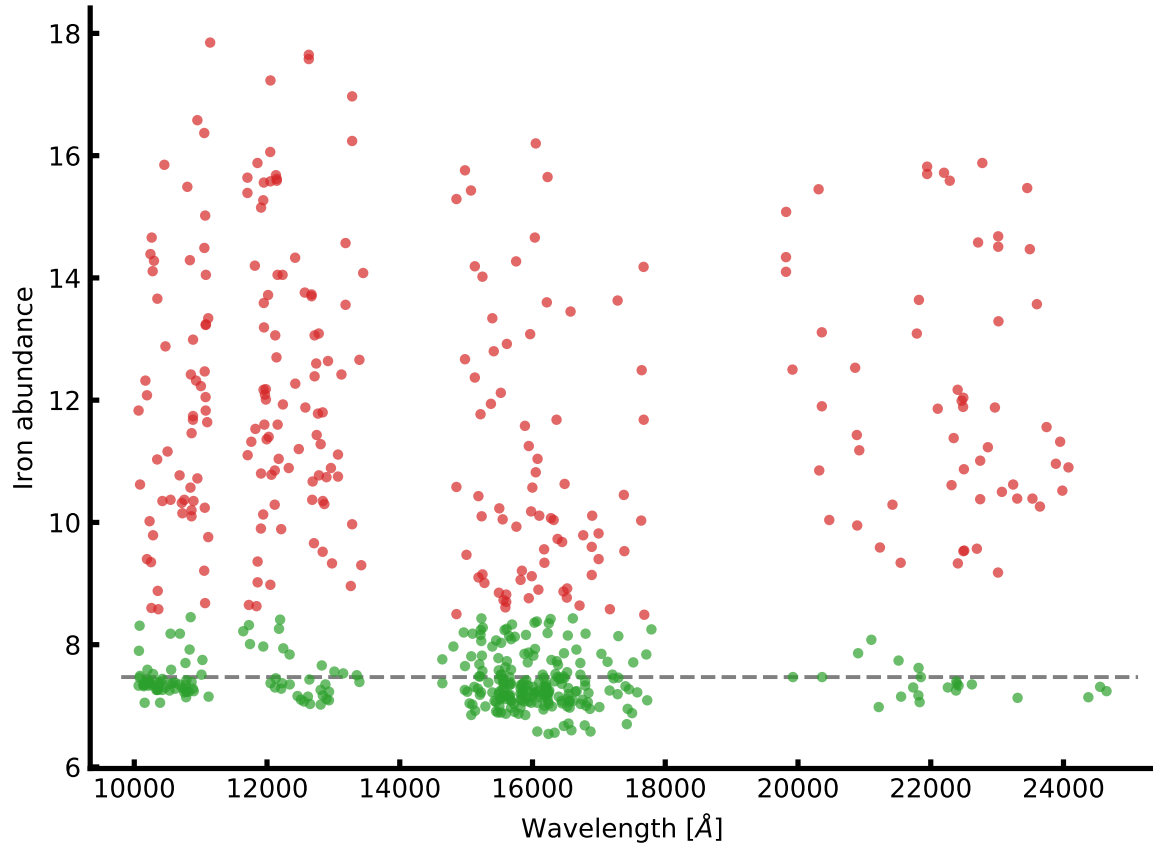


Figure 4.4: Line abundance of all iron lines before calibrating the $\log gf$ values. The green points are the points with a deviation less than 1.0 dex from the solar iron abundance. All the red points are discarded. The horizontal line shows the solar iron abundance.

are 7.47 when using the solar atmosphere model mentioned above. There is an anti-correlation between the abundance of a line and $\log gf$. This means a simple bisector minimization can be used to locate the $\log gf$ that gives the desired abundance. This was done for all the iron lines at this stage.

Note If the setup³ used to determine the parameters is changed, then it is important to calibrate the $\log gf$ values for the line list again. This includes the type of model atmospheres used (e.g. ATLAS9 or MARCS), the interpolation code to generate a model atmosphere from the grid, or the settings of the radiative code, here MOOG, and even the settings used in the radiative transfer code, i.e. the specific physics used. In the results listed below the setups are identical, except for the work done with synthetic spectra (see Section 4.7). There both ATLAS9 and MARCS model atmospheres were used, and a calibrated set of $\log gf$ values are available for both setups.

4.1.5 Removal of high dispersion lines

The line list calibrated above was used to derive parameters for HD 20010 (see Section 4.2), however the derived parameters showed poor results when compared to the literature values. This lead to the following test to identify lines which show high dispersion:

A Gaussian distribution was made for the EW of each line centred on the EW itself,

$$f(x, EW, \sigma) = \frac{1}{\sqrt{2\pi}\sigma} e^{-\frac{(x-EW)^2}{2\sigma^2}}, \quad (4.2)$$

where σ is the error on the EW, expressed by Cayrel (1988):

$$\sigma \simeq 1.6 \frac{\sqrt{\Delta\lambda EW}}{S/N}, \quad (4.3)$$

where $\Delta\lambda = 0.1$ and a $S/N=50$ were considered here, which is much lower than the actual S/N of the solar atlas. The search for lines to remove from the line list, in order to improve the results is as follows:

1. Make 100 draws for each EW (giving a total of 100 line lists)
2. Derive the line abundances for all 100 line lists using the solar model atmosphere and MOOG
3. Calculate the mean absolute deviation (MAD) for each line using the derived abundances
4. Locate the lines with highest dispersion in a MAD versus original EW plot (see Figure 4.5)

In the upper panel of Figure 4.5 the weaker lines (i.e. lines with lower EW) shows a higher MAD value, however this is expected since a small absolute change in the EW results in a large relative change in abundance for these lines. This does not mean these lines necessarily have a high dispersion, since it is just the expected outcome of this test. Moreover, these relatively weak lines from the solar atlas should be stronger for some other spectral types, and therefore important to include if possible. Therefore the disperse lines are found in the de-trended MAD value, where an exponential function was used for de-trending. A single point above 3σ was removed iteratively in the de-trended data. After this process there are 334 Fe I lines and 13 Fe II lines.

³ That can be different atmosphere models, interpolation codes, etc.

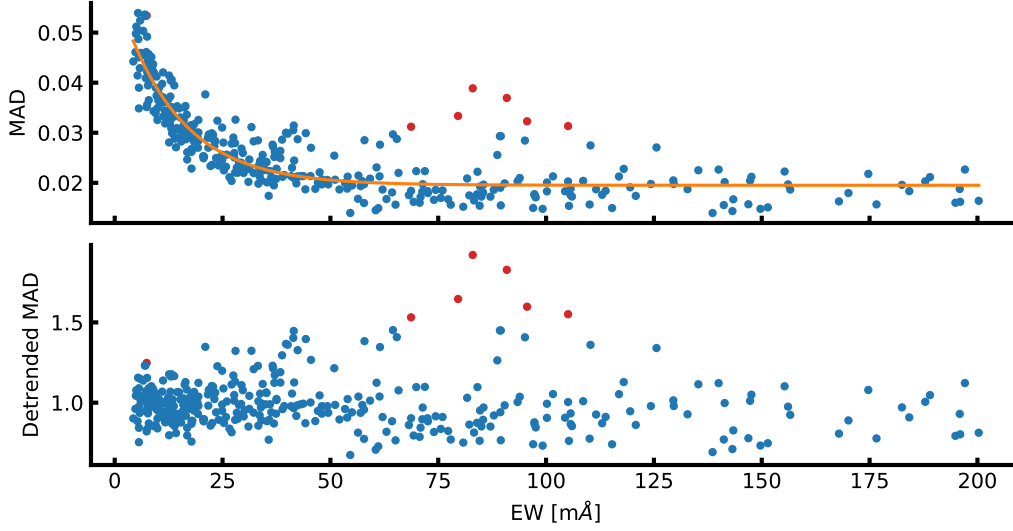


Figure 4.5: The most disperse lines. *Upper panel:* The MAD versus the original EW. The red points are the outliers which were discarded during this process. *Lower plot:* Same as above with the de-trended MAD by the exponential fit as shown in the upper panel.

4.2 HD20010

To test the NIR line list a well-studied solar-type star was needed. The spectrum for such a target needs to be available in the NIR at both high resolution and high S/N. An ideal place to look for such a star was the CRIRES-POP database (Lebzelter et al., 2012). Here, the best target for testing was HD 20010, an F8 subgiant star. At the time of writing this thesis and Andreasen et al. (2016) the spectrum of HD 20010 was not fully reduced. Here it is still contaminated by some telluric lines, and the wavelength solution used is not optimal; both which are essential, however a tedious and difficult task to accomplish.

HD 20010 star has been part of many surveys and is therefore well studied. Different parameters from the literature are listed in Table 4.2.

Table 4.2: Selection of literature values for the atmospheric parameters for HD 20010. The mean and a 3σ standard deviation is presented at the end of the table from the literature values included, which was used as a reference for the derived parameters.

Author	T_{eff} (K)	$\log g$ (dex)	[Fe/H] (dex)	ξ_{micro} (km/s)
Balachandran (1990)	6152	4.15	-0.27 ± 0.08	1.60
Favata et al. (1997)	6000	...	-0.35 ± 0.07	...
Santos et al. (2004)	6275 ± 57	4.40 ± 0.37	-0.19 ± 0.06	2.41 ± 0.41
Gonzalez et al. (2010)	6170 ± 35	3.93 ± 0.02	-0.206 ± 0.025	1.70 ± 0.09
Ramírez et al. (2012)	6073 ± 78	3.91 ± 0.03	-0.30 ± 0.05	...
Mortier et al. (2013a)	6114	...	-0.19	...
Mean	6131 ± 255	4.01 ± 0.60	-0.23 ± 0.14	1.90 ± 1.08

The data available at CRIRES-POP are in the raw format and pipeline reduced, while three small pieces of the spectrum are fully reduced on the web page⁴. The data is in the standard CRIRES format

⁴ <http://www.univie.ac.at/crerespop/data.htm>

with each fits file including four binary tables with the data from the four detectors with the same resolution in each spectrum. In the future, the final reduced data will be presented by the CRIRES-POP team. In contrast to the pipeline reduced data, this will be of higher quality, a better wavelength calibration, and telluric corrected.

The EWs were measured of the pipeline reduced spectrum, and where there was an overlap with the fully reduced spectrum, the EW was measured in both cases as a consistency check. The measured EWs from the fully reduced spectra were consistent with the measured EWs from the pipeline reduced spectra, although with less noise in the fully reduced spectral parts. As mentioned above, the Y, J, H, and K-bands, which are all available for this star, were used in this analysis. The spectra come in pieces of 50 Å to 120 Å. These pieces overlap each other, and up to five EW measurements were made for some lines. Unfortunately, wavelength calibration is a difficult task for CRIRES owing to the rather small spectral regions measured on each detector. Each calibration was performed separately for each detector and required the availability of a sufficient number of calibration lines in the respective spectral region. This was not always the case and a default linear solution was applied. A pipeline reduced spectrum shows up as a stretched spectrum if the wavelength calibration is poor compared to a model spectrum or a solar spectrum, for example. The wavelength calibration does not have any effect on the signal-to-noise ratio, which is generally high for the spectrum of HD 20010. The signal-to-noise varies between 200 and 400 for different chunks. However, the stretched spectra will most likely have an effect on the measured EWs.

The pipeline reduced spectrum for HD 20010 contains tellurics and the wavelength is shifted in radial velocity. All of these factors make the line identification very difficult, so a program was developed⁵ to properly identify the lines, which does the following:

1. Plotting the observed spectrum
2. Overplotting a model spectrum. In this particular case the solar spectrum was used since the atmospheric parameters are close enough, so the sun was able to serve as a model
3. Overplotting a telluric spectrum from the TAPAS web page (Bertaux et al., 2014)
4. Overplotting vertical lines at the location of lines in the list
5. Calculating the cross-correlation function (CCF) for the telluric spectrum with respect to the observed spectrum, locating the maximum value by a Gaussian fit, and using this to shift the telluric spectrum with the found RV
6. Performing the same as step 5, but for the model spectrum
7. Shifting the lines with the same RV as found for the model/solar spectrum

The final plot shows the shifted spectra, and the CCFs at the sides. An example of the software in use is shown in Figure 4.6. The two radial velocities (for the telluric and model spectrum) are part of the title of the plot. Once the lines were identified, the EWs were measured with the `splot` routine in *Image Reduction and Analysis Facility* (IRAF). The reason not to choose ARES for this task was to visually confirm the identification of the line given the relative poor wavelength calibration from the automatic pipeline. 249 Fe I lines and 5 Fe II EWs were measured compared to 344 Fe I lines and 13 Fe II

⁵ The program (and other small scripts) can be found here https://github.com/DanielAndreasen/astro_scripts

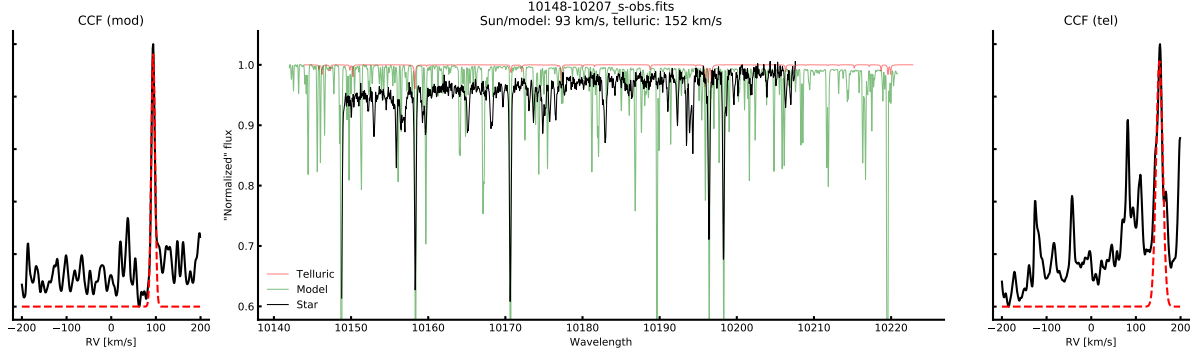


Figure 4.6: Line identification in piece of Arcturus spectrum with PHOENIX model and telluric model for correcting RV.

lines for the Sun over the whole NIR spectral region in the line list. Whenever there were more than one EW measurement of a line, due to overlap in different spectra, the average was used for the final EW. The stellar atmospheric parameters were derived using the standard procedure (see Section 3.2.2). Lines below $5 \text{ m}\text{\AA}$ were removed in order to remove the lines which are most affected by contamination from either telluric or other line blends. Additionally, a cut in EP at 5.5 eV was made since the Fe I and Fe II lines usually used for stellar parameter determination in the optical regime are also limited to similar values (see e.g. Sousa et al., 2008).

When deriving the stellar atmospheric parameters, one outlier were removed at a time (after a completed minimization) until no outliers were present. Since we could only measure 5 Fe II lines, the parameter were also derived with $\log g = 4.01 \text{ dex}$ fixed at the reference mean value (see Table 4.2). The resulting atmospheric parameters and iron abundances are presented in Table 4.3. The effective temperature, surface gravity, and metallicity agree within the errors with the literature values. Similar parameters are obtained by fixing $\log g$ to the average literature value or by leaving it free.

Table 4.3: The derived parameters for HD20010 with and without fixed surface gravity.

	T_{eff} (K)	$\log g$ (dex)	ξ_{micro} (km/s)	[Fe/H] (dex)
Literature	6131 ± 255	4.01 ± 0.60	1.90 ± 1.08	-0.23 ± 0.14
	6116 ± 224	4.21 ± 0.58	2.45 ± 0.45	-0.14 ± 0.14
	6144 ± 212	4.01 (fixed)	2.66 ± 0.42	-0.13 ± 0.29

The errors on the atmospheric parameters for HD 20010 are much higher than what is achievable with other measurements in the literature, as presented above in Table 4.2. In order to explain these errors, the abundances for all lines which have at least two measurements of the EW were calculated from the highest and lowest measured EW. The differences in abundances are presented in Figure 4.7. The very large differences (more than 0.1 dex) translate to the high errors in the parameters.

This test strongly suggest that errors in the EWs, likely due to the telluric contamination and non-optimal reduction of the spectrum (poor default wavelength calibration), are responsible for the relatively large error in the derived stellar parameters. After the first analysis of HD 20010, the CRIRES-POP team published a fully reduced spectrum of 10 Leo (Nicholls et al., 2017) with telluric correction and an optimal wavelength solution. The results obtained from this star (see Section 4.6) are very promising for the method used here, and it encourage a complete re-visit of HD 20010 once the reduction is optimal.

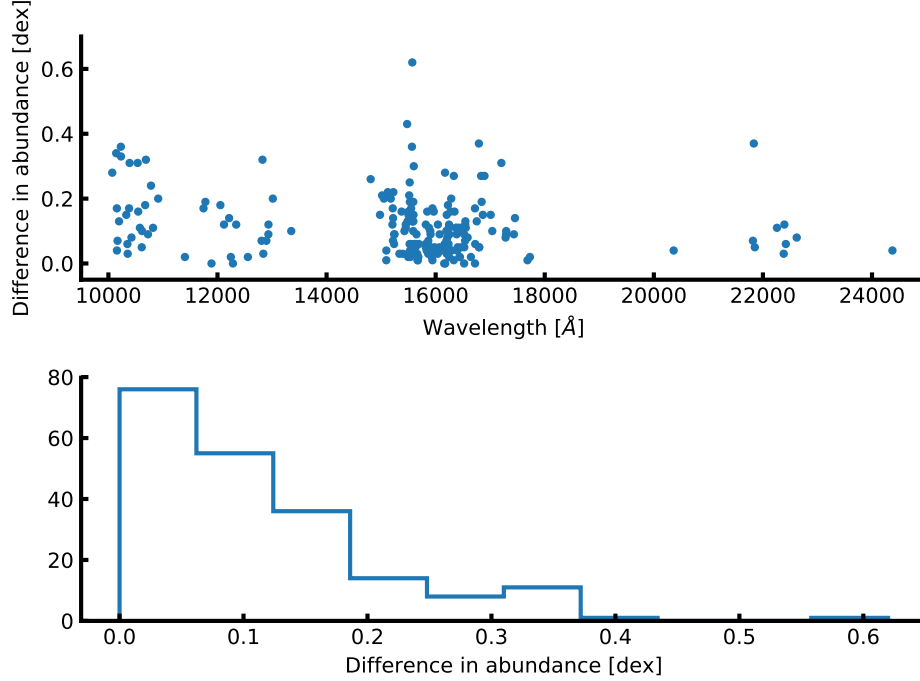


Figure 4.7: Difference in abundance for HD 20010 when multiple measurements of EW were obtained. The differences are between the lowest and highest measured EW in case of multiple measurements. This is shown against the wavelength (*upper panel*) and in a histogram (*lower panel*).

4.3 The NIR line list - toward cooler stars

As was seen in Section 4.2 the line list presented above was used to derive atmospheric parameters of HD 20010. Even though the first test of the line list was successful, it left room for improvements. The errors on the derived parameters were quite high for the spectral type compared results obtainable with a similar analysis utilising the optical spectrum (see Section 4.2 for details on this). Additionally, the derived metallicity was 0.10 dex higher than the literature values used.

If all derived parameters except metallicity are reliable (when compared to e.g. a literature value), then it suggest that the measured EW are either over- or underestimated. However, when using a line list for the first time like here, it can also suggest problems with the line list itself, most likely a bad calibration. This could have been wrong measurements of the EWs of the calibrator star, Sun in this case. This combines to several cases:

- Correct measurements of EWs of calibrator star:
 - Systematic lower measurements of EWs of target star leads to underestimated $[M/H]$
 - Systematic higher measurements of EWs of target star leads to overestimated $[M/H]$
 - Correct measurements of EWs of target star leads to correct $[M/H]$
- Systematic lower measurements of EWs of calibrator star:
 - Systematic lower measurements of EWs of target star leads to underestimated $[M/H]$

- Systematic higher measurements of EWs of target star can lead to underestimated, correct or overestimated $[M/H]$ depending on the amount of systematic higher measurements
- Correct measurements of EWs of target star leads to underestimated $[M/H]$
- Systematic higher measurements of EWs of calibrator star:
 - Systematic lower measurements of EWs of target star can lead to overestimated, correct or underestimated $[M/H]$ depending on the amount of systematic lower measurements
 - Systematic higher measurements of EWs of target star leads to overestimated $[M/H]$
 - Correct measurements of EWs of target star leads to overestimated $[M/H]$

It is important to note, that *correct* has been used here, assuming a perfect setup, that includes perfect model atmosphere, perfect radiative transfer code, etc. In reality the final $[M/H]$ (and the other parameters) measured by different groups will occasionally differ regarding the setup used (see e.g. [Hinkel et al., 2016](#)).

As described in Section 4.1 the EW of the Sun (calibrator star) was measured with **ARES**. A crucial option to set when using **ARES** is the **rejt** parameter as mentioned in Section 3.2.2.2. This option is used to place the continuum and will thus directly affect the measured EW. At the time of compiling the first version of the line list it seems the **rejt** value used did not reflect the high S/N of the spectrum, thus placing the continuum too low and thereby underestimate the EW. The **rejt** parameter used was 0.995 (S/N=200), while it should have been closer to 0.999 (S/N=1000). This might have excluded some of the weakest lines, since a cut in EW was made at 5 mÅ.

In this second version of the line list, the goal is to:

1. Make sure the EW measurements are as correct as possible by measuring them by hand
2. Free of blended lines in cooler stars (K stars in this case)

The second point is a similar exercise which was done in the optical by [Tsantaki et al. \(2013\)](#), where blended lines were removed from the larger line list by [Sousa et al. \(2008\)](#). This allowed to determine the atmospheric parameters of stars cooler than 5200 K. However, the optical spectrum still suffer for severely blended lines at low T_{eff} , thus this method does not work for M stars.

Both of the above steps were done at the same time, by measuring the EWs by hand using **IRAF**. Whenever a line was difficult to reliably measure, i.e. a consistent measurement was not possible/easy, it was discarded since it was blended. This can be seen in Figure 4.8 where the difference in the EW measurements are shown against the EWs from the first version. The average difference of the two versions is $(2.1 \pm 11.1) \text{ mÅ}$. The large deviation are due to line blending. There are some measurements of EW higher than 150 mÅ which should have been removed. These lines have not been used during the analysis, however they were kept since they might appear useful on a later stage.

With the increased access to high quality NIR spectra and the gained experience during the course of the thesis, it was possible to improve the line list by a second visual inspection on the solar spectrum.

After the new measurements of the EWs, the line list was re-calibrated according to the procedure described above. The average change in $\log gf$ is -0.062 ± 0.157 , i.e. on average the oscillator strengths are higher in the second version compared to the first version of the line list.

With the second version there are only 5 Fe II lines left which is a concern since these are crucial for the derivation of the surface gravity.

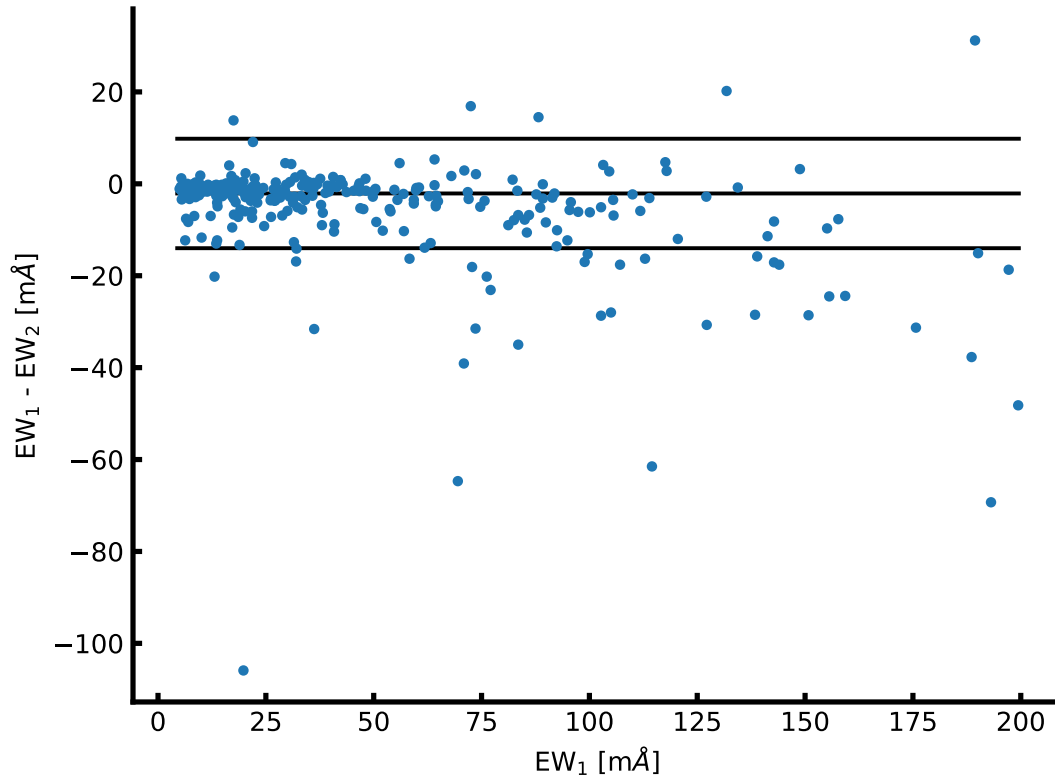


Figure 4.8: Comparison of the EW from the first version of the line list (measured with **ARES**), EW_1 , and the second version, EW_2 (measured with **IRAF**). The EWs are generally higher in the second version, with an average difference between the two version of $(2.1 \pm 11.1) \text{ m}\text{\AA}$. The three horizontal lines show the average value and the standard deviation.

4.4 HD 20010 - revisited

During the analysis of Arcturus (see Section 4.5) and 10 Leo (see Section 4.6) with the refined line list presented in Section 4.3 it was a simple task to apply the updated line list on HD 20010 a second time as a test whether it would perform similar, worse or better. This is compared to results obtained from the literature and the previous results in Section 4.2.

Therefore HD 20010 was revisited, and the atmospheric stellar parameters were derived. The measured EWs from the results above in Section 4.2 were kept, however the lines which did not make the cut in the second version of the line list were removed. Moreover, the $\log gf$ values were updated since these were re-calibrated.

At this point FASMA was fully developed and was used to obtain the results which are shown in Table 4.4 along with the results for Arcturus and 10 Leo (details on their parameters will be found below). The agreement with the adopted average literature values are better for HD 20010 compared to the results from above in Section 4.2 (especially $[\text{Fe}/\text{H}]$ and $\log g$), and smaller errors with the updated results. This first test of the line list already shows promising results. The literature values are slightly different here than compared to the first analysis of this star. This is solely because other references were used, the PASTEL catalogue (Soubiran et al., 2016). However, this does not change the improvement seen.

Table 4.4: Results for the three stars where first set of parameters are the literature values as presented in Table 4.1, second set of parameters are results with $\log g$ set to the same value during the minimization procedure as found in the literature (fixed), and last set of parameters are with all parameters free during the minimization procedure.

	HD 20010	10 Leo	Arcturus
Literature			
T_{eff} (lit.)	6152 ± 95	4741 ± 60	4300 ± 110
$\log g$ (lit.)	3.96 ± 0.19	2.76 ± 0.17	1.60 ± 0.29
$[\text{Fe}/\text{H}]$ (lit.)	-0.27 ± 0.06	-0.03 ± 0.02	-0.54 ± 0.11
ξ_{micro} (lit.)	1.17 ± 0.24	1.45 ± 0.08	1.93 ± 0.13
$\log g$ fixed			
T_{eff}	6161 ± 164	4761 ± 118	4357 ± 74
$\log g$	3.96 (fixed)	2.76 (fixed)	1.60 (fixed)
$[\text{Fe}/\text{H}]$	-0.18 ± 0.11	0.01 ± 0.07	-0.55 ± 0.04
ξ_{micro}	1.72 ± 0.44	1.25 ± 0.11	1.55 ± 0.10
All free			
T_{eff}	6162 ± 184	4805 ± 98	4439 ± 62
$\log g$	4.08 ± 0.77	2.42 ± 0.61	1.20 ± 0.20
$[\text{Fe}/\text{H}]$	-0.18 ± 0.11	-0.01 ± 0.07	-0.58 ± 0.06
ξ_{micro}	1.59 ± 0.49	1.23 ± 0.10	1.55 ± 0.10

4.5 Arcturus

Arcturus is one of the brightest stars on the Northern hemisphere with a V magnitude of -0.05 (Ducati, 2002), and is well studied (see e.g. Griffin and Griffin, 1967; McWilliam, 1990; Ramírez et al., 2013, to mention just a few), and a benchmark star in current spectroscopic surveys such as Gaia-ESO (Jofré et al., 2014; Smiljanic et al., 2014). Hence it is a prime target for testing with the numerous measurements of

the atmospheric parameters.

The atlas of Arcturus, acquired at Kitt Peak National Observatory using the FTS spectrograph at the Mayall telescope by [Hinkle et al. \(1995a\)](#), covers the spectral range of interest (YJHK bands). Strong telluric features were identified with a spectrum from the TAPAS web page ([Bertaux et al., 2014](#)) which was useful during the line identification. The atlas also comes with a telluric standard and the ratio of the two spectra in order to correct for the tellurics. The telluric spectrum from TAPAS was only used for telluric line identification. Both the telluric corrected and non-corrected spectra was used during the analysis, however the focus was on the non-corrected spectrum since it is simple to identify the telluric lines in this spectrum.

The atlas consists of both a summer observation set and a winter observation set. The two data sets have been obtained in order to minimise the effect of tellurics at different spectral regions. A comparison between the two sets of measured EWs, both the manual measurements using IRAF and the automatic measurements using ARES, are shown in Figure 4.9. The automatic EW measurements for the summer set and winter set show excellent agreement with a dispersion of 7 mÅ and a systematic difference of 0.1 mÅ, i.e. negligible. This means that the two data sets are very similar, thus it was decided to only manually measure the EWs for one set (summer). Since this is a test of the line list (rather than a study of Arcturus) and the fact that the EWs are very similar, the parameters are only derived from the summer set with the EWs measured by ARES. Parameters were derived with and without $\log g$ set to a fixed value (1.60 dex, the average literature value adopted). The derivation of the parameters followed the same procedure as described above for HD 20010 using FASMA. Again outliers in abundance were removed one at the time until there were no more outliers. The final results are presented in Table 4.4 together with mean parameters from the literature.

There is overall good agreement between the derived parameters and the average values from the literature adopted (see Table 4.4). The only parameter being difficult to measure is the surface gravity due to the low number of Fe II lines in the NIR. This was already suspected and mentioned in Section 4.3. There are also some problems determining ξ_{micro} , however this is not a major concern, since it is not as important a parameter as the other three. The derived metallicity is consistent with the literature here which is promising since there were some problems with this parameter in Section 4.2.

4.6 10 Leo

The spectrum for 10 Leo was recently made available by the CRIRES-POP team ([Nicholls et al., 2017](#)). 10 Leo is very similar to Arcturus, which is also one reason this star was the first to be fully reduced by the CRIRES-POP team. The spectrum is divided into several pieces according to the atmospheric windows in the NIR: YJ (only together), H, K, L, and M. Here the first three were used since this is the range of the line list. Some small gaps are present in the spectrum due to tellurics that could not be properly removed, low S/N, bad pixels, etc. Rather than giving an uncertain interpolation, [Nicholls et al. \(2017\)](#) decided to leave small gaps in the data. This had very little effect on this line by line analysis, however, due to those gaps, one Fe II line were not measured which are crucial to determine the surface gravity.

The approach for determining the atmospheric stellar parameters for 10 Leo is identical to Arcturus. ARES was used on each band (YJ, H, and K-band) separately. For the small gaps in the spectrum, the flux was simply set to 1, since the spectrum has already been normalised. This also prevented ARES to

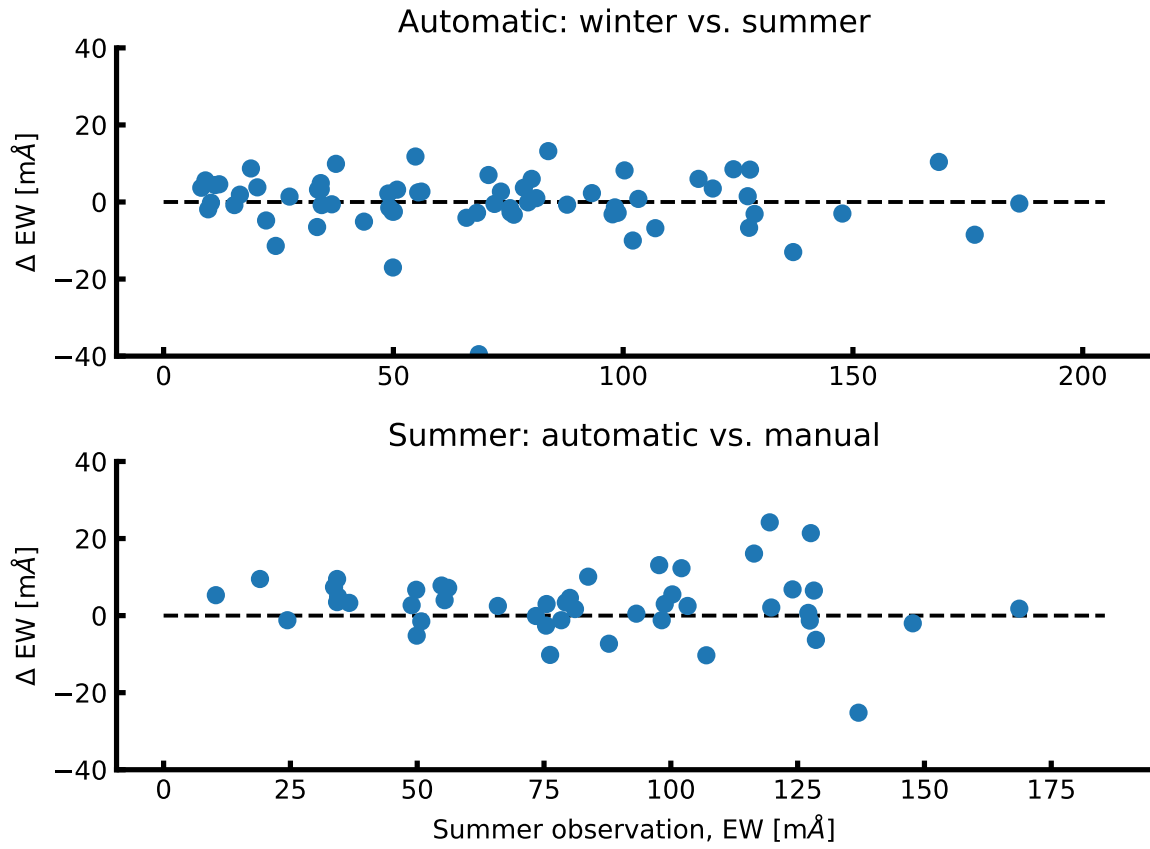


Figure 4.9: Top figure: Difference of the automatic EW measurements between the summer observations and winter observations from the Arcturus spectra. Bottom figure: Same as above, but with manual measurements from ARES (summer) and automatic measurements (summer).

identify and measure any lines in these regions. The EWs from the three regions were combined to one final line list used for the determination of the parameters. The final results can be seen in Table 4.4.

Generally the derived parameters are in excellent agreement with the literature values listed here. A 64 K difference is seen for T_{eff} with $\log g$ set as a free parameter, well within the errors. The only parameter that show a discrepancy compared to the literature value is ξ_{micro} with a difference of 0.22 km/s, which is at the limit of the errors reported. We note that this parameter is not reported in the PASTEL database, and this was a derived parameter from an empirical relation. $\log g$ was derived with large errors which is a result from the few Fe II (three lines) measured. However, the $\log g$ is not far from the literature value, only 0.34 dex lower, which is well within the large errors reported. However, it also shows it is safer to obtain $\log g$ from other more reliable methods, such as asteroseismology when possible.

Then find some reliable values instead

4.7 Synthetic cool stars

Mainly due to lack of available high quality spectra in the NIR, it is a good test to use a simulation. By deriving parameters from synthetic spectra, it is possible to carefully control the work flow, in the sense that the target parameters are known. In this section the synthetic library⁶ by Husser et al. (2013) will be used. These are synthetic spectra created from spherical symmetric PHOENIX atmosphere models under local thermodynamic equilibrium. The model atmospheres does not include dust settling since all models are hotter than 2300 K. The details for the atmosphere models can be seen in Husser et al. (2013).

For this test only the T_{eff} will vary, ranging from 3500 K to 6000 K with most densely sampled at lower temperatures (see Figure 4.10). Here $\log g = 4.5$ dex and $[M/H] = 0.00$ dex, i.e. synthesised dwarf stars with solar metallicity. Before analysing the data, the spectra was broadened to have a spectral resolution of 100 000, comparable with current and future high resolution NIR spectrographs.

In this test ARES was used to measure the EWs of as many lines from the line list (second version) as possible for each of the 12 synthetic spectra. These line list were used to derive parameters with two different model atmospheres, ATLAS9 (Kurucz, 1993) and MARCS (Gustafsson et al., 2008), with FASMA. This was done twice, with all parameters derived from FASMA (Figure 4.10), and again with $\log g$ fixed at 4.5 dex and ξ_{micro} fixed which means it is changed in each iteration (see Section 3.2.2 for details) according to an empirical relation. The latter case with fixed parameters is shown in Figure 4.11.

For the results with $\log g$ and ξ_{micro} fixed at the correct parameters during the derivation, the first thing noticed is the good agreement between the two model atmospheres. Second, the derived T_{eff} are underestimated for $T_{\text{eff}} > 4000$ K while for the two lowest T_{eff} it is the opposite case. It is important to know that the grid of ATLAS9 models only go down to 3750 K, however these synthetic spectra were included for completeness. For $T_{\text{eff}} > 4000$ K it is systematically lower by the same amount, roughly 100 K. As have been shown in the previous sections in this chapter, the methodology is reliable for T_{eff} ranging from 4300 K to 6200 K (see Table 4.4). With the consistent offset in T_{eff} , it is a clear indication that the methodology is reliable down to these temperatures.

In the case of $\log g$ and ξ_{micro} fixed the derived mean metallicity for the 12 synthetic spectra are $[Fe/H] = (-0.12 \pm 0.17)$ dex and $[Fe/H] = (-0.19 \pm 0.12)$ dex for the ATLAS9 and MARCS model atmospheres, respectively. The offset is likely to be found in the discrepancy between the model atmosphere and real data (Arcturus in this case) as shown in Figure 4.13. Here a PHOENIX synthetic spectrum with

⁶ <http://phoenix.astro.physik.uni-goettingen.de/>

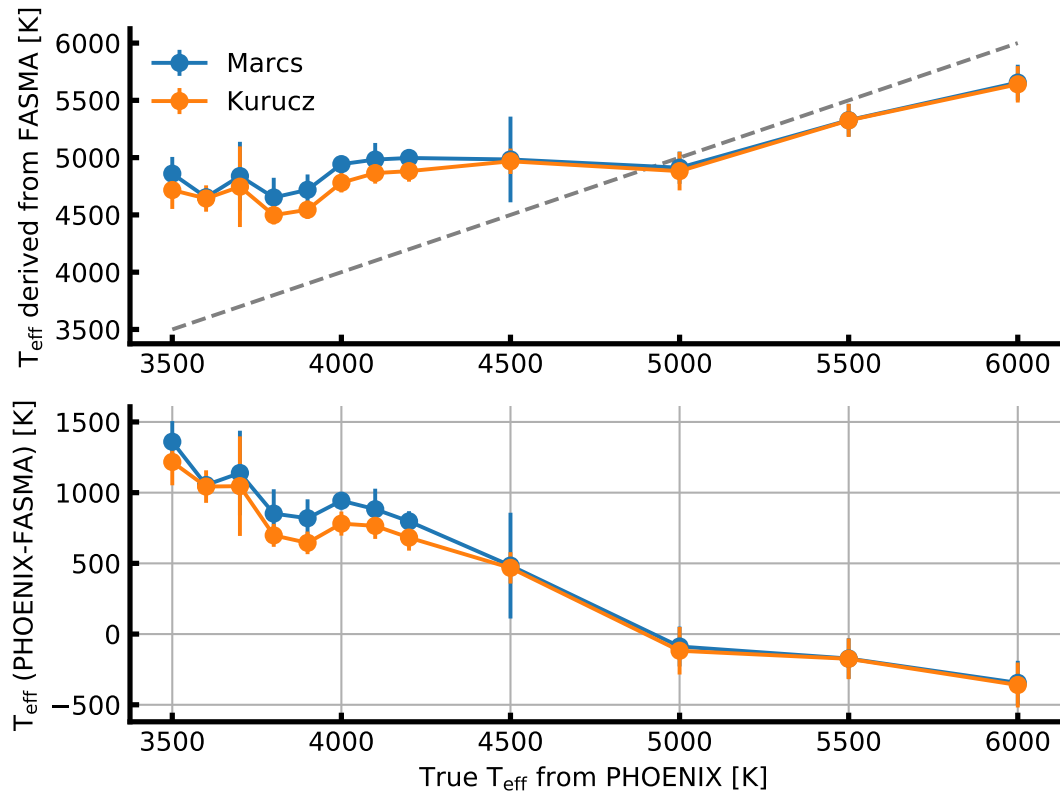


Figure 4.10: Derived parameters of 12 synthetic PHOENIX spectra with varying T_{eff} .

$T_{\text{eff}} = 4300$ K, $\log g = 1.50$ dex, and $[\text{Fe}/\text{H}] = -0.50$ dex is plotted with a piece of the Arcturus atlas from Section 4.5. The synthetic spectrum has similar parameters as Arcturus, thus they should have similar spectral features. However, in the plot the spectral lines are deeper for the PHOENIX model and there seem to be more absorption lines in this synthetic spectrum compared to the observed spectrum. This have a direct effect on the measured EWs as they will be blended and deeper than expected.

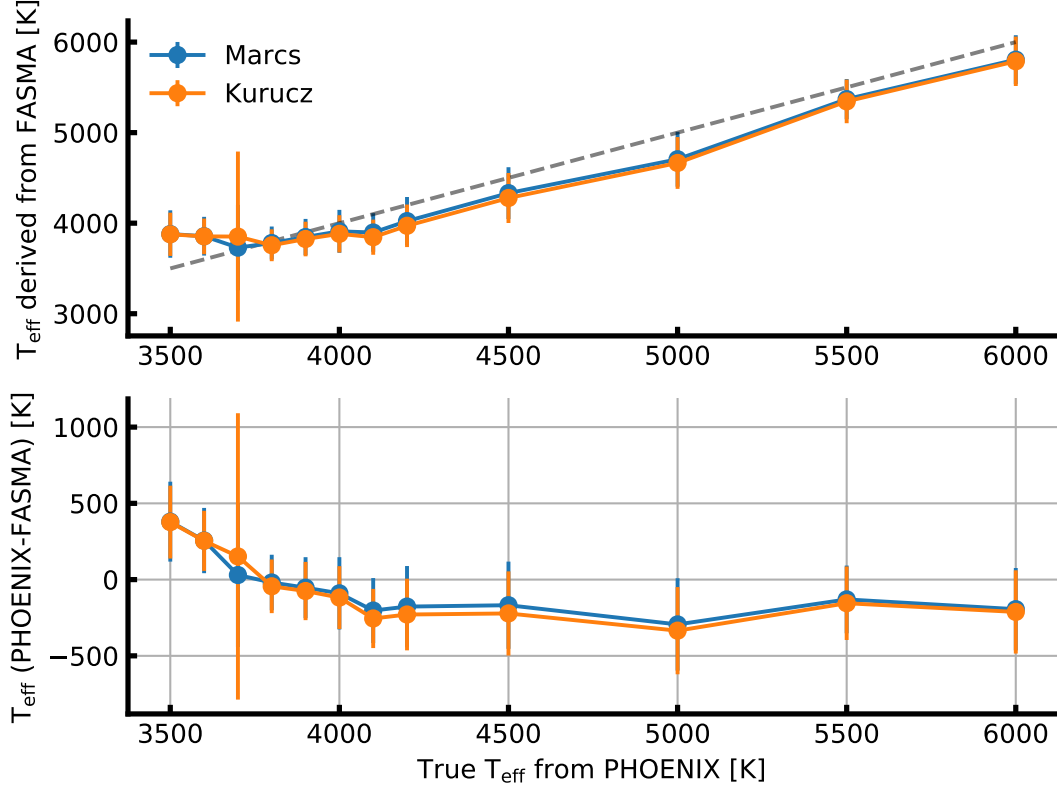


Figure 4.11: Derived parameters of 12 synthetic PHOENIX spectra with varying T_{eff} . Here $\log g$ is fixed at 4.5 dex and ξ_{micro} fixed according to an empirical relation, thus only deriving T_{eff} and $[\text{Fe}/\text{H}]$.

A comparison with EWs from the iron line list from the observed Arcturus spectrum and the synthetic spectrum which resembles Arcturus closest is shown in Figure 4.12. The EWs are clearly getting more disperse with increasing EW.

When all the parameters are derived it is a very different story for T_{eff} . In this case the T_{eff} are overestimated for the synthetic spectra colder than 5000 K. Above this limit the T_{eff} are slightly underestimated with a hint of the results getting worse further from this limit. The reason for this can partly be found in the measured Fe II lines. As mentioned before, these are used to determine $\log g$. There have been measured between 1 and 3 Fe II lines, generally fewer the lower T_{eff} is, out of 5 possible measurements. The mean derived values for the surface gravity are $\log g = (1.11 \pm 1.63)$ dex and $\log g = (1.38 \pm 1.45)$ dex for ATLAS9 and MARCS model atmospheres, respectively. Similarly for the metallicity the following mean values are $[\text{Fe}/\text{H}] = (-0.73 \pm 0.37)$ dex and $[\text{Fe}/\text{H}] = (-0.73 \pm 0.38)$ dex for ATLAS9 and MARCS model atmospheres, respectively. The measured iron abundance for the 12

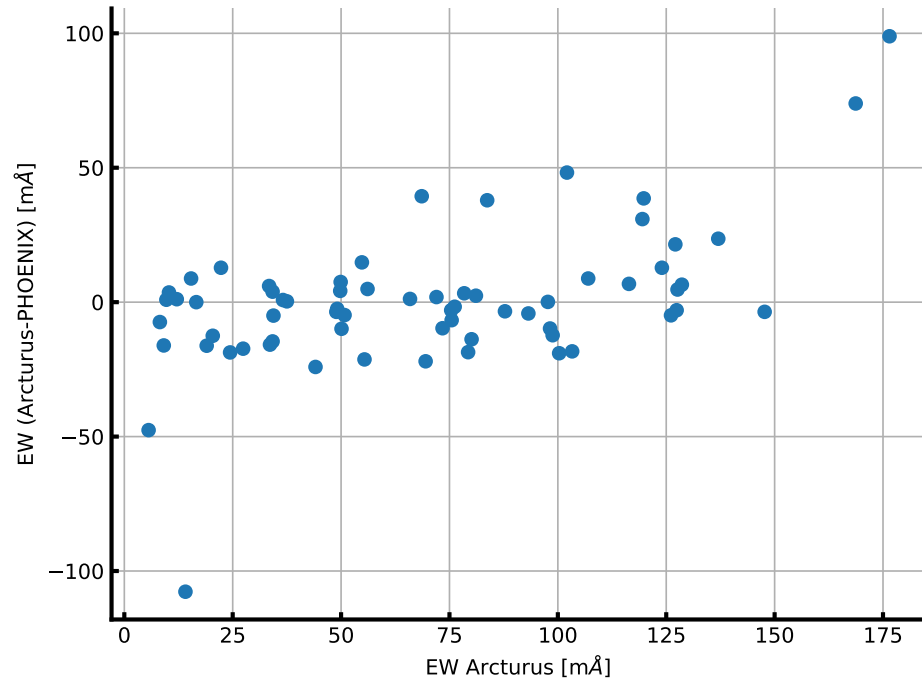


Figure 4.12: Common EWs between Arcturus and the synthetic spectrum with closest parameters (see text for details). The EWs are getting more disperse with increasing EW which is expected when seeing the direct comparison of the spectrum in Figure 4.13.

synthetic spectra can be seen in Figure 4.14. The figure only includes runs which reached convergence with FASMA.

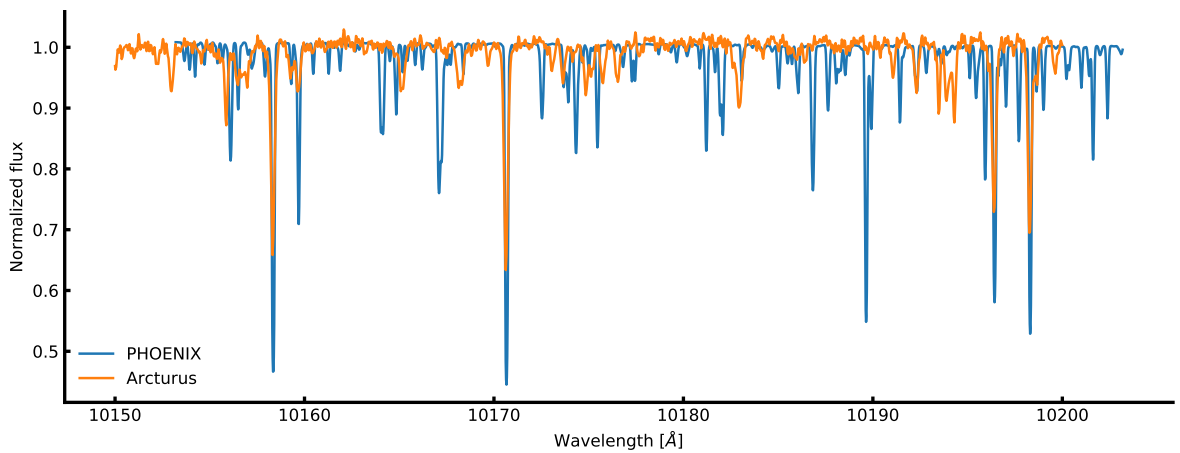


Figure 4.13: Comparison between the Arcturus atlas and a PHOENIX synthetic spectrum with similar parameters to Arcturus (see text for details).

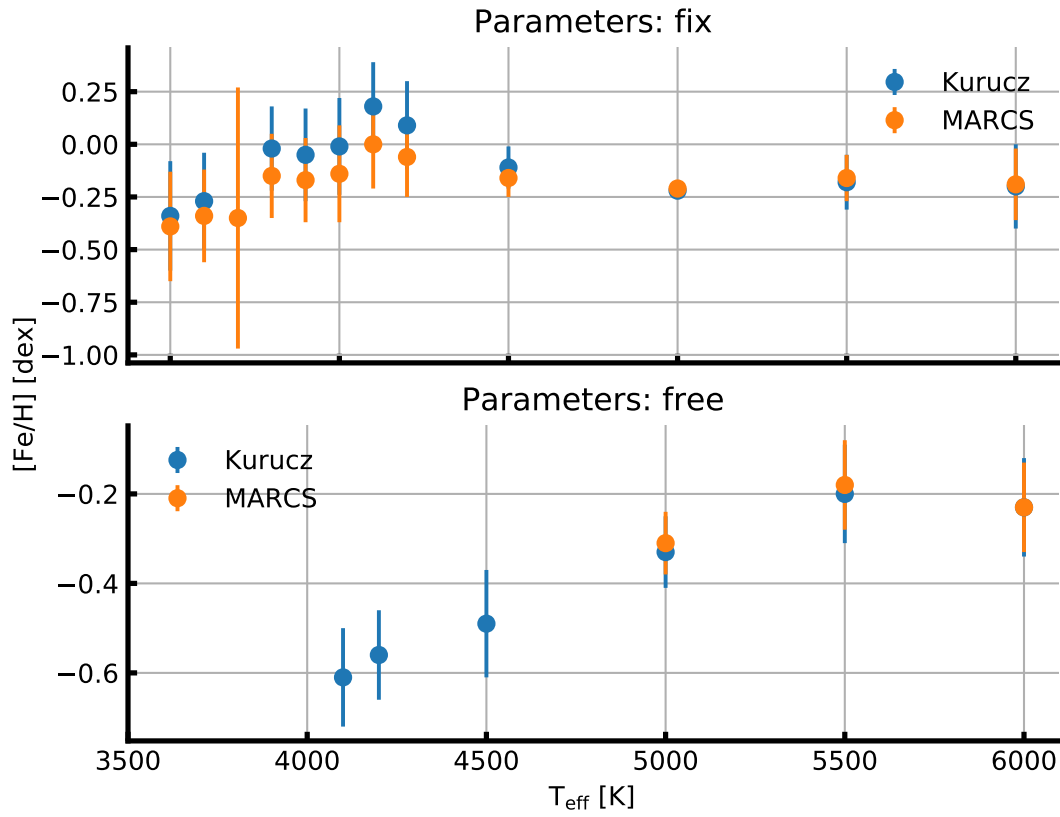


Figure 4.14: Derived $[\text{Fe}/\text{H}]$ with respect to the true T_{eff} for runs that reached convergence. *Top panel:* $\log g$ fixed at 4.5 dex and ξ_{micro} to the empirical relation (see text for details). *Lower panel:* All parameters free.

Chapter 5

SWEET-Cat

If you hold a cat by the tail you learn things
you cannot learn any other way.

Mark Twain

Part of the work during the thesis has been dedicated to regularly update SWEET-Cat¹ after announcements of new exoplanet hosts, a catalogue with all discovered planet hosts, and the stellar parameters. After collecting spectra for more than 50 exoplanet hosts, these were analysed and presented in [Andreasen et al. \(2017b\)](#).

In this chapter a detailed description of SWEET-Cat will be presented along with the analysis of the newly collected spectra.

5.1 What is SWEET-Cat?

As mentioned above, SWEET-Cat is a catalogue of planet host stars. However, the strength of SWEET-Cat is the homogeneously analysed stars utilising the method described in Section 3.2.2 with FASMA or ARES+MOOG.

In the era with a large number of discovered exoplanets (more than 3500 confirmed exoplanet at the moment of writing), it is possible to perform in-depth statistical studies. However, when conducting these studies it is crucial to have consistent measurements of e.g. stellar atmospheric parameters. This can be obtained by using a single analysis to obtain these parameters, as it is known that different methods will lead to different results (see e.g. [Hinkel et al., 2016](#), for a recent review).

To obtain stellar atmospheric parameters in a consistent and homogeneously way is an on-going goal with SWEET-Cat, where high quality spectra are obtained for stars hosting planets. These are used to determine the stellar parameters in a homogeneous way. All stars in SWEET-Cat analysed with the method from our group are marked with a flag. The columns provided in SWEET-Cat are summarised in Table 5.1. It is important to note that SWEET-Cat does not include any planetary parameters.

SWEET-Cat is updated on a weekly basis if new planet hosts are discovered, and whenever planet hosts have been analysed with the method from our group, as described in this thesis.

¹ <https://www.astro.up.pt/resources/sweet-cat/>

Table 5.1: Columns in SWEET-Cat

Column	Unit	Description
Name		Popular stellar name
HD number		HD number
RA	deg	Right ascension
Dec	deg	Declination
Vmag	mag	V magnitude
$\sigma(\text{Vmag})$	mag	Error on V magnitude
π	mas	Parallax
$\sigma(\pi)$	mas	Error on parallax
Source of π		Source of parallax measurement
T_{eff}	K	Effective temperature
$\sigma(T_{\text{eff}})$	K	Error on effective temperature
$\log g$	dex	Surface gravity
$\sigma(\log g)$	dex	Error on surface gravity
$\log g_{\text{LC}}$	dex	Surface gravity corrected from light curves
$\sigma(\log g_{\text{LC}})$	dex	Error on surface gravity corrected from light curves
ξ_{micro}	km/s	Micro turbulence
$\sigma(\xi_{\text{micro}})$	km/s	Error on micro turbulence
[Fe / H]	dex	Metallicity
$\sigma([\text{Fe} / \text{H}])$	dex	Error on metallicity
Mass	M_{\odot}	Stellar mass
$\sigma(\text{Mass})$	M_{\odot}	Error on stellar mass
Reference		Reference for parameters
Homogeneity flag	0/1	0 for not homogeneous analysis, 1 otherwise
Last updated	date	Last updated
Comments		Any special remarks/comments (e.g. M star)

5.2 Data for 50 planet hosts

In this section the data for a large update to SWEET-Cat will be described (Andreasen et al., 2017b). The majority of the data comes as a result from proposals submitted for observational time, while some of the data was found in the archive. In the next section the analysis of the 50 spectra will be presented along with the results.

5.2.1 The data

Data² for 43 out of the 50 stars were collected using UVES/VLT (Dekker et al., 2000), FEROS/2.2m telescope in La Silla (Kaufer et al., 1999), and FIES/NOT (Frandsen and Lindberg, 1999) spectrographs. The remaining spectra were found in various archives³. This includes spectra from the HARPS/3.6m telescope in La Silla (Mayor et al., 2003) and ESPaDOnS/CFHT (Donati, 2003). Some characteristics of the spectrographs are presented in Table 5.2 with the mean S/N for the spectra used. The S/N for each star can be seen in Table B.1 along with the atmospheric parameters of the stars. The S/N is measured automatically by ARES. These 50 stars are confirmed exoplanet hosts listed in SWEET-Cat, but they

² Based on observations collected at the La Silla Observatory, ESO (Chile), with FEROS/2.2m (run 2014B/020), with UVES/VLT at the Cerro Paranal Observatory (runs ID 092.C-0695, 093.C-0219, 094.C-0367, 095.C-0324, and 096.C-0092), and with FIES/NOT at Roque de los Muchachos (Spain) (runs ID 14AF14 and 53-202).

³ ESPaDOnS
HARPS

belonged to the list of stars that have not previously been analysed by our team because no spectra was public available or of high enough quality (high spectral resolution and high S/N).

Table 5.2: Spectrographs used for this paper with their spectral resolution, wavelength coverage, and mean S/N from the spectra used.

Spectrograph	Resolution	Spectral range	Mean S/N
HARPS	115 000	378 nm to 691 nm	642
UVES	110 000	480 nm to 1100 nm	212
ESPaDOnS	81 000	370 nm to 1050 nm	775
FIES	67 000	370 nm to 730 nm	763
FEROS	48 000	350 nm to 920 nm	208

5.2.2 Data collected from archive

The spectra⁴ was obtained with the highest possible resolution for a given spectrograph, and in cases with multiple observations, we include all the observations unless a spectrum is close to the saturation limit for a given spectrograph. All S/N were considered. However, the lower the S/N would in general yield a lower precision on the final parameters. For multiple spectra, we combine them after first correcting the radial velocity (RV) and using a sigma clipper to remove strange peak like features. The individual spectra are then combined to a single spectrum for a given star to increase the S/N. This single spectrum is used in the analysis described below. For most of the spectra in the archive included here, several spectra were combined as described above, while for the observations dedicated to this work, the spectrum would be a single spectrum, or in cases of faint stars, it would be observed a few times to reach the desired S/N. The reason to observe faint stars multiple times rather than in one exposure, is that the total amount of exposure (to reach the desired S/N) is higher than recommended/possible with the instruments used. Moreover, activity on the time scale of the exposure might deform the spectra. This can e.g. be stellar pulsations. The reason for having a single/few spectra of high S/N versus multiple spectra of low S/N is mostly due to the difference in science cases behind the observations; for example, the HARPS spectra were mostly used for RV monitoring or follow-up of the exoplanet(s), while the UVES spectra were mostly used to characterise stellar parameters or other similar projects.

5.3 Analysis of 50 planet hosts

The method of determining atmospheric parameters from the curve of growth analysis has been applied several times in the optical (see e.g. [Sousa et al., 2011](#); [Mortier et al., 2013b](#); [Tsantaki et al., 2013](#); [Santos et al., 2013](#)). When studying stars with planets and any correlations between stellar and planetary parameters it is important to have a homogeneous characterisation of the stars. An effort to compile a sample into a catalogue was initiated by [Santos et al. \(2013\)](#) with the SWEET-Cat database. The motivation to homogenise the stellar hosts is mainly to compare the hosts and make statistical studies on one consistent scale. When doing these statistical studies, the results might otherwise suffer from offsets between different methods.

⁴ Based on observations collected at the La Silla Observatory, ESO (Chile), with HARPS/3.6m (runs 60.A-9036(A), 072.C-0488(E), 081.C-0842(D), 083.C-1001(A), 084.C-0229(A), 087.C-0012(B), 089.C-0732(A), 091.C-0034(A), 092.C-0721(A), 093.C-0409(A), 183.C-0972(A), 188.C-0265(A,D,F,G,H,I,J,K,L,M,N), 192.C-0852(A,M)), and with ESPaDOnS/CFHT at the National Research Council of Canada (runs 14AF14, 07bo03, 11AQ78, 05AC23, 06AF22).

The skills acquired during the thesis on NIR studies as mentioned above were directly translated into deriving parameters for a sample of 50 known planet host stars that were not previously analysed by our group (Andreasen et al., 2017b). The spectra of these stars were required at UVES, FIES, HARPS, and ESPaDOnS with the mean S/N higher than 200.

A Hertzsprung-Russell diagram of the sample can be seen in Figure 5.1. The sample covers a large range of T_{eff} , FGK, while there are both dwarf, sub-giant, and some giant stars. The colours indicate the $\log g$. In order to determine the luminosity of each star the simple relation

$$L = 4\pi R^2 \sigma T_{\text{eff}}^4$$

is used, where L is the luminosity, R is the stellar radius, and σ is the Stefan-Boltzmann constant. In solar units this relation is simply:

$$\frac{L}{L_{\odot}} = \left(\frac{R}{R_{\odot}} \right)^2 \left(\frac{T_{\text{eff}}}{T_{\text{eff},\odot}} \right)^4$$

In order to determine the the stellar radius, the empirical relation from Torres et al. (2010) was used.

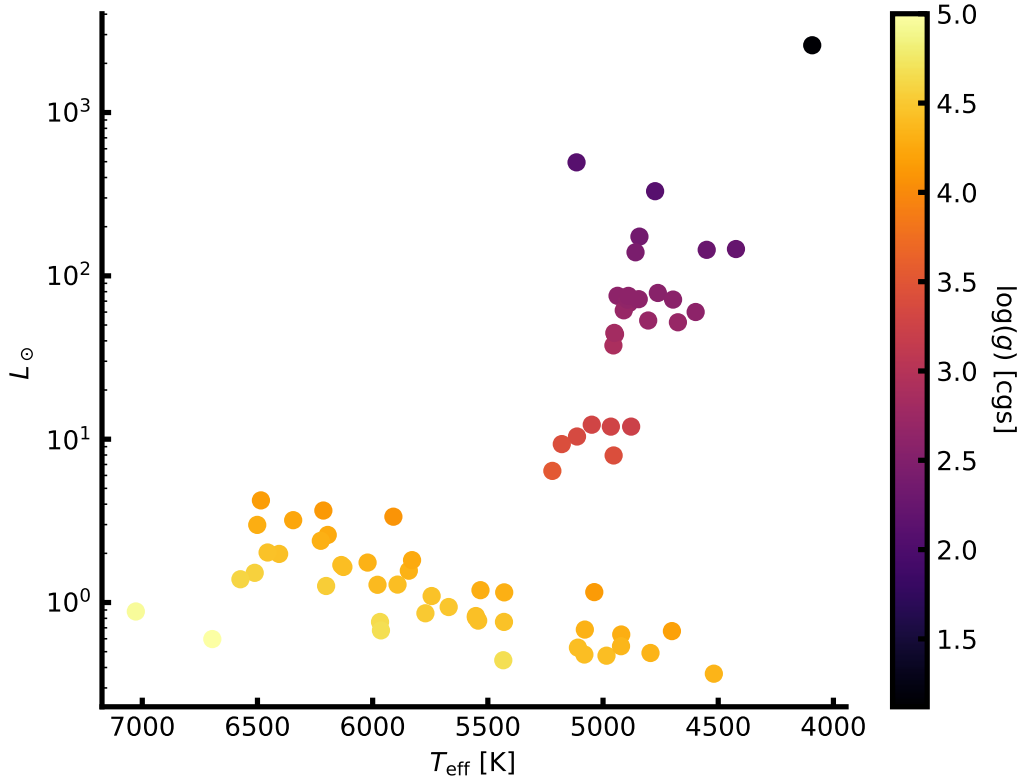


Figure 5.1: A Hertzsprung-Russell diagram of the sample of 50 planet host stars added to SWEET-Cat. The parameters were derived using optical high resolution and high S/N spectra in tandem with FASMA and an optical line list. The colour scale shows the derived $\log g$ for each star.

The parameters were derived using **FASMA** with the optical line list compiled by [Sousa et al. \(2008\)](#) and [Tsantaki et al. \(2013\)](#) for stars where T_{eff} was below 5200 K. All the new derived parameters were added to SWEET-Cat, available for the community. The parameters are also available in Table B.1, while the previous results can be seen in Table B.2. A comparison between the new derived parameters and the previous parameters can be seen in Figure 5.2

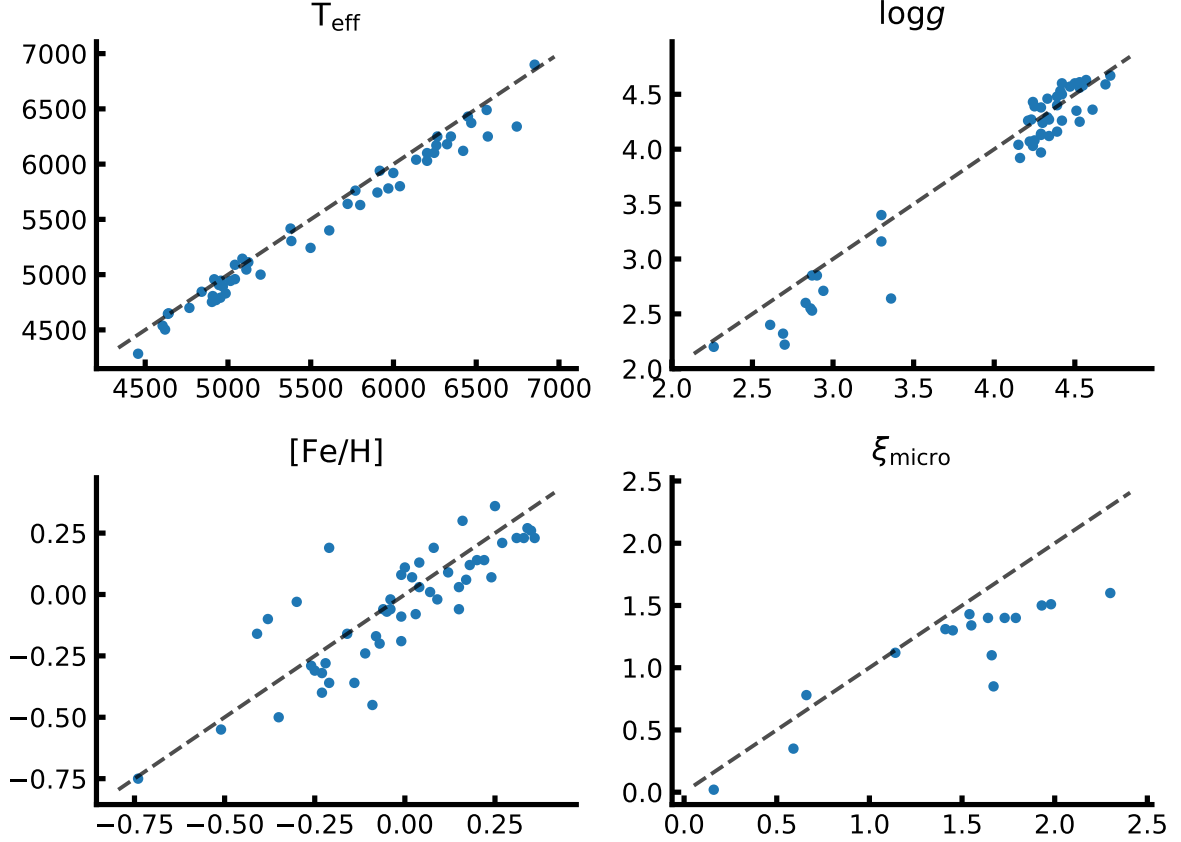


Figure 5.2: The new atmospheric parameters of 50 exoplanet hosts against the previous parameters.

Since there exists more reliable surface gravities than the spectroscopic surface gravity ($\log g_{\text{spec}}$), such as that derived from asteroseismology or transit light curves, a correction to $\log g_{\text{spec}}$ is applied based on asteroseismology as found by [Mortier et al. \(2014\)](#) given by:

$$\log g_{\text{seis}} = \log g_{\text{spec}} - (3.89 \pm 0.23) \times 10^{-4} T_{\text{eff}} + 2.10 \pm 0.14, \quad (5.1)$$

where $\log g_{\text{seis}}$ is the corrected surface gravity. This correction is only used for FGK dwarf stars, i.e. between $4800 \text{ K} \leq T_{\text{eff}} \leq 6500 \text{ K}$ and $\log g \geq 4.2 \text{ dex}$. For stars with a $\log g$ lower than this limit the correction will not be applied, and if the $\log g$ changes to below this limit after the correction, the spectroscopic $\log g$ will be used again. The correction for $\log g$ depends on both T_{eff} and $\log g$. The correction can be up to 0.5 dex, depending on the T_{eff} .

With these updated parameters the completeness of SWEET-Cat for stars brighter than V magnitude 10 is 85% (77% for stars brighter than 12). For fainter stars it is time expensive to acquire spectra of the

quality needed for this method. Moreover, many of the fainter planet host stars have been observed with the *Kepler* space mission, where most stars are faint.

5.3.1 Habitable zone

This section was not part of the original paper (Andreasen et al., 2017b), however it is an interesting showcase of what a catalogue like SWEET-Cat can be used for.

The habitable zone of a star is at the distance where liquid water may exists. This distance depends on T_{eff} and the luminosity, but also on the planetary atmosphere and its composition. Using Equation 3 described in Kopparapu et al. (2013) to calculate the inner and upper limits of the habitable zone. The equation is rather simple:

$$d = \sqrt{\frac{L/L_{\odot}}{S_{\text{eff}}}} \text{ AU}, \quad (5.2)$$

$$S_{\text{eff}} = S_{\text{eff},\odot} + aT_* + bT_*^2 + cT_*^3 + dT_*^4, \quad (5.3)$$

where $T_* = T_{\text{eff}} - 5780 \text{ K}$, and the coefficients can be found in Table 3 in Kopparapu et al. (2013), which depends on the specific model of habitable zone used. Here are used the “Runaway Greenhouse” for the inner limit and “Maximum Greenhouse” for the outer limit of the habitable zone. The equation above is only valid for main sequence stars FGKM, thus only stars with $\log g \geq 4.2$ dex have been included.

It was possible to find three planets within this zone; GJ 785 c, HD 37124 c, and KELT-6 c. These planets does not have known radii, and their minimum masses are $(0.076, 0.652, 3.710)M_{\text{Jupiter}}$, respectively. Thus, it is fair to assume they are all gas planets when comparing to gas planets in our Solar System. All three host stars are metal-poor. A correlation between orbital period and host star metallicity is known (see e.g. Adibekyan et al., 2013), where metal-poor stars have planets with higher orbital period. Since the habitable zone is often quite far from the host star, that is the case for e.g. FGK dwarf stars which can be seen in Figure 5.3, it is expected that metal-poor stars will harbour most of the exoplanets in the habitable zone according to the correlation found in Adibekyan et al. (2013). A quick summary of the system is shown in Table 5.3.

Table 5.3: Host star and planetary properties of GJ 785, HD 37124, and KELT-6; all which have an exoplanet in the habitable zone.

Parameter	GJ 785	HD 37124	KELT-6
Stellar parameters			
T_{eff}	$(5087 \pm 48) \text{ K}$	$(5460 \pm 35) \text{ K}$	$(6246 \pm 88) \text{ K}$
$\log g$	$(4.30 \pm 0.10) \text{ dex}$	$(4.26 \pm 0.04) \text{ dex}$	$(4.22 \pm 0.09) \text{ dex}$
$[\text{Fe}/\text{H}]$	$(-0.01 \pm 0.03) \text{ dex}$	$(-0.42 \pm 0.03) \text{ dex}$	$(-0.22 \pm 0.06) \text{ dex}$
Luminosity	$0.72L_{\odot}$	$1.10L_{\odot}$	$2.70L_{\odot}$
V magnitude	6.13	7.68	10.38
Planetary parameters			
Planet	GJ 785 c	HD 37124 c	KELT-6 c
Period	525 days	885 days	1276 days
Mass	$0.076M_J$	$0.652M_J$	$3.710M_J$
Semi-major axis	1.18 AU	1.71 AU	2.39 AU
Inner HZ limit	0.86 AU	1.04 AU	1.56 AU
Outer HZ limit	1.53 AU	1.84 AU	2.70 AU

In Figure 5.3 the habitable zone of the stars analysed here are shown along with the location of the planets. The three systems mentioned above are highlighted in the figure.

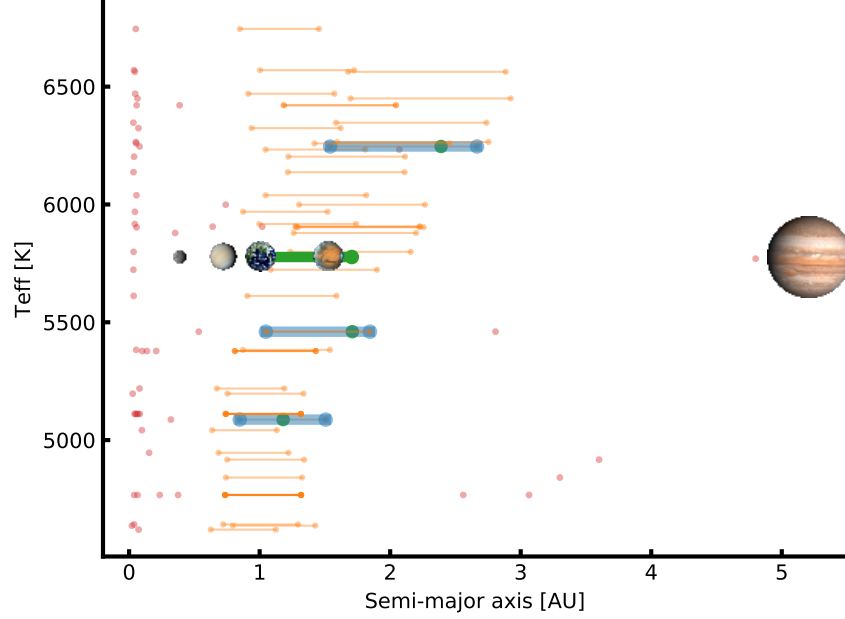


Figure 5.3: The habitable zone for the updated SWEET-Cat stars. The coloured line shows the theoretical habitable zone, while the dots shows the location of the planets in the actual system. The blue lines show the habitable zone of the three stars where a planet is located within it (green points). The red dots and orange lines are systems which does not lie within the habitable zone. Finally, the green line shows the location of the Sun’s habitable zone and the first five planets placement. In this model both Earth and Mars are within the habitable zone.

5.3.2 Changes to planetary parameters

As a results to the analysis above, it is expected that some planetary parameters will change compared with the previous literature values due to the connection between derived planetary parameters and stellar parameters (see Equation 1.1 and Equation 1.2).

Therefore the radius and mass of all the 50 new stars updated in SWEET-Cat were computed using the empirical formula presented in [Torres et al. \(2010\)](#). Some of the stars have radii derived from different methods, usually from isochrones. These radii generally show a good correlation with radii derived from [Torres et al. \(2010\)](#) if the literature parameters of T_{eff} , $\log g$, and $[\text{Fe}/\text{H}]$ are used. However, when comparing with the new radius derived using the parameters presented here, the results can differ by up to 65%. This is shown in Figure 5.4 how the radius calculated from [Torres et al. \(2010\)](#) differs between the literature atmospheric parameters and the new homogeneous atmospheric parameters presented here. Note that stellar radii are provided by many of the authors from different discovery papers, but here the atmospheric parameters via the derivation of the stellar radius, as described above, are compared, rather than comparing the stellar radii from different methods.

In the sections below there follow a discussion of the systems (seven stars, eight exoplanets) where

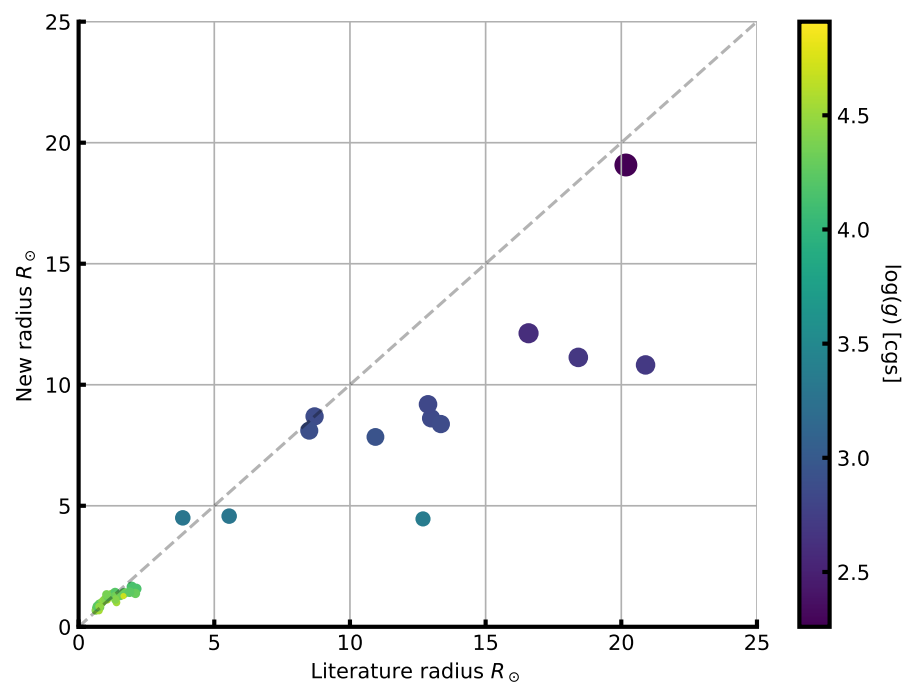


Figure 5.4: Stellar radius on both axes calculated based on [Torres et al. \(2010\)](#). The x-axis shows the stellar radius based on the atmospheric parameters from the literature, while the y-axis indicates the new homogeneous parameters presented here. The colour and size indicate the surface gravity. This clearly shows that the disagreement is biggest for more evolved stars.

the radius or mass of the stars changes more than 25% and how this influences the planetary parameters. The changes in radius for a star is primarily due to changes in $\log g$, which can be used as an indicator of the evolutionary stage of a star. Discrepancies in $\log g$ are also typically the reason for derived mass differences.

The planetary radius, mass, and semi-major axis were re-derived when possible following the three simple scaling relations based on Newton’s law of gravity (Newton, 1687) for deriving mass and distance and simple geometry for radius (see e.g. Torres et al., 2008)

$$M_{\text{pl,new}} = \left(\frac{M_{*,\text{lit}}}{M_{*,\text{new}}} \right)^{-2/3} M_{\text{pl,lit}} \quad (5.4)$$

$$R_{\text{pl,new}} = \left(\frac{R_{*,\text{lit}}}{R_{*,\text{new}}} \right) R_{\text{pl,lit}} \quad (5.5)$$

$$a_{\text{pl,new}} = \left(\frac{M_{*,\text{lit}}}{M_{*,\text{new}}} \right)^{1/3} a_{\text{pl,lit}}, \quad (5.6)$$

where the subscript “lit” denotes the value from the literature used in the comparison, the subscript “new” indicates the new computed values, the subscript “pl” is short for planet, and the subscript “*” is short for star; M , R , and a are mass, radius, and semi-major axis, respectively. Note that for the literature values, the values reported directly from the literature were used and not the derived radius and mass from Torres et al. (2010). To identify outliers, the radii and masses were compared when derived from Torres et al. (2010) since this is a measure of how the atmospheric parameters have changed.

5.3.2.1 HAT-P-46

HAT-P-46 has two known exoplanets according to Hartman et al. (2014a). The outer planet HAT-P-46 c is not transiting, hence the radius is not known for this planet. The results presented above for this star come from UVES/VLT data with a S/N of 208. Hartman et al. (2014a) derived the following spectroscopic parameters: $T_{\text{eff}} = (6120 \pm 100)$ K, $\log g = (4.25 \pm 0.11)$ dex, and $[\text{Fe}/\text{H}] = (0.30 \pm 0.10)$ dex. Note that for this star the asteroseismic correction applied (see Section 5.3) results in a corrected $\log g$ below 4.2dex, so the spectroscopic $\log g$ was used for this star.

If mass and radius is derived of HAT-P-46 b with the new parameters, the radius obtained is $R_{\text{pl}} = 0.93R_J$, while Hartman et al. (2014a) derived $R_{\text{pl}} = 1.28R_J$. No change in mass is seen (Hartman et al. 2014a found $M_{\text{pl}} = 0.49M_J$); however, there is a decrease in the radius, and this results with a more dense planet, $\rho_{\text{pl}} = 0.76 \text{ g/cm}^3$ from $\rho_{\text{pl}} = (0.28 \pm 0.10) \text{ g/cm}^3$.

Only the minimum mass is known for the secondary companions, as it does not transit HAT-P-46 seen from Earth. With the derived parameters here, the minimum mass is $M \sin i_{\text{pl}} = 1.97M_J$, where Hartman et al. (2014a) presented $M \sin i_{\text{pl}} = 2.00M_J$, so a very small change, as expected.

5.3.2.2 HD 120084

The exoplanet orbiting this star with a period of 2082 days and a quite eccentric orbit at 0.66 was discovered by Sato et al. (2013a). The atmospheric parameters were derived by Takeda et al. (2008) using a similar method to that described here. The quality of the spectra they analysed, however, were not as high as those used here. Using the HIDES spectrograph at the 188 cm reflector at NAOJ, Takeda et al. (2008) reported an average S/N for their sample of 100-300 objects at a resolving power of 67 000.

The spectrum used here is from ESPaDOnS with a resolving power of 81 000, and with a S/N for this star at 850. With the new parameters obtained, there is a slight decrease in stellar mass for the star at $1.93M_{\odot}$ compared to $2.39M_{\odot}$ obtained by [Takeda et al. \(2008\)](#), hence the minimum planetary mass is also slightly lower, from $m_{\text{pl}} \sin i = 4.5M_J$ to $m_{\text{pl}} \sin i = 3.9M_J$. The stellar radius decrease by 28%, from $9.12R_{\odot}$ to $7.81R_{\odot}$. Since there are no observations of the planet transiting, the planetary radius has not been computed.

5.3.2.3 HD 233604

HD 233604 b was discovered by [Nowak et al. \(2013\)](#), while the stellar atmospheric parameters of the star were derived by [Zieliński et al. \(2012\)](#), who used the same method as described here using the HRS spectrograph at HET with a resolving power of 60 000 with a typical S/N at 200-250. For the analysis presented here, a spectrum from the FIES spectrograph was used with a slightly higher resolution at 67 000, and similar but also slightly higher S/N at 320 for this star.

This planet is in a very close orbit with a semi-major axis of $\sim 15R_*$ (R_* is the stellar radius) using the parameters from [Nowak et al. \(2013\)](#). Using the updated parameters presented in this paper the stellar mass increase slightly from $1.5M_{\odot}$ to $1.9M_{\odot}$, and a decrease in stellar radius from $10.5R_{\odot}$ to $8.6R_{\odot}$. This increases the semi-major axis to $\sim 21R_*$. We note that the correct stellar radii are used to describe the semi-major axis in both cases. The increase in stellar mass leads to an increase in the minimum planetary mass, from $m_{\text{pl}} \sin i = 6.58M_J$ to $m_{\text{pl}} \sin i = 7.79M_J$.

Moreover, [Nowak et al. \(2013\)](#) found a high Li abundance at $A(\text{Li})_{\text{LTE}} = (1.400 \pm 0.042)$ dex for this star and speculated that this star might have engulfed a planet. A more likely explanation is that this star has not yet reached the first dredge-up process ([Nowak et al., 2013](#)). In the analysis here a much lower value is found, $A(\text{Li})_{\text{LTE}} = 0.92$ dex, and hence the star is not believed to be Li rich. The Li abundance found here is in excellent agreement with [Adamów et al. \(2014\)](#). Even applying a NLTE correction, as was done in [Adamów et al. \(2014\)](#) ($A(\text{Li})_{\text{NLTE}} = 1.08$), this star is not Li rich.

5.3.2.4 HD 5583

This exoplanet was discovered by [Niedzielski et al. \(2016\)](#) with an orbital period of 139 days around a K giant. This exoplanet was discovered with the radial velocity technique, and the planetary radius is not known. The stellar parameters were derived in a similar manner to that presented here (see [Niedzielski et al., 2016](#), and references therein); the biggest disagreement is in the surface gravity. Here was derived a $\log g$ that is higher by 0.34 dex, which gives a stellar radius that is smaller by 37%. The derived mass is 15% higher, which in turn increases the minimum planetary mass from $m_{\text{pl}} \sin i = 5.78M_J$ to $m_{\text{pl}} \sin i = 8.63M_J$. Even with the increase in mass, it is still within the planetary regime for most inclinations, as was noted by [Niedzielski et al. \(2016\)](#).

5.3.2.5 HD 81688

This exoplanet was discovered by [Sato et al. \(2008\)](#) with the RV method. The host star is a metal-poor K giant. The atmospheric parameters presented in [Sato et al. \(2008\)](#) are obtained via the same method as presented here, and the agreement is quite good. Once again the big disagreement is in the surface gravity: Here was obtained 0.48 dex higher. Even though the stellar atmospheric parameters, and hence the planetary parameters, do change, the radius and mass derived are not far from the values presented

in the paper by [Sato et al. \(2008\)](#). This is a case where the star was marked as an outlier, due to the comparison between the radius and mass derived from [Torres et al. \(2010\)](#).

The new stellar mass is the same as before, $2.1M_{\odot}$. The stellar radius changed from $13.0R_{\odot}$ to $10.8R_{\odot}$. Since a transit of this star has not been observed and the stellar mass remains the same, there is no change in the planetary parameters.

It is worth noting that this system is in an interesting configuration with a very close orbit around an evolved star. This system, among others, has been the subject of work on planet engulfment (see e.g. [Kunitomo et al., 2011](#)).

5.3.2.6 HIP 107773

The planetary companion was presented in [Jones et al. \(2015\)](#) as an exoplanet around an intermediate-mass evolved star. The stellar parameters were obtained from the analysis by [Jones et al. \(2011\)](#) using the same method as presented here, but with a different line list, which might lead to some disagreements. A higher $\log g$ (2.83 dex compared to 2.60 dex) was derived here, thus the star is slightly smaller with $11.6R_{\odot}$ to $9.2R_{\odot}$ and $2.4M_{\odot}$ to $2.1M_{\odot}$ for radius and mass of the star, respectively. The other atmospheric parameters are very similar to those derived by [Jones et al. \(2011\)](#). This leads to a reduced minimum mass of the planetary companion from $m \sin i = 1.98M_J$ to $m \sin i = 1.78M_J$. The planetary radius has not been measured.

5.3.2.7 WASP-97

The exoplanet orbiting WASP-97 was discovered by [Hellier et al. \(2014\)](#). The host star parameters were derived using a similar method to that described here after co-adding several spectra from the CORALIE spectrograph. They reach a S/N of 100 with a spectral resolution of 50 000. The parameters presented here come from the UVES spectrograph with a S/N of more than 200.

The parameters do not change much for this planet. The minimum planetary mass changes from $m_{\text{pl}} \sin i = 1.32M_J$ to $m_{\text{pl}} \sin i = 1.37M_J$ and the radius from $1.13R_J$ to $1.42R_J$. This affects the density quite strongly; it changes from 1.13 g/cm^3 to 0.59 g/cm^3 . This exoplanet is then in the same category as Saturn; its density is lower than water, but it is slightly larger than Jupiter.

5.3.2.8 ω Serpentis (ome Ser)

The exoplanet orbiting this star with a period of 277 days and an eccentric orbit at 0.11 was also presented by [Sato et al. \(2013a\)](#). The atmospheric parameters were derived in the same way as for HD 120084. Data from FIES with a resolving power of 67 000 was used, and with a S/N for this star of 1168. With the new parameters a slightly higher stellar mass for the star is obtained at $2.19M_{\odot}$ compared to the value of $2.17M_{\odot}$ obtained by [Takeda et al. \(2008\)](#). This change is not significant enough to change the minimum planetary mass at $m_{\text{pl}} \sin i = 1.7M_J$. The stellar radius decreases by more than one solar radius, from $12.3R_{\odot}$ to $11.1R_{\odot}$. However, since there are no observations of transiting exoplanets, any change in planetary radius cannot be detected.

5.3.2.9 α Ursa Major (omi UMa)

omi UMa b was discovered by [Sato et al. \(2012\)](#) using the RV method. The stellar parameters are from [Takeda et al. \(2008\)](#), as discussed above. The spectrum used for this star is from ESPaDOnS with a S/N

of more than 500 compared to the value of 100-300 reached for the large sample presented in [Takeda et al. \(2008\)](#). The luminosity and mass for omi UMa were obtained from theoretical evolutionary tracks (see [Sato et al., 2012](#), and references therein). The radius was then estimated using the Stefan-Boltzmann relationship, using the measured luminosity and T_{eff} .

The parameters presented here mainly differ in the surface gravity: here it is 0.72 dex higher at $\log g = 3.36$. This leads to a big change in stellar mass and radius from $3.1M_{\odot}$ to $1.6M_{\odot}$ and $14.1R_{\odot}$ to $4.5R_{\odot}$, respectively. [Sato et al. \(2012\)](#) have reported that omi UMa b is the first planet candidate around a star more massive than $3M_{\odot}$, which is not supported by the results presented here. With these updated results, the minimum mass of the planet is now $m \sin i = 2.7M_J$, whereas previously it was $m \sin i = 4.1M_J$ ([Sato et al., 2012](#)). The exoplanet is not reported to transit, as seen from Earth, so the radius for this exoplanet is not known, which would have changed a great deal with these new results.

5.4 Discovering two giant planet populations

The stellar parameters from SWEET-Cat was combined with the exoplanetary database from [Exoplanet.eu](#) to explore new star-planet connections by [Santos et al. \(2017\)](#). With the amount of exoplanets discovered, it opens up the possibility for statistical studies, which might give insight in the models describing planet formation and evolution (see e.g. [Mayor et al., 2014](#)).

In this work by [Santos et al. \(2017\)](#), the study was focused on giant exoplanets, namely exoplanets with masses higher than $1M_{\text{Jup}}$ and below $25M_{\text{Jup}}$. The upper limit is to avoid entering the brown dwarf regime. In cases where the exoplanet have only been detected by RV, the minimum mass is used. There were some additionally constraints:

- All stars have T_{eff} , $\log g$, and $[\text{Fe}/\text{H}]$ listed in SWEET-Cat.
- T_{eff} between 4000 K and 6500 K for more reliable derived stellar atmospheric parameters with high quality spectra.
- Visual magnitude below 13 (not very constraining) for more reliable RV measurements and confidence that the stellar atmospheric parameters can be derived reliably.
- Cut in orbital period to only consider exoplanets between 10 days and 5 years. Lower limit is to avoid hot Jupiters for which the formation mechanism is still debated (see e.g. [Ngo et al., 2016](#); [Nelson et al., 2017](#)). The upper limit is for completeness, assuring that the planet would not be missed in RV surveys.

A histogram of the exoplanetary masses (in the $1 - 20M_{\text{Jup}}$ mass range) is shown in Figure 5.5. Both with and without the constraint. Two different peaks become evident in this plot around $4M_{\text{Jup}}$.

The sample was divided at the highest mass exoplanets ($4 - 15M_{\text{Jup}}$) and the lowest mass giant exoplanets ($1 - 4M_{\text{Jup}}$), and the stellar parameters were explored in these two sub-samples. Specifically the $[\text{Fe}/\text{H}]$ was explored here. This can be seen in Figure 5.6, where the samples have been divided into stellar mass groups as well (including the full sample). Kolmogorov-Smirnov (K-S) tests were performed on each case, in order to understand if the sub-samples comes from the same parent population.

From the K-S p -values, it suggest that the two sub-samples (high and low exoplanet masses) comes from distinct population when considering all the stars ($p = 5 \cdot 10^{-4}$) and the highest mass stars (above $1.5M_{\odot}$; $p = 3 \cdot 10^{-3}$), while the p -value increasing for the intermediate stellar masses ($1 - 1.5M_{\odot}$;

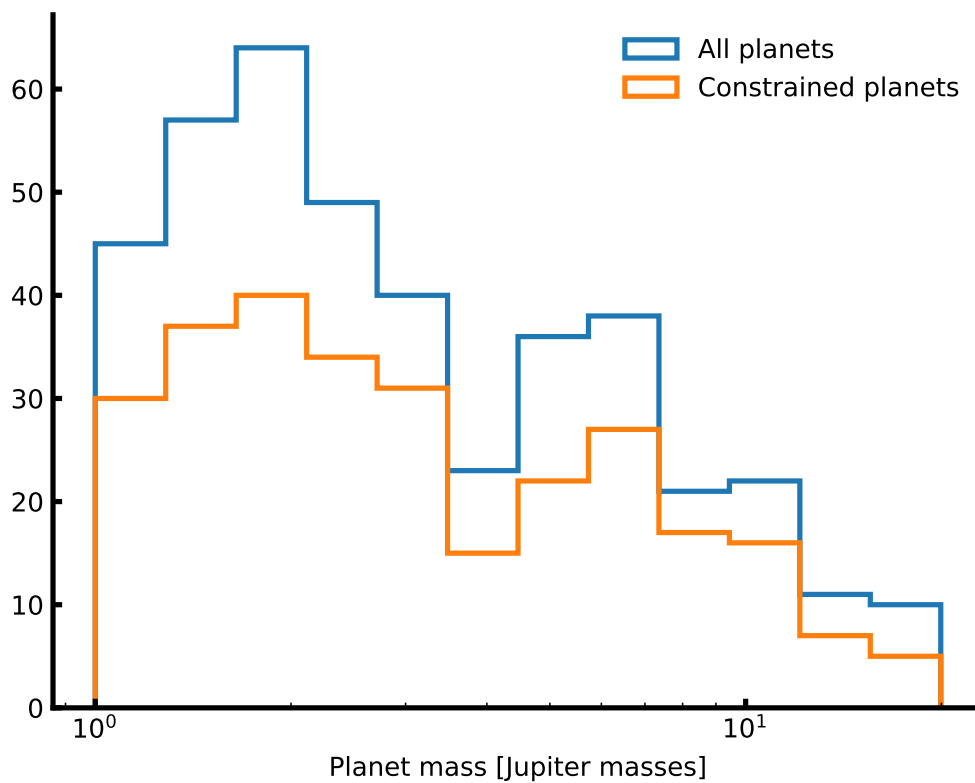


Figure 5.5: Giant planet masses for the full sample and constrained sample (see text for details). This study was performed by [Santos et al. \(2017\)](#) to distinct two giant planet populations.

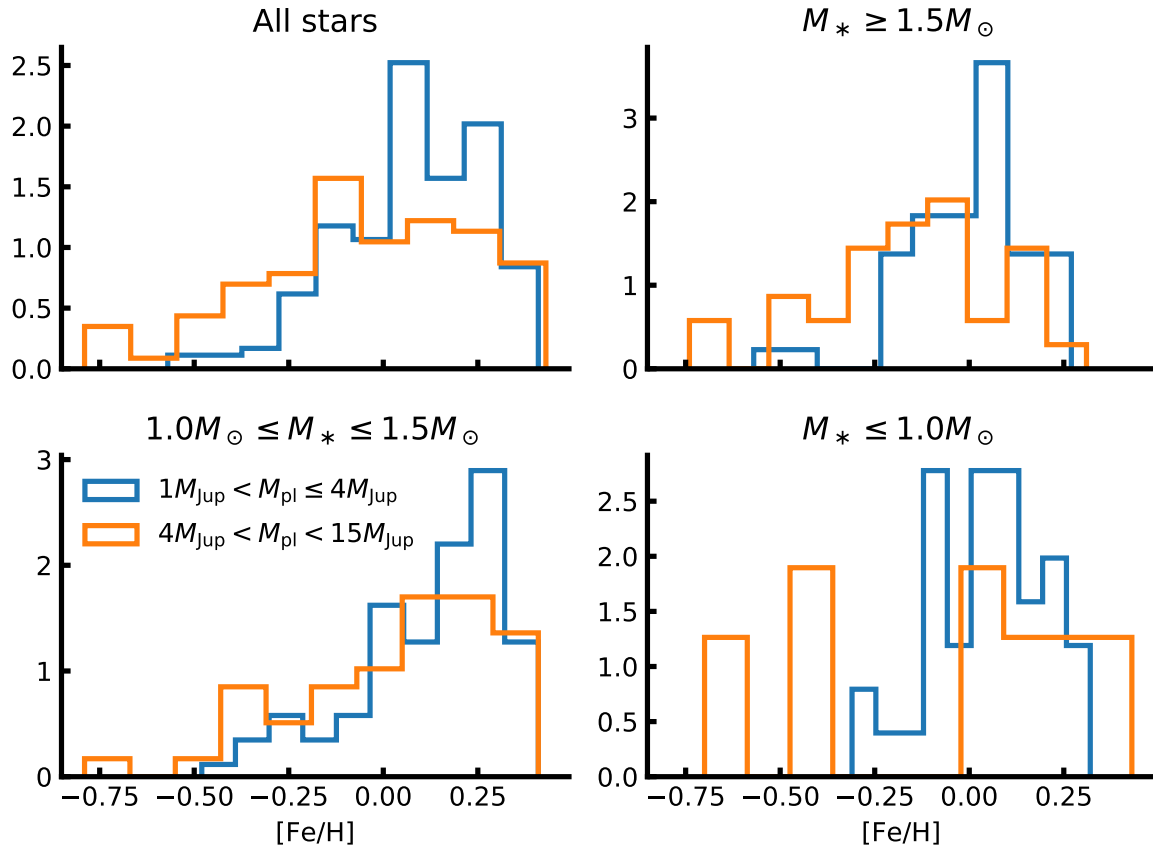


Figure 5.6: [Fe/H] distributions for the lowest and highest exoplanet masses. These are divided into different stellar mass ranges.

$p = 0.06$), and the lowest stellar masses ($1M_{\odot}$; $p = 0.06$). No statistical evidence were found that the two sub-samples were significantly different, when considering orbital period or eccentricities instead of stellar metallicity.

The results suggest that there are evidence for two different giant planet populations. Stars with planets more massive than $4M_{\text{Jup}}$ are in average more metal-poor; a trend that is statistically significant for more massive stars (above $1.5M_{\odot}$), although it is observed in all stellar mass regimes. As was discussed briefly in Section 1.2.1, there is a strong correlation between stellar metallicity and planet frequency; stars hosting giant planets are more metal-rich than stars without planets. An observational fact that supports the core-accretion model for planet formation. Thus it is intriguing that here the most massive planets are found around the more metal-poor stars. In the core-accretion paradigm it has been suggested that the planet frequency increase with stellar mass up to $3M_{\odot}$ (Kennedy and Kenyon, 2008). Additionally, it is known that higher mass stars have higher mass disks (Natta et al., 2000). Therefore, the results presented here might simply show that the most massive exoplanets ($> 4M_{\text{Jup}}$) are formed around the most massive stars, even though these stars might be more metal-poor (compared to the stars hosting low mass giant exoplanets), because the most massive stars can have more massive disks.

To explore this explanation, the $M_{*}10^{[\text{Fe}/\text{H}]}$ index was compared for the two planet population. This index is expected to measure the total amount of the heavy material in the disks, and is thus a better measure for the planet formation efficiency in the core-accretion scenario. For all the stars in the sample, the K-S test gives a p -value of 0.08. So the stellar mass can only be part of the explanation.

Alternatively it has been suggested that gravitational instability may be less dependent on metal content as core-accretion to form planets (Boss, 2002; Cai et al., 2006).

Then the observational results can be interpreted as showing two distinct giant planet populations formed by different physical processes:

- Low mass giant planets ($1 - 4M_{\text{Jup}}$): Formed by core-accretion around more metal-rich stars.
- High mass giant planets ($> 4M_{\text{Jup}}$): Formed by gravitational instability (or other instability process), less sensitive to stellar metallicity.

5.5 Updating SWEET-Cat

While SWEET-Cat is already a success, it is important to strive to improve the catalogue. Therefore several improvements for SWEET-Cat are planned. The most important additions are the derivation of chemical abundances and derivation of mass⁵, radius, and age using stellar modelling.

With the derivation of chemical abundances, it is possible to make more in-depth studies of the planet hosts, e.g. by studying trends with condensation temperatures (see e.g. Adibekyan et al., 2016). By deriving the masses and radii of the planet hosting stars, the planetary parameters, (mass and radius, and thus the bulk density) can be derived in a consistent way. This leads to a third improvement of SWEET-Cat; namely re-derived planetary parameters using the homogeneously derived stellar parameters.

When deriving the stellar masses and radii, the luminosity is also an output, which could be added to the future version of SWEET-Cat. This leads to simple estimates of the habitable zone limits (see the discussion above in Section 5.3.1). The implication of this is immediately evident: locating exoplanets in

⁵ The mass is currently available, however it is derived from an empirical relation.

the habitable zone with the updated stellar parameters. This is of course particularly interesting if the exoplanet is rocky.

Two other additions to SWEET-Cat could be the projected rotational velocity, $v \sin i$, and activity indicators such as $\log R'_{\text{HK}}$. Note that $v \sin i$ will be difficult to derive. Here it is simplest to use synthesis to estimate this parameter, although for slow rotating stars (below 10 km/s) it is difficult to measure accurately with a high precision. These slow rotating stars are the ones used with the method described above in e.g. Section 5.3. The activity is very important to include, since relations with stellar age and stellar rotation might be explored. Moreover, some non-obvious correlations such as the correlation found between $\log R'_{\text{HK}}$ and planetary surface gravity (Hartman, 2010; Figueira et al., 2014b) might be explored as well.

The last update on the wish-list is for the web page itself. It could be made modern with plotting capabilities, and in tandem combine SWEET-Cat with an exoplanet database, such as [Exoplanet.eu](https://exoplanet.eu). This will allow any user to quickly explore relations between stellar and planetary properties. The tool for plotting has already been developed and is distributed along with other scripts developed during this PhD under `astro_scripts`⁶.

⁶ Can be found here: https://github.com/DanielAndreasen/astro_scripts, and can be installed with `pip install astro-scripts`

Conclusions and future work

Don't cry because it's over, smile because it happened.

Dr. Seuss

6.1 Conclusions

This thesis consisted of two separated analysis. 1) The analysis of NIR stellar spectra and the compilation of a new iron line list for determining stellar atmospheric parameters, and 2) the analysis of 50 planet-hosting stars and update of SWEET-Cat. These two different analyses (NIR and optical) were both done using the same method; determination of stellar atmospheric parameters using high quality spectra by imposing ionization and excitation equilibrium. In a few summarised points, this thesis brings:

- A new NIR line list consisting of 84 Fe I lines and 5 Fe II lines. This line list is optimised for usage with high quality spectra. The goal is to analyse FGK stars and making the bridge towards the M stars. Especially are the dwarf stars of most interest, in the context of exoplanets and the search of habitable worlds. “Know the star, know the exoplanet” is the key.

The line list has been tested on few NIR spectra, mostly due to the lack of spectra and the difficulties it is to currently obtain any NIR spectra. This is about to change in the near future. The tests performed have been increasingly successful, and progress is evident.

- To analyse the data a new tool was created, **FASMA**. This tool provides many different options, can be used with different atmosphere models, is available to the community as a web application, and provides three different drivers for analysis of spectra: EW measurements, deriving parameters, and deriving abundances of a range of elements. A fourth driver is under construction which is to derive parameters using the synthesis method ([Tsantaki et al., 2017](#)).
- The analysis of 50 planet-host stars to increase the number of homogeneously analysed stars was also the first appearance and official usage of **FASMA**. This analysis increased the completeness to 85% for stars brighter than 10 V magnitude. It is time consuming to obtain high quality spectra for stars fainter than this magnitude, however the completeness is still at 77% for stars brighter than 12 V magnitude. Out of the 50 planet host stars analysed, eight changed either the radius or

mass by more than 25%. These eight systems were carefully analysed, and the updated planetary parameters (radius, mass, and density) were derived when possible.

6.2 Future work

While the tests with the NIR line list has been successful, there will still be room for improvements. The same is the case for the FASMA and SWEET-Cat. Here are some of the main points for (possible) future work.

- One of the most difficult parameters to derive from high quality NIR spectra is the surface gravity. This has also been known for the optical part of the spectrum (see e.g. [Mortier et al., 2014](#)). However, with the iron line list presented here, the problem is more severe than the optical. This is mainly due to the lack of Fe II lines. There might be different ways to solve this problem.
 1. Set the $\log g$ to a fixed value determined from other sources (this can e.g. be asteroseismology).
 2. Obtain more Fe II lines in the NIR. With the increased experience, it might prove valuable to have a second look at the Fe II lines, thereby increase the numbers.
 3. Explorer another element than iron. While iron is both abundant in numbers and have a lot of transitions, there might exists a better element for this.
 4. Find other pressure sensitive features in the NIR to derive $\log g$. In this case it will then be combined with the first point raised, and iteratively obtaining T_{eff} , $[\text{Fe}/\text{H}]$, and ξ_{micro} , before then obtaining $\log g$.

This points requires some consideration before anything is done, as they might be time consuming or not work as intended. As an example, it might not always be a advisable to set the surface gravity (or any other parameters) to a fixed value.

- The model atmosphere used is reliable, however newer versions are available. It would be interesting to use more recent versions of the ATLAS9 atmosphere models, and to explorer other atmosphere models altogether, as the PHOENIX library.
- While FASMA is in a state where it work well and is stable, there are still ways to improve it. One way is to use machine learning to get a better guess of initial parameters. This work has already been initiated, and details on this can be seen in Chapter C, however the work is not yet connected to FASMA. An additional plugin to FASMA could be to correct line abundances for non-LTE effects using a pre-calculated grid of these corrections. The main part of this has already been done in another project, but is not yet implemented into FASMA.
- After obtaining stellar atmospheric parameters from a high quality spectrum it is natural to explorer the spectrum with another purpose: to obtain abundances for other elements. The individual abundances of other elements than iron might be used to explorer the history of the star, and can be used in connection with the plant-star correlations. This is something that is already explored in detail in the optical, but is yet a relative new approach in the NIR from high quality spectra.
- One of the main limitations during this thesis have been the limited access to data. This lead to the analysis of synthetic spectra. It will be very interesting to explorer real data in the future. Particular

interesting is the CARMENES library which is under constructions. This library will contain a high S/N spectrum of all the stars observed by CARMENES. This can be used to accurately explorer different part of the parameter space and find weak points in the methodology presented here in this thesis.

- This was already discussed previously, however, it will be interesting to update SWEET-Cat. These updates can include more columns such as abundances of the planet host, modelled mass, radius, and age, rotational velocity, etc. The update to SWEET-Cat can also be for the web interface. A wish is to update this and include easy-plotting capabilities for users to quickly explorer planet-star correlations.

Appendix A

NIR line list

Table A.1: The NIR iron line list. The $\log g$ are calibrated with FASMA using the ATLAS9 model atmospheres by Kurucz (1993).

Wavelength Å	Atomic number	Excitation potential eV	$\log gf$	Element	Solar EW mÅ
10065.05	26.0	4.83	-0.279	Fe I	94.0
10080.42	26.0	5.10	-1.964	Fe I	5.9
10081.39	26.0	2.42	-4.512	Fe I	6.9
10086.24	26.0	2.95	-3.978	Fe I	7.0
10137.10	26.0	5.09	-1.736	Fe I	9.8
10142.84	26.0	5.06	-1.554	Fe I	14.9
10145.56	26.0	4.80	-0.118	Fe I	109.0
10155.16	26.0	2.18	-4.336	Fe I	16.2
10156.51	26.0	4.59	-2.109	Fe I	12.2
10167.47	26.0	2.20	-2.319	Fe I	125.7
10195.11	26.0	2.73	-3.608	Fe I	22.6
10216.31	26.0	4.73	0.047	Fe I	129.9
10218.41	26.0	3.07	-2.893	Fe I	40.9
10265.22	26.0	2.22	-4.648	Fe I	8.1
10307.45	26.0	4.59	-2.432	Fe I	6.4
10332.33	26.0	3.63	-3.131	Fe I	10.5
10340.89	26.0	2.20	-3.665	Fe I	46.6
10347.97	26.0	5.39	-0.717	Fe I	37.0
10353.81	26.0	5.39	-0.989	Fe I	24.2
10364.06	26.0	5.45	-1.100	Fe I	18.0
10379.00	26.0	2.22	-4.236	Fe I	18.7
10388.75	26.0	5.45	-1.471	Fe I	8.7
10395.80	26.0	2.18	-3.435	Fe I	61.3
10423.03	26.0	2.69	-3.658	Fe I	22.9
10423.74	26.0	3.07	-3.119	Fe I	29.9

Table A.1: continued.

Wavelength Å	Atomic number	Excitation potential eV	log <i>gf</i>	Element	Solar EW mÅ
10469.65	26.0	3.88	-1.277	Fe I	89.3
10532.24	26.0	3.93	-1.650	Fe I	64.4
10555.65	26.0	5.45	-1.282	Fe I	13.1
10577.14	26.0	3.30	-3.222	Fe I	17.2
10616.72	26.0	3.27	-3.306	Fe I	15.6
10725.19	26.0	3.64	-2.948	Fe I	15.7
10753.00	26.0	3.96	-2.077	Fe I	39.7
10780.69	26.0	3.24	-3.553	Fe I	10.4
10783.05	26.0	3.11	-2.786	Fe I	47.0
10818.28	26.0	3.96	-2.160	Fe I	35.6
10863.52	26.0	4.73	-0.877	Fe I	67.1
10884.26	26.0	3.93	-2.129	Fe I	39.1
10896.30	26.0	3.07	-2.911	Fe I	42.9
11013.24	26.0	4.80	-1.240	Fe I	42.4
11026.79	26.0	3.94	-2.517	Fe I	21.2
11119.80	26.0	2.85	-2.452	Fe I	84.8
11641.80	26.0	4.58	-2.116	Fe I	15.6
11778.42	26.0	5.34	-1.708	Fe I	8.4
12053.08	26.0	4.56	-1.602	Fe I	41.3
12119.50	26.0	4.59	-1.897	Fe I	25.0
12213.34	26.0	4.64	-2.006	Fe I	19.1
12227.11	26.0	4.61	-1.408	Fe I	51.5
12244.92	26.0	3.64	-3.222	Fe I	11.8
12340.48	26.0	2.28	-4.680	Fe I	9.4
12342.92	26.0	4.64	-1.545	Fe I	42.1
12510.52	26.0	4.96	-1.930	Fe I	12.9
12557.00	26.0	2.28	-4.026	Fe I	33.8
12615.93	26.0	4.64	-1.686	Fe I	35.7
12638.70	26.0	4.56	-0.679	Fe I	112.3
12807.15	26.0	3.64	-2.649	Fe I	37.1
12808.24	26.0	4.99	-1.811	Fe I	16.4
12824.86	26.0	3.02	-3.612	Fe I	20.1
12840.57	26.0	4.96	-1.612	Fe I	25.3
12879.77	26.0	2.28	-3.525	Fe I	68.7
12896.12	26.0	4.91	-1.713	Fe I	23.2
12933.01	26.0	5.02	-1.879	Fe I	13.9
12934.67	26.0	5.39	-1.103	Fe I	30.9
13014.84	26.0	5.45	-1.542	Fe I	12.3
13352.17	26.0	5.31	-0.355	Fe I	94.4
13392.10	26.0	5.35	-0.105	Fe I	115.1

Table A.1: continued.

Wavelength Å	Atomic number	Excitation potential eV	$\log gf$	Element	Solar EW mÅ
15194.49	26.0	2.22	-4.808	Fe I	14.1
15201.57	26.0	5.49	-1.315	Fe I	29.0
15207.53	26.0	5.38	0.311	Fe I	215.9
15335.38	26.0	5.41	0.252	Fe I	205.2
15490.34	26.0	2.20	-4.787	Fe I	16.1
15593.74	26.0	5.03	-1.796	Fe I	28.0
15611.15	26.0	3.42	-2.966	Fe I	51.6
15631.95	26.0	5.35	0.171	Fe I	207.0
15648.51	26.0	5.43	-0.633	Fe I	93.8
15676.58	26.0	5.11	-1.848	Fe I	22.3
16198.50	26.0	5.41	-0.376	Fe I	131.4
17420.83	26.0	3.88	-3.628	Fe I	6.7
19923.34	26.0	5.02	-1.536	Fe I	49.7
21851.38	26.0	3.64	-3.578	Fe I	12.7
22257.11	26.0	5.06	-0.704	Fe I	132.5
22380.80	26.0	5.03	-0.377	Fe I	179.4
22392.88	26.0	5.10	-1.330	Fe I	60.8
22619.84	26.0	4.99	-0.564	Fe I	158.2
23308.48	26.0	4.08	-2.705	Fe I	31.3
10427.31	26.1	6.08	-1.575	Fe II	13.7
10501.50	26.1	5.55	-1.861	Fe II	19.5
10862.64	26.1	5.59	-2.006	Fe II	15.3
11125.58	26.1	5.62	-2.213	Fe II	10.5
13251.14	26.1	9.41	0.768	Fe II	13.4

Appendix

B

SWEET-Cat update of 50 planet hosts

∞

Table B.1: Derived parameters for the 50 stars in our sample. The S/N was measured by ARES.

Star	T_{eff} [K]	$\log g$ [cgs]	[Fe / H]	ξ_{micro} [km/s]	ξ_{micro} fixed?	Instrument	S/N
BD -11 4672	4553 ± 75	4.87 ± 0.51	-0.30 ± 0.02	0.14 ± 0.07	yes	FIES	487
BD +49 828	5015 ± 36	$2.87 \pm 0.09^{\text{a}}$	-0.01 ± 0.03	1.48 ± 0.04	no	FIES	567
GJ 785	5087 ± 48	4.42 ± 0.10	-0.01 ± 0.03	0.69 ± 0.10	no	HARPS	801
HATS-1	5969 ± 46	4.39 ± 0.06	-0.04 ± 0.04	1.06 ± 0.08	no	UVES	155
HATS-5	5383 ± 91	4.41 ± 0.22	0.08 ± 0.06	0.91 ± 0.14	no	UVES	158
HAT-P-12	4642 ± 106	4.53 ± 0.27	-0.26 ± 0.06	0.28 ± 0.63	no	FIES	185
HAT-P-24	6470 ± 181	4.33 ± 0.27	-0.41 ± 0.10	1.40 ± 0.03	yes	UVES	158
HAT-P-39	6745 ± 236	4.39 ± 0.47	-0.21 ± 0.12	1.53 ± 0.04	yes	UVES	127
HAT-P-42	5903 ± 66	$4.29 \pm 0.10^{\text{a}}$	0.34 ± 0.05	1.19 ± 0.08	no	UVES	130
HAT-P-46	6421 ± 121	$4.53 \pm 0.14^{\text{a}}$	0.16 ± 0.09	1.67 ± 0.18	no	UVES	208
HD 120084	4969 ± 40	$2.94 \pm 0.14^{\text{a}}$	0.12 ± 0.03	1.41 ± 0.04	no	ESPaDOnS	852

Table B.1: continued.

Star	T_{eff} [K]	$\log g$ [cgs]	[Fe / H]	ξ_{micro} [km/s]	ξ_{micro} fixed?	Instrument	S/N
HD 192263	4946 ± 46	4.61 ± 0.14	-0.05 ± 0.02	0.66 ± 0.12	no	HARPS	415
HD 219134	4767 ± 70	4.57 ± 0.17	0.00 ± 0.04	0.59 ± 0.24	no	ESPaDOnS	725
HD 220842	5999 ± 39	$4.30 \pm 0.06^{\text{a}}$	-0.08 ± 0.03	1.21 ± 0.05	no	FIES	459
HD 233604	4954 ± 46	$2.86 \pm 0.11^{\text{a}}$	-0.14 ± 0.04	1.61 ± 0.05	no	FIES	314
HD 283668	4841 ± 73	4.51 ± 0.18	-0.74 ± 0.04	0.16 ± 0.61	no	FIES	592
HD 285507	4620 ± 126	4.72 ± 0.61	0.04 ± 0.06	0.74 ± 0.43	no	UVES	239
HD 5583	4986 ± 35	$2.87 \pm 0.09^{\text{a}}$	-0.35 ± 0.03	1.62 ± 0.04	no	FIES	933
HD 81688	4903 ± 21	$2.70 \pm 0.05^{\text{a}}$	-0.21 ± 0.02	1.54 ± 0.02	no	^b	1350, 860
HD 82886	5123 ± 18	$3.30 \pm 0.04^{\text{a}}$	-0.25 ± 0.01	1.16 ± 0.02	no	^c	1198, 1294
HD 87883	4917 ± 68	4.53 ± 0.19	0.02 ± 0.03	0.46 ± 0.21	no	ESPaDOnS	753
HIP 107773	4957 ± 49	$2.83 \pm 0.09^{\text{a}}$	0.04 ± 0.04	1.49 ± 0.05	no	UVES	218
HIP 11915	5770 ± 14	4.33 ± 0.03	-0.06 ± 0.01	0.95 ± 0.02	no	HARPS	709
HIP 116454	5042 ± 72	4.69 ± 0.15	-0.16 ± 0.03	0.71 ± 0.17	no	UVES	412
HR 228	5042 ± 42	$3.30 \pm 0.09^{\text{a}}$	0.07 ± 0.03	1.14 ± 0.04	no	UVES	400
KELT-6	6246 ± 88	$4.22 \pm 0.09^{\text{a}}$	-0.22 ± 0.06	1.66 ± 0.13	no	FIES	374
Kepler-37	5378 ± 53	4.47 ± 0.12	-0.23 ± 0.04	0.58 ± 0.13	no	FIES	205
Kepler-444	5111 ± 43	4.50 ± 0.13	-0.51 ± 0.03	0.37 ± 0.15	no	FIES	675
mu Leo	4605 ± 94	$2.61 \pm 0.26^{\text{a}}$	0.25 ± 0.06	1.64 ± 0.11	no	ESPaDOnS	354
ome Ser	4928 ± 35	$2.69 \pm 0.06^{\text{a}}$	-0.11 ± 0.03	1.55 ± 0.04	no	FIES	1168
omi UMa	5499 ± 52	$3.36 \pm 0.07^{\text{a}}$	-0.01 ± 0.05	1.98 ± 0.06	no	ESPaDOnS	527
Qatar-2	4637 ± 316	4.53 ± 0.62	0.09 ± 0.17	0.63 ± 0.83	no	UVES	97
SAND364	4457 ± 104	$2.26 \pm 0.20^{\text{a}}$	-0.04 ± 0.06	1.60 ± 0.11	no	UVES	220
TYC+1422-614-1	4908 ± 41	$2.90 \pm 0.12^{\text{a}}$	-0.07 ± 0.03	1.57 ± 0.05	no	FIES	506
WASP-37	5917 ± 72	4.25 ± 0.15	-0.23 ± 0.05	0.59 ± 0.13	no	FIES	232
WASP-44	5612 ± 80	4.39 ± 0.30	0.17 ± 0.06	1.32 ± 0.13	no	UVES	125
WASP-52	5197 ± 83	4.55 ± 0.30	0.15 ± 0.05	1.16 ± 0.14	no	UVES	125

Table B.1: continued.

Star	T_{eff} [K]	$\log g$ [cgs]	[Fe / H]	ξ_{micro} [km/s]	ξ_{micro} fixed?	Instrument	S/N
WASP-58	6039 ± 55	4.23 ± 0.10	-0.09 ± 0.04	1.12 ± 0.08	no	FIES	310
WASP-61	6265 ± 168	$4.21 \pm 0.21^{\text{a}}$	-0.38 ± 0.11	1.44 ± 0.02	yes	UVES	163
WASP-72	6570 ± 85	4.25 ± 0.13	0.15 ± 0.06	2.30 ± 0.15	no	UVES	174
WASP-73	6203 ± 32	$4.16 \pm 0.06^{\text{a}}$	0.20 ± 0.02	1.66 ± 0.04	no	^d	193,231
WASP-75	6203 ± 46	$4.42 \pm 0.22^{\text{a}}$	0.24 ± 0.03	1.45 ± 0.06	no	UVES	189
WASP-76	6347 ± 52	$4.29 \pm 0.08^{\text{a}}$	0.36 ± 0.04	1.73 ± 0.06	no	UVES	165
WASP-82	6563 ± 55	$4.29 \pm 0.10^{\text{a}}$	0.18 ± 0.04	1.93 ± 0.08	no	UVES	239
WASP-88	6450 ± 61	$4.24 \pm 0.06^{\text{a}}$	0.03 ± 0.04	1.79 ± 0.09	no	UVES	174
WASP-94 A	6259 ± 34	$4.34 \pm 0.07^{\text{a}}$	0.35 ± 0.03	1.50 ± 0.04	no	UVES	356
WASP-94 B	6137 ± 21	$4.42 \pm 0.05^{\text{a}}$	0.33 ± 0.02	1.29 ± 0.03	no	UVES	397
WASP-95	5799 ± 31	$4.29 \pm 0.05^{\text{a}}$	0.22 ± 0.03	1.18 ± 0.04	no	UVES	247
WASP-97	5723 ± 52	4.24 ± 0.07	0.31 ± 0.04	1.03 ± 0.08	no	UVES	219
WASP-99	6324 ± 89	4.34 ± 0.12	0.27 ± 0.06	1.83 ± 0.12	no	UVES	249
WASP-100	6853 ± 209	$4.15 \pm 0.26^{\text{a}}$	-0.30 ± 0.12	1.87 ± 0.02	yes	UVES	166

^a Spectroscopic $\log g$.

^b Weighted average of ESPaDOnS and FIES results. The parameters are (FIES in parentheses): $T_{\text{eff}} = 4870(4934) \pm 30(29)$, $\log g = 2.50(2.73) \pm 0.14(0.05)$, $[\text{Fe} / \text{H}] = -0.26(-0.19) \pm 0.03(0.02)$, and $\xi_{\text{micro}} = 1.50(1.59) \pm 0.03(0.03)$.

^c Weighted average of ESPaDOnS and FIES results. The parameters are (FIES in parentheses): $T_{\text{eff}} = 5124(5121) \pm 22(29)$, $\log g = 3.30(3.31) \pm 0.05(0.07)$, $[\text{Fe} / \text{H}] = -0.25(-0.24) \pm 0.02(0.02)$, and $\xi_{\text{micro}} = 1.15(1.17) \pm 0.03(0.04)$.

^d Weighted average of UVES and FEROS results. The parameters are (FEROS in parentheses): $T_{\text{eff}} = 6313(6162) \pm 61(37)$, $\log g = 4.26(4.14) \pm 0.15(0.06)$, $[\text{Fe} / \text{H}] = 0.22(0.19) \pm 0.04(0.03)$, and $\xi_{\text{micro}} = 1.85(1.61) \pm 0.08(0.04)$.

Table B.2: Previous parameters from SWEET-Cat.

Star	T_{eff} [K]	$\log g$ [cgs]	[Fe / H]	ξ_{micro} [km/s]	Reference
BD-114672	4475 ± 100	4.10 ± 0.36	-0.48 ± 0.05	0.67 ± 0.16	Moutou et al. (2015)
BD +49 828	4943 ± 30	2.85 ± 0.09	-0.19 ± 0.06	...	Niedzielski et al. (2015b)
GJ 785	5144 ± 50	4.60 ± 0.06	0.08 ± 0.03	...	Howard et al. (2011)
HATS-1	5780 ± 100	4.40 ± 0.08	-0.06 ± 0.12	...	Penev et al. (2013)
HATS-5	5304 ± 50	4.53 ± 0.02	0.19 ± 0.08	...	Zhou et al. (2014)
HAT-P-12	4650 ± 60	4.61 ± 0.02	-0.29 ± 0.05	...	Lee et al. (2014)
HAT-P-24	6373 ± 80	4.29 ± 0.04	-0.16 ± 0.08	...	Kipping et al. (2010)
HAT-P-39	6340 ± 100	4.16 ± 0.03	0.19 ± 0.10	...	Hartman et al. (2012)
HAT-P-46	6120 ± 100	4.25 ± 0.11	0.30 ± 0.10	$0.85 \pm ...$	Hartman et al. (2014b)
HAT-P-42	5743 ± 50	4.14 ± 0.07	0.27 ± 0.08	...	Boisse et al. (2013)
HD 120084	4892 ± 22	2.71 ± 0.08	0.09 ± 0.05	1.31 ± 0.10	Sato et al. (2013a)
HD 192263	4906 ± 57	4.36 ± 0.17	-0.07 ± 0.02	0.78 ± 0.12	Tsantaki et al. (2013)
HD 219134	4699 ± 16	4.63 ± 0.10	0.11 ± 0.04	0.35 ± 0.19	Motalebi et al. (2015)
HD 220074	3935 ± 110	1.30 ± 0.50	-0.25 ± 0.25	1.60 ± 0.30	Lee et al. (2013)
HD 220842	5920 ± 20	4.24 ± 0.02	-0.17 ± 0.02	...	Hébrard et al. (2016)
HD 233604	4791 ± 45	2.55 ± 0.18	-0.36 ± 0.04	...	Nowak et al. (2013)
HD 283668	4845 ± 66	4.35 ± 0.12	-0.75 ± 0.12	0.02 ± 0.30	Wilson et al. (2016)
HD 285507	4503 ± 73	4.67 ± 0.06	0.13 ± 0.01	...	Quinn et al. (2014)
HD 5583	4830 ± 45	2.53 ± 0.14	-0.50 ± 0.18	...	Niedzielski et al. (2016)
HD 81688	4753 ± 15	2.22 ± 0.05	-0.36 ± 0.02	1.43 ± 0.05	Sato et al. (2008)
HD 82886	5112 ± 44	3.40 ± 0.06	-0.31 ± 0.03	...	Johnson et al. (2011)
HD 87883	4958 ± 44	4.56 ± 0.06	0.07 ± 0.03	...	Valenti and Fischer (2005)
HIP 107773	4945 ± 100	2.60 ± 0.20	0.03 ± 0.10	...	Jones et al. (2015)
HIP 11915	5760 ± 4	4.46 ± 0.01	-0.06 ± 0.00	...	Bedell et al. (2015)
HIP 116454	5089 ± 50	4.59 ± 0.03	-0.16 ± 0.08	...	Vanderburg et al. (2015)
HR 228	4959 ± 25	3.16 ± 0.08	0.01 ± 0.04	1.12 ± 0.07	Sato et al. (2013b)

Table B.2: continued.

Star	T_{eff} [K]	$\log g$ [cgs]	[Fe / H]	ξ_{micro} [km/s]	Reference
KELT-6	6102 ± 43	4.07 ± 0.06	-0.28 ± 0.04	...	Collins et al. (2014)
Kepler-37	5417 ± 70	4.57 ± 0.01	-0.32 ± 0.07	...	Barclay et al. (2013)
Kepler-444	5046 ± 74	4.60 ± 0.06	-0.55 ± 0.07	...	Campante et al. (2015)
mu Leo	4538 ± 27	2.40 ± 0.10	0.36 ± 0.05	1.40 ± 0.10	Lee et al. (2014)
ome Ser	4770 ± 10	2.32 ± 0.04	-0.24 ± 0.02	1.34 ± 0.04	Sato et al. (2013a)
omi UMa	5242 ± 10	2.64 ± 0.03	-0.09 ± 0.02	1.51 ± 0.07	Sato et al. (2012)
Qatar-2	4645 ± 50	4.60 ± 0.02	-0.02 ± 0.08	...	Bryan et al. (2012)
SAND364	4284 ± 9	2.20 ± 0.06	-0.02 ± 0.04	...	Brucalassi et al. (2014)
TYC+1422-614-1	4806 ± 45	2.85 ± 0.18	-0.20 ± 0.08	...	Niedzielski et al. (2015a)
WASP-37	5940 ± 55	4.39 ± 0.02	-0.40 ± 0.12	...	Simpson et al. (2011)
WASP-44	5400 ± 150	4.48 ± 0.07	0.06 ± 0.10	...	Anderson et al. (2012)
WASP-52	5000 ± 100	4.58 ± 0.01	0.03 ± 0.12	...	Hébrard et al. (2013)
WASP-58	5800 ± 150	4.27 ± 0.09	-0.45 ± 0.09	...	Hébrard et al. (2013)
WASP-61	6250 ± 150	4.26 ± 0.01	-0.10 ± 0.12	...	Hellier et al. (2012)
WASP-72	6250 ± 100	4.08 ± 0.13	-0.06 ± 0.09	1.60 ± 0.10	Gillon et al. (2013)
WASP-73	6030 ± 120	3.92 ± 0.08	0.14 ± 0.14	1.10 ± 0.20	Delrez et al. (2014)
WASP-75	6100 ± 100	4.50 ± 0.10	0.07 ± 0.09	1.30 ± 0.10	Gómez Maqueo Chew et al. (2013)
WASP-76	6250 ± 100	4.13 ± 0.02	0.23 ± 0.10	1.40 ± 0.10	West et al. (2016)
WASP-82	6490 ± 100	3.97 ± 0.02	0.12 ± 0.11	1.50 ± 0.10	West et al. (2016)
WASP-88	6430 ± 130	4.03 ± 0.09	-0.08 ± 0.12	1.40 ± 0.10	Delrez et al. (2014)
WASP-94 A	6170 ± 80	4.27 ± 0.07	0.26 ± 0.15	...	Neveu-VanMalle et al. (2014)
WASP-94 B	6040 ± 90	4.26 ± 0.06	0.23 ± 0.14	...	Neveu-VanMalle et al. (2014)
WASP-95	5630 ± 130	4.38 ± 0.03	0.14 ± 0.16	...	Hellier et al. (2014)
WASP-97	5640 ± 100	4.43 ± 0.03	0.23 ± 0.11	...	Hellier et al. (2014)
WASP-99	6180 ± 100	4.12 ± 0.03	0.21 ± 0.15	...	Hellier et al. (2014)
WASP-100	6900 ± 120	4.04 ± 0.11	-0.03 ± 0.10	...	Hellier et al. (2014)

FASMA and machine learning

With the increasing amount of astrophysical data, it is important to perform a rapid and trustworthy analysis. This is one of the strengths for **FASMA** when dealing with high quality spectroscopic data for determination of stellar atmospheric parameters. Here a classic method to analyse these large amount of data has been modernised with a new minimisation technique that utilise the physical knowledge about the system. However smart it may sound like, it can be improved. The time consuming part in **FASMA** are the calls to **MOOG**. In the end a couple of minutes are spent on the minimisation on a modern computer.

This lead to a side-project: explorer the use of machine learning to determine stellar atmospheric parameters. Machine learning (ML) is not a new topic in computer science, but it is a tool that is steadily becoming more and more popular in today's science. The effort of using ML here is meant as a proof of concept, and something that can be improved upon in the future.

The idea was to remove the expensive calls to **MOOG** completely. Two things are required in order to do so in the approach presented here:

1. Stellar atmospheric parameters of a large sample of stars with a big span in the parameter space
2. The EW measurements of as many absorption lines as possible (in this case Fe I and Fe II)

Additionally it is here required that the above two points are obtained in a homogeneous way. Luckily such a sample was already analysed during this thesis as a test of **FASMA** (see Section 3.2.2.6) where a sample of 582 stars were analysed; all of which meet the above required criteria.

This data set of measurements of EWs and the parameters were organised and prepared in a big table as follows:

- Each row contains both the measurements of the EWs (first N columns) and the parameters (last four columns). The parameters are T_{eff} , $\log g$, $[\text{Fe}/\text{H}]$, and ξ_{micro}
- The columns excluding the last four are labelled with the wavelength of the absorption line
- All wavelength columns which contained at least one missing measurement of the EW for any of the 582 stars were removed

There are 58 wavelength columns after removing wavelength columns with missing measurements. Before the removal there were 299 columns with wavelength. In this case the **scikit-learn** package¹ from the

¹ <http://scikit-learn.org/>

Python ecosystem was used to train the data set. This package also include a tool to split the data into a training part and testing part. This is particular useful when trying to evaluate the accuracy of the model used. Here the training consist of 2/3 of the data, and the rest is for testing. This splitting is done randomly, giving slight different results each time the script is executed.

The training itself is quite fast (less than 10s). However, the real power comes when the trained model is saved to the disk, which can later be loaded again. In this way the training will only be done once. Using the model to obtain the parameters is much less than 1 s, which makes is many orders of magnitudes faster² than a more traditional approach as with **FASMA**.

When testing the model trained, the 1/3 data set is used to derive parameters. Those derived parameters are then compared to the actual parameters with a mean absolute error. This gives an idea of the accuracy. In Figure C.1 the script was run 1000 times (the splitting was done randomly in each run), and the error for each parameter is shown as a histogram. The mean errors for each parameters are roughly T_{eff} : 47 K, $\log g$: 0.10 dex, $[\text{Fe}/\text{H}]$: 0.038 dex, and ξ_{micro} : 0.12 km/s.

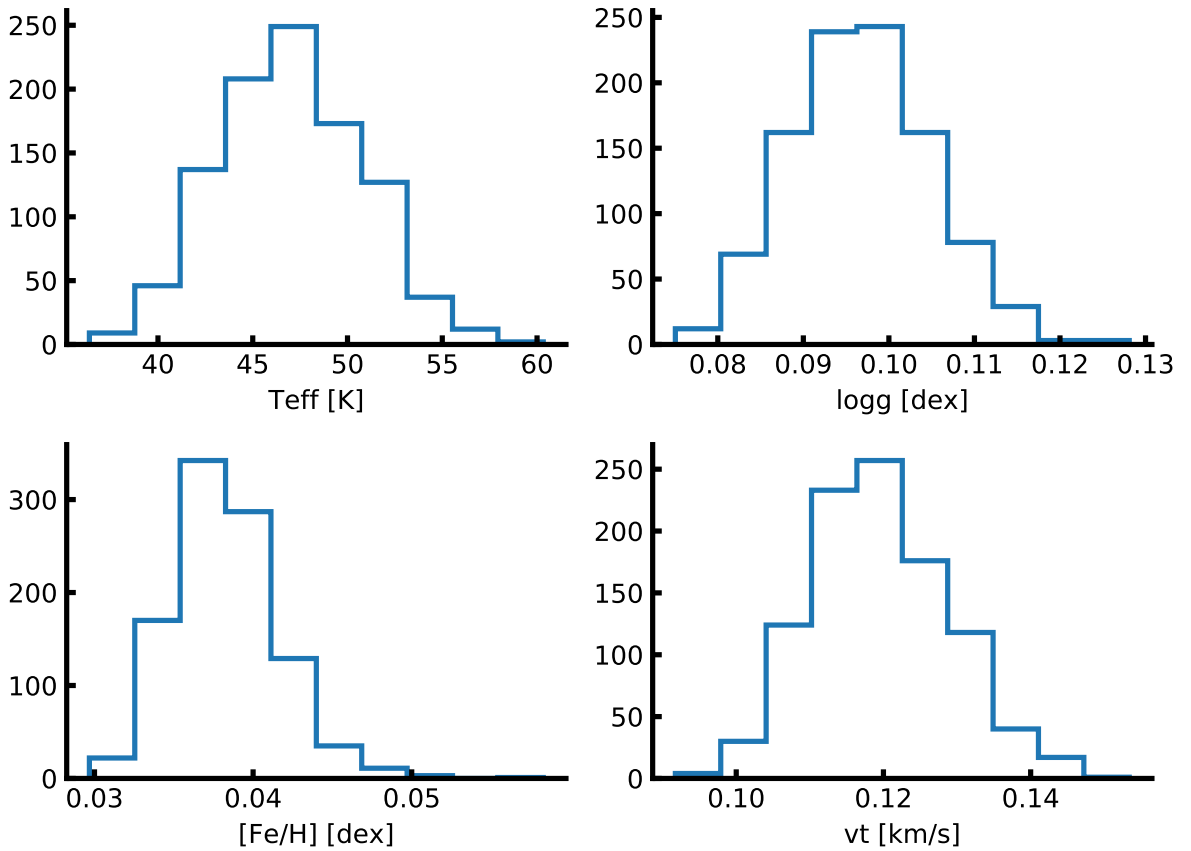


Figure C.1: Mean absolute error on each parameter after 1000 runs.

There exists many different algorithms within **scikit-learn** to train the final model. In the test here a simple **LinearRegression** was used. Other algorithms were tested as well, such as **Ridge** and **Lasso**, however with very similar results. The main difference between the different algorithms are found in the details on how the minimisation is done. This is described in great detail in the online documentation.

² Improvements in the order of millions have been obtained here.

Bibliography

- Adamów, M., Niedzielski, A., Villaver, E., Wolszczan, A., and Nowak, G.: 2014, *A&A* **569**, A55
- Adibekyan, V., Delgado-Mena, E., Figueira, P., Sousa, S. G., Santos, N. C., González Hernández, J. I., Minchev, I., Faria, J. P., Israelian, G., Harutyunyan, G., Suárez-Andrés, L., and Hakobyan, A. A.: 2016, *A&A* **592**, A87
- Adibekyan, V. Z., Benamati, L., Santos, N. C., Alves, S., Lovis, C., Udry, S., Israelian, G., Sousa, S. G., Tsantaki, M., Mortier, A., Sozzetti, A., and De Medeiros, J. R.: 2015, *MNRAS* **450**, 1900
- Adibekyan, V. Z., Figueira, P., Santos, N. C., Mortier, A., Mordasini, C., Delgado Mena, E., Sousa, S. G., Correia, A. C. M., Israelian, G., and Oshagh, M.: 2013, *A&A* **560**, A51
- Adibekyan, V. Z., Santos, N. C., Sousa, S. G., Israelian, G., Delgado Mena, E., González Hernández, J. I., Mayor, M., Lovis, C., and Udry, S.: 2012a, *A&A* **543**, A89
- Adibekyan, V. Z., Sousa, S. G., Santos, N. C., Delgado Mena, E., González Hernández, J. I., Israelian, G., Mayor, M., and Khachatryan, G.: 2012b, *A&A* **545**, A32
- Agol, E., Steffen, J., Sari, R., and Clarkson, W.: 2005, *MNRAS* **359**, 567
- Alibert, Y.: 2014, *A&A* **561**, A41
- Anderson, D. R., Collier Cameron, A., Gillon, M., Hellier, C., Jehin, E., Lendl, M., Maxted, P. F. L., Queloz, D., Smalley, B., Smith, A. M. S., Triaud, A. H. M. J., West, R. G., Pepe, F., Pollacco, D., Ségransan, D., Todd, I., and Udry, S.: 2012, *MNRAS* **422**, 1988
- Andreasen, D. T., Sousa, S. G., Delgado Mena, E., Santos, N. C., Lebzelter, T., Mucciarelli, A., and Neil, J. J.: 2017a, *A&A* **585**, A143
- Andreasen, D. T., Sousa, S. G., Delgado Mena, E., Santos, N. C., Tsantaki, M., Rojas-Ayala, B., and Neves, V.: 2016, *A&A* **585**, A143
- Andreasen, D. T., Sousa, S. G., Tsantaki, M., Teixeira, G. D. C., Mortier, A., Santos, N. C., Suárez-Andrés, L., Delgado Mena, E., and Ferreira, A. C. S.: 2017b, *A&A* **600**, A69
- Apai, D., Kasper, M., Skemer, A., Hanson, J. R., Lagrange, A.-M., Biller, B. A., Bonnefoy, M., Buenzli, E., and Vigan, A.: 2016, *ApJ* **820**, 40

- Arnold, L., Gillet, S., Lardi re, O., Riaud, P., and Schneider, J.: 2002, *A&A* **392**, 231
- Baglin, A., Auvergne, M., Boisnard, L., Lam-Trong, T., Barge, P., Catala, C., Deleuil, M., Michel, E., and Weiss, W.: 2006, in *36th COSPAR Scientific Assembly*, Vol. 36 of *COSPAR Meeting*
- Bakos, G., Noyes, R. W., Kov cs, G., Stanek, K. Z., Sasselov, D. D., and Domsa, I.: 2004, *Publications of the ASP* **116**, 266
- Balachandran, S.: 1990, *ApJ* **354**, 310
- Barclay, T., Rowe, J. F., Lissauer, J. J., Huber, D., Fressin, F., Howell, S. B., Bryson, S. T., Chaplin, W. J., D sert, J.-M., Lopez, E. D., Marcy, G. W., Mullally, F., Ragozzine, D., Torres, G., Adams, E. R., Agol, E., Barrado, D., Basu, S., Bedding, T. R., Buchhave, L. A., Charbonneau, D., Christiansen, J. L., Christensen-Dalsgaard, J., Ciardi, D., Cochran, W. D., Dupree, A. K., Elsworth, Y., Everett, M., Fischer, D. A., Ford, E. B., Fortney, J. J., Geary, J. C., Haas, M. R., Handberg, R., Hekker, S., Henze, C. E., Horch, E., Howard, A. W., Hunter, R. C., Isaacson, H., Jenkins, J. M., Karoff, C., Kawaler, S. D., Kjeldsen, H., Klaus, T. C., Latham, D. W., Li, J., Lillo-Box, J., Lund, M. N., Lundkvist, M., Metcalfe, T. S., Miglio, A., Morris, R. L., Quintana, E. V., Stello, D., Smith, J. C., Still, M., and Thompson, S. E.: 2013, *Nature* **494**, 452
- Baumann, P., Ram rez, I., Mel ndez, J., Asplund, M., and Lind, K.: 2010, *A&A* **519**, A87
- Bedding, T. R., Mosser, B., Huber, D., Montalb n, J., Beck, P., Christensen-Dalsgaard, J., Elsworth, Y. P., Garc a, R. A., Miglio, A., Stello, D., White, T. R., De Ridder, J., Hekker, S., Aerts, C., Barban, C., Belkacem, K., Broomhall, A.-M., Brown, T. M., Buzasi, D. L., Carrier, F., Chaplin, W. J., di Mauro, M. P., Dupret, M.-A., Frandsen, S., Gilliland, R. L., Goupil, M.-J., Jenkins, J. M., Kallinger, T., Kawaler, S., Kjeldsen, H., Mathur, S., Noels, A., Silva Aguirre, V., and Ventura, P.: 2011, *Nature* **471**, 608
- Bedell, M., Mel ndez, J., Bean, J. L., Ram rez, I., Asplund, M., Alves-Brito, A., Casagrande, L., Dreizler, S., Monroe, T., Spina, L., and Tucci Maia, M.: 2015, *A&A* **581**, A34
- Berdi nas, Z. M., Rodr guez-L pez, C., Amado, P. J., Anglada-Escud , G., Barnes, J. R., MacDonald, J., Zechmeister, M., and Sarmiento, L. F.: 2017, *MNRAS* **469**, 4268
- Bertaux, J. L., Lallement, R., Ferron, S., Boonne, C., and Bodichon, R.: 2014, *A&A* **564**, A46
- Beuzit, J.-L., Feldt, M., Dohlen, K., Mouillet, D., Puget, P., Wildi, F., Abe, L., Antichi, J., Baruffolo, A., Baudoz, P., Boccaletti, A., Carbillet, M., Charton, J., Claudi, R., Downing, M., Fabron, C., Feautrier, P., Fedrigo, E., Fusco, T., Gach, J.-L., Gratton, R., Henning, T., Hubin, N., Joos, F., Kasper, M., Langlois, M., Lenzen, R., Moutou, C., Pavlov, A., Petit, C., Pragt, J., Rabou, P., Rigal, F., Roelfsema, R., Rousset, G., Saisse, M., Schmid, H.-M., Stadler, E., Thalmann, C., Turatto, M., Udry, S., Vakili, F., and Waters, R.: 2008, in *Ground-based and Airborne Instrumentation for Astronomy II*, Vol. 7014 of *Proceedings of the SPIE*, p. 701418
- Blackwell, D. E. and Shallis, M. J.: 1977, *MNRAS* **180**, 177
- Bochanski, J. J., Hawley, S. L., Covey, K. R., West, A. A., Reid, I. N., Golimowski, D. A., and Ivezi ,  .: 2010, *AJ* **139**, 2679

- Boisse, I., Hartman, J. D., Bakos, G. Á., Penev, K., Csubry, Z., Béky, B., Latham, D. W., Bieryla, A., Torres, G., Kovács, G., Buchhave, L. A., Hansen, T., Everett, M., Esquerdo, G. A., Szklenár, T., Falco, E., Shporer, A., Fulton, B. J., Noyes, R. W., Stefanik, R. P., Lázár, J., Papp, I., and Sári, P.: 2013, *A&A* **558**, A86
- Bonfils, X., Delfosse, X., Udry, S., Forveille, T., Mayor, M., Perrier, C., Bouchy, F., Gillon, M., Lovis, C., Pepe, F., Queloz, D., Santos, N. C., Ségransan, D., and Bertaux, J.-L.: 2013, *A&A* **549**, A109
- Bonnefoy, M., Zurlo, A., Baudino, J. L., Lucas, P., Mesa, D., Maire, A.-L., Vigan, A., Galicher, R., Homeier, D., Marocco, F., Gratton, R., Chauvin, G., Allard, F., Desidera, S., Kasper, M., Moutou, C., Lagrange, A.-M., Antichi, J., Baruffolo, A., Baudrand, J., Beuzit, J.-L., Boccaletti, A., Cantalloube, F., Carillet, M., Charton, J., Claudi, R. U., Costille, A., Dohlen, K., Dominik, C., Fantinel, D., Feautrier, P., Feldt, M., Fusco, T., Gigan, P., Girard, J. H., Gluck, L., Gry, C., Henning, T., Janson, M., Langlois, M., Madec, F., Magnard, Y., Maurel, D., Mawet, D., Meyer, M. R., Milli, J., Moeller-Nilsson, O., Mouillet, D., Pavlov, A., Perret, D., Pujet, P., Quanz, S. P., Rochat, S., Rousset, G., Roux, A., Salasnich, B., Salter, G., Sauvage, J.-F., Schmid, H. M., Sevin, A., Soenke, C., Stadler, E., Turatto, M., Udry, S., Vakili, F., Wahhaj, Z., and Wildi, F.: 2016, *A&A* **587**, A58
- Borucki, W. J.: 2017, *Proceedings of the American Philosophical Society* **161**, 38
- Borucki, W. J., Koch, D., Basri, G., Batalha, N., Brown, T., Caldwell, D., Caldwell, J., Christensen-Dalsgaard, J., Cochran, W. D., DeVore, E., Dunham, E. W., Dupree, A. K., Gautier, T. N., Geary, J. C., Gilliland, R., Gould, A., Howell, S. B., Jenkins, J. M., Kondo, Y., Latham, D. W., Marcy, G. W., Meibom, S., Kjeldsen, H., Lissauer, J. J., Monet, D. G., Morrison, D., Sasselov, D., Tarter, J., Boss, A., Brownlee, D., Owen, T., Buzasi, D., Charbonneau, D., Doyle, L., Fortney, J., Ford, E. B., Holman, M. J., Seager, S., Steffen, J. H., Welsh, W. F., Rowe, J., Anderson, H., Buchhave, L., Ciardi, D., Walkowicz, L., Sherry, W., Horch, E., Isaacson, H., Everett, M. E., Fischer, D., Torres, G., Johnson, J. A., Endl, M., MacQueen, P., Bryson, S. T., Dotson, J., Haas, M., Kolodziejczak, J., Van Cleve, J., Chandrasekaran, H., Twicken, J. D., Quintana, E. V., Clarke, B. D., Allen, C., Li, J., Wu, H., Tenenbaum, P., Verner, E., Bruhweiler, F., Barnes, J., and Prsa, A.: 2010, *Science* **327**, 977
- Boss, A. P.: 2002, *ApJL* **567**, L149
- Bouchy, F., Pepe, F., and Queloz, D.: 2001, *A&A* **374**, 733
- Brucalassi, A., Pasquini, L., Saglia, R., Ruiz, M. T., Bonifacio, P., Bedin, L. R., Biazzo, K., Melo, C., Lovis, C., and Randich, S.: 2014, *A&A* **561**, L9
- Bryan, M. L., Alsubai, K. A., Latham, D. W., Parley, N. R., Collier Cameron, A., Quinn, S. N., Carter, J. A., Fulton, B. J., Berlind, P., Brown, W. R., Buchhave, L. A., Calkins, M. L., Esquerdo, G. A., Fűrész, G., Gråe Jørgensen, U., Horne, K. D., Stefanik, R. P., Street, R. A., Torres, G., West, R. G., Dominik, M., Harpsøe, K. B. W., Liebig, C., Calchi Novati, S., Ricci, D., and Skottfelt, J. F.: 2012, *ApJ* **750**, 84
- Buchhave, L. A., Latham, D. W., Johansen, A., Bizzarro, M., Torres, G., Rowe, J. F., Batalha, N. M., Borucki, W. J., Brugamyer, E., Caldwell, C., Bryson, S. T., Ciardi, D. R., Cochran, W. D., Endl, M., Esquerdo, G. A., Ford, E. B., Geary, J. C., Gilliland, R. L., Hansen, T., Isaacson, H., Laird, J. B.,

- Lucas, P. W., Marcy, G. W., Morse, J. A., Robertson, P., Shporer, A., Stefanik, R. P., Still, M., and Quinn, S. N.: 2012, *Nature* **486**, 375
- Cai, K., Durisen, R. H., Michael, S., Boley, A. C., Mejía, A. C., Pickett, M. K., and D'Alessio, P.: 2006, *ApJL* **636**, L149
- Campante, T. L., Barclay, T., Swift, J. J., Huber, D., Adibekyan, V. Z., Cochran, W., Burke, C. J., Isaacson, H., Quintana, E. V., Davies, G. R., Silva Aguirre, V., Ragozzine, D., Riddle, R., Baranec, C., Basu, S., Chaplin, W. J., Christensen-Dalsgaard, J., Metcalfe, T. S., Bedding, T. R., Handberg, R., Stello, D., Brewer, J. M., Hekker, S., Karoff, C., Kolbl, R., Law, N. M., Lundkvist, M., Miglio, A., Rowe, J. F., Santos, N. C., Van Laerhoven, C., Arentoft, T., Elsworth, Y. P., Fischer, D. A., Kawaler, S. D., Kjeldsen, H., Lund, M. N., Marcy, G. W., Sousa, S. G., Sozzetti, A., and White, T. R.: 2015, *ApJ* **799**, 170
- Casagrande, L., Portinari, L., and Flynn, C.: 2006, *MNRAS* **373**, 13
- Cavicchioli, R.: 2002, *Astrobiology* **2**, 281
- Cayrel, R.: 1988, in G. Cayrel de Strobel and M. Spite (eds.), *The Impact of Very High S/N Spectroscopy on Stellar Physics*, Vol. 132 of *IAU Symposium*, p. 345
- Chaplin, W. J., Kjeldsen, H., Christensen-Dalsgaard, J., Basu, S., Miglio, A., Appourchaux, T., Bedding, T. R., Elsworth, Y., García, R. A., Gilliland, R. L., Girardi, L., Houdek, G., Karoff, C., Kawaler, S. D., Metcalfe, T. S., Molenda-Žakowicz, J., Monteiro, M. J. P. F. G., Thompson, M. J., Verner, G. A., Ballot, J., Bonanno, A., Brandão, I. M., Broomhall, A.-M., Bruntt, H., Campante, T. L., Corsaro, E., Creevey, O. L., Doğan, G., Esch, L., Gai, N., Gaulme, P., Hale, S. J., Handberg, R., Hekker, S., Huber, D., Jiménez, A., Mathur, S., Mazumdar, A., Mosser, B., New, R., Pinsonneault, M. H., Pricopi, D., Quirion, P.-O., Régulo, C., Salabert, D., Serenelli, A. M., Silva Aguirre, V., Sousa, S. G., Stello, D., Stevens, I. R., Suran, M. D., Uytterhoeven, K., White, T. R., Borucki, W. J., Brown, T. M., Jenkins, J. M., Kinemuchi, K., Van Cleve, J., and Klaus, T. C.: 2011, *Science* **332**, 213
- Charbonneau, D., Brown, T. M., Noyes, R. W., and Gilliland, R. L.: 2002, *ApJ* **568**, 377
- Christensen-Dalsgaard, J., Kjeldsen, H., Brown, T. M., Gilliland, R. L., Arentoft, T., Frandsen, S., Quirion, P.-O., Borucki, W. J., Koch, D., and Jenkins, J. M.: 2010, *ApJL* **713**, L164
- Collins, K. A., Eastman, J. D., Beatty, T. G., Siverd, R. J., Gaudi, B. S., Pepper, J., Kielkopf, J. F., Johnson, J. A., Howard, A. W., Fischer, D. A., Manner, M., Bieryla, A., Latham, D. W., Fulton, B. J., Gregorio, J., Buchhave, L. A., Jensen, E. L. N., Stassun, K. G., Penev, K., Crepp, J. R., Hinkley, S., Street, R. A., Cargile, P., Mack, C. E., Oberst, T. E., Avril, R. L., Mellon, S. N., McLeod, K. K., Penny, M. T., Stefanik, R. P., Berlind, P., Calkins, M. L., Mao, Q., Richert, A. J. W., DePoy, D. L., Esquerdo, G. A., Gould, A., Marshall, J. L., Oelkers, R. J., Pogge, R. W., Trueblood, M., and Trueblood, P.: 2014, *AJ* **147**, 39
- Cosentino, R., Lovis, C., Pepe, F., Collier Cameron, A., Latham, D. W., Molinari, E., Udry, S., Bezawada, N., Black, M., Born, A., Buchschacher, N., Charbonneau, D., Figueira, P., Fleury, M., Galli, A., Gallie, A., Gao, X., Ghedina, A., Gonzalez, C., Gonzalez, M., Guerra, J., Henry, D., Horne, K., Hughes, I., Kelly, D., Lodi, M., Lunney, D., Maire, C., Mayor, M., Micela, G., Ordway, M. P., Peacock, J., Phillips,

- D., Piotto, G., Pollacco, D., Queloz, D., Rice, K., Riverol, C., Riverol, L., San Juan, J., Sasselov, D., Segransan, D., Sozzetti, A., Sosnowska, D., Stobie, B., Szentgyorgyi, A., Vick, A., and Weber, L.: 2012, in *Ground-based and Airborne Instrumentation for Astronomy IV*, Vol. 8446 of *Proceedings of the SPIE*, p. 84461V
- Czekala, I., Andrews, S. M., Mandel, K. S., Hogg, D. W., and Green, G. M.: 2015, *ApJ* **812**, 128
- Dekker, H., D’Odorico, S., Kaufer, A., Delabre, B., and Kotzlowski, H.: 2000, in M. Iye and A. F. Moorwood (eds.), *Optical and IR Telescope Instrumentation and Detectors*, Vol. 4008 of *Proceedings of the SPIE*, pp 534–545
- Delfosse, X., Bonfils, X., Forveille, T., Udry, S., Mayor, M., Bouchy, F., Gillon, M., Lovis, C., Neves, V., Pepe, F., Perrier, C., Queloz, D., Santos, N. C., and Ségransan, D.: 2013, *A&A* **553**, A8
- Delgado Mena, E., Israelian, G., González Hernández, J. I., Sousa, S. G., Mortier, A., Santos, N. C., Adibekyan, V. Z., Fernandes, J., Rebolo, R., Udry, S., and Mayor, M.: 2014, *A&A* **562**, A92
- Delgado Mena, E., Tsantaki, M., Adibekyan, V. Z., Sousa, S. G., Santos, N. C., González Hernández, J. I., and Israelian, G.: 2017, *ArXiv e-prints*
- Delrez, L., Van Grootel, V., Anderson, D. R., Collier-Cameron, A., Doyle, A. P., Fumel, A., Gillon, M., Hellier, C., Jehin, E., Lendl, M., Neveu-VanMalle, M., Maxted, P. F. L., Pepe, F., Pollacco, D., Queloz, D., Ségransan, D., Smalley, B., Smith, A. M. S., Southworth, J., Triaud, A. H. M. J., Udry, S., and West, R. G.: 2014, *A&A* **563**, A143
- Donati, J.-F.: 2003, in J. Trujillo-Bueno and J. Sanchez Almeida (eds.), *Solar Polarization*, Vol. 307 of *Astronomical Society of the Pacific Conference Series*, p. 41
- Dorn, C., Khan, A., Heng, K., Connolly, J. A. D., Alibert, Y., Benz, W., and Tackley, P.: 2015, *A&A* **577**, A83
- Ducati, J. R.: 2002, *VizieR Online Data Catalog* 2237
- Einstein, A.: 1916, *Annalen der Physik* **354**, 769
- Favata, F., Micela, G., and Sciortino, S.: 1997, *A&A* **323**, 809
- Figueira, P., Faria, J. P., Delgado-Mena, E., Adibekyan, V. Z., Sousa, S. G., Santos, N. C., and Israelian, G.: 2014a, *A&A* **570**, A21
- Figueira, P., Oshagh, M., Adibekyan, V. Z., and Santos, N. C.: 2014b, *A&A* **572**, A51
- Fischer, D. A. and Valenti, J.: 2005, *ApJ* **622**, 1102
- Frandsen, S. and Lindberg, B.: 1999, in H. Karttunen and V. Pirola (eds.), *Astrophysics with the NOT*, p. 71
- Gaia Collaboration, Prusti, T., de Bruijne, J. H. J., Brown, A. G. A., Vallenari, A., Babusiaux, C., Bailer-Jones, C. A. L., Bastian, U., Biermann, M., Evans, D. W., and et al.: 2016, *A&A* **595**, A1

- Gillon, M., Anderson, D. R., Collier-Cameron, A., Doyle, A. P., Fumel, A., Hellier, C., Jehin, E., Lendl, M., Maxted, P. F. L., Montalbán, J., Pepe, F., Pollacco, D., Queloz, D., Ségransan, D., Smith, A. M. S., Smalley, B., Southworth, J., Triaud, A. H. M. J., Udry, S., and West, R. G.: 2013, *A&A* **552**, A82
- Gómez Maqueo Chew, Y., Faedi, F., Pollacco, D., Brown, D. J. A., Doyle, A. P., Collier Cameron, A., Gillon, M., Lendl, M., Smalley, B., Triaud, A. H. M. J., West, R. G., Wheatley, P. J., Busuttil, R., Liebig, C., Anderson, D. R., Armstrong, D. J., Barros, S. C. C., Bento, J., Bochinski, J., Burwitz, V., Delrez, L., Enoch, B., Fumel, A., Haswell, C. A., Hébrard, G., Hellier, C., Holmes, S., Jehin, E., Kolb, U., Maxted, P. F. L., McCormac, J., Miller, G. R. M., Norton, A. J., Pepe, F., Queloz, D., Rodríguez, J., Ségransan, D., Skillen, I., Stassun, K. G., Udry, S., and Watson, C.: 2013, *A&A* **559**, A36
- Gonzalez, G.: 1997, *MNRAS* **285**, 403
- Gonzalez, G.: 2015, *MNRAS* **446**, 1020
- Gonzalez, G., Carlson, M. K., and Tobin, R. W.: 2010, *MNRAS* **403**, 1368
- Gonzalez, G. and Laws, C.: 2000, *AJ* **119**, 390
- Gray, D. F.: 2005, *The Observation and Analysis of Stellar Photospheres*, 3rd ed.
- Griffin, R. and Griffin, R.: 1967, *MNRAS* **137**, 253
- Grundahl, F., Fredslund Andersen, M., Christensen-Dalsgaard, J., Antoci, V., Kjeldsen, H., Handberg, R., Houdek, G., Bedding, T. R., Pallé, P. L., Jessen-Hansen, J., Silva Aguirre, V., White, T. R., Frandsen, S., Albrecht, S., Andersen, M. I., Arentoft, T., Brogaard, K., Chaplin, W. J., Harpsøe, K., Jørgensen, U. G., Karovicova, I., Karoff, C., Kjærgaard Rasmussen, P., Lund, M. N., Sloth Lundkvist, M., Skottfelt, J., Norup Sørensen, A., Tronsgaard, R., and Weiss, E.: 2017, *ApJ* **836**, 142
- Gustafsson, B., Edvardsson, B., Eriksson, K., Jørgensen, U. G., Nordlund, Å., and Plez, B.: 2008, *A&A* **486**, 951
- Hartman, J. D.: 2010, *ApJL* **717**, L138
- Hartman, J. D., Bakos, G. Á., Béky, B., Torres, G., Latham, D. W., Csubry, Z., Penev, K., Shporer, A., Fulton, B. J., Buchhave, L. A., Johnson, J. A., Howard, A. W., Marcy, G. W., Fischer, D. A., Kovács, G., Noyes, R. W., Esquerdo, G. A., Everett, M., Szklenár, T., Quinn, S. N., Bieryla, A., Knox, R. P., Hinz, P., Sasselov, D. D., Fűrész, G., Stefanik, R. P., Lázár, J., Papp, I., and Sári, P.: 2012, *AJ* **144**, 139
- Hartman, J. D., Bakos, G. Á., Torres, G., Kovács, G., Johnson, J. A., Howard, A. W., Marcy, G. W., Latham, D. W., Bieryla, A., Buchhave, L. A., Bhatti, W., Béky, B., Csubry, Z., Penev, K., de Val-Borro, M., Noyes, R. W., Fischer, D. A., Esquerdo, G. A., Everett, M., Szklenár, T., Zhou, G., Bayliss, D., Shporer, A., Fulton, B. J., Sanchis-Ojeda, R., Falco, E., Lázár, J., Papp, I., and Sári, P.: 2014a, *AJ* **147**, 128
- Hartman, J. D., Bakos, G. Á., Torres, G., Kovács, G., Johnson, J. A., Howard, A. W., Marcy, G. W., Latham, D. W., Bieryla, A., Buchhave, L. A., Bhatti, W., Béky, B., Csubry, Z., Penev, K., de Val-Borro, M., Noyes, R. W., Fischer, D. A., Esquerdo, G. A., Everett, M., Szklenár, T., Zhou, G., Bayliss, D., Shporer, A., Fulton, B. J., Sanchis-Ojeda, R., Falco, E., Lázár, J., Papp, I., and Sári, P.: 2014b, *AJ* **147**, 128

- Hébrard, G., Arnold, L., Forveille, T., Correia, A. C. M., Laskar, J., Bonfils, X., Boisse, I., Díaz, R. F., Hagelberg, J., Sahlmann, J., Santos, N. C., Astudillo-Defru, N., Borgniet, S., Bouchy, F., Bourrier, V., Courcol, B., Delfosse, X., Deleuil, M., Demangeon, O., Ehrenreich, D., Gregorio, J., Jovanovic, N., Labrevoir, O., Lagrange, A.-M., Lovis, C., Lozi, J., Moutou, C., Montagnier, G., Pepe, F., Rey, J., Santerne, A., Ségransan, D., Udry, S., Vanhuyse, M., Vigan, A., and Wilson, P. A.: 2016, *A&A* **588**, A145
- Hébrard, G., Collier Cameron, A., Brown, D. J. A., Díaz, R. F., Faedi, F., Smalley, B., Anderson, D. R., Armstrong, D., Barros, S. C. C., Bento, J., Bouchy, F., Doyle, A. P., Enoch, B., Gómez Maqueo Chew, Y., Hébrard, É. M., Hellier, C., Lendl, M., Lister, T. A., Maxted, P. F. L., McCormac, J., Moutou, C., Pollacco, D., Queloz, D., Santerne, A., Skillen, I., Southworth, J., Tregloan-Reed, J., Triaud, A. H. M. J., Udry, S., Vanhuyse, M., Watson, C. A., West, R. G., and Wheatley, P. J.: 2013, *A&A* **549**, A134
- Hellier, C., Anderson, D. R., Cameron, A. C., Delrez, L., Gillon, M., Jehin, E., Lendl, M., Maxted, P. F. L., Pepe, F., Pollacco, D., Queloz, D., Ségransan, D., Smalley, B., Smith, A. M. S., Southworth, J., Triaud, A. H. M. J., Udry, S., and West, R. G.: 2014, *MNRAS* **440**, 1982
- Hellier, C., Anderson, D. R., Collier Cameron, A., Doyle, A. P., Fumel, A., Gillon, M., Jehin, E., Lendl, M., Maxted, P. F. L., Pepe, F., Pollacco, D., Queloz, D., Ségransan, D., Smalley, B., Smith, A. M. S., Southworth, J., Triaud, A. H. M. J., Udry, S., and West, R. G.: 2012, *MNRAS* **426**, 739
- Hinkel, N. R., Young, P. A., Pagano, M. D., Desch, S. J., Anbar, A. D., Adibekyan, V., Blanco-Cuaresma, S., Carlberg, J. K., Delgado Mena, E., Liu, F., Nordlander, T., Sousa, S. G., Korn, A., Gruyters, P., Heiter, U., Jofré, P., Santos, N. C., and Soubiran, C.: 2016, *ApJS* **226**, 4
- Hinkle, K., Wallace, L., and Livingston, W.: 1995a, *Publications of the ASP* **107**, 1042
- Hinkle, K. H., Wallace, L., and Livingston, W.: 1995b, in A. J. Sauval, R. Blomme, and N. Grevesse (eds.), *Laboratory and Astronomical High Resolution Spectra*, Vol. 81 of *Astronomical Society of the Pacific Conference Series*, p. 66
- Holman, M. J. and Murray, N. W.: 2005, *Science* **307**, 1288
- Howard, A. W., Johnson, J. A., Marcy, G. W., Fischer, D. A., Wright, J. T., Henry, G. W., Isaacson, H., Valenti, J. A., Anderson, J., and Piskunov, N. E.: 2011, *ApJ* **730**, 10
- Huber, D., Chaplin, W. J., Christensen-Dalsgaard, J., Gilliland, R. L., Kjeldsen, H., Buchhave, L. A., Fischer, D. A., Lissauer, J. J., Rowe, J. F., Sanchis-Ojeda, R., Basu, S., Handberg, R., Hekker, S., Howard, A. W., Isaacson, H., Karoff, C., Latham, D. W., Lund, M. N., Lundkvist, M., Marcy, G. W., Miglio, A., Silva Aguirre, V., Stello, D., Arentoft, T., Barclay, T., Bedding, T. R., Burke, C. J., Christiansen, J. L., Elsworth, Y. P., Haas, M. R., Kawaler, S. D., Metcalfe, T. S., Mullally, F., and Thompson, S. E.: 2013, *ApJ* **767**, 127
- Huber, D., Silva Aguirre, V., Matthews, J. M., Pinsonneault, M. H., Gaidos, E., García, R. A., Hekker, S., Mathur, S., Mosser, B., Torres, G., Bastien, F. A., Basu, S., Bedding, T. R., Chaplin, W. J., Demory, B.-O., Fleming, S. W., Guo, Z., Mann, A. W., Rowe, J. F., Serenelli, A. M., Smith, M. A., and Stello, D.: 2014, *ApJS* **211**, 2

- Husser, T.-O., Wende-von Berg, S., Dreizler, S., Homeier, D., Reiners, A., Barman, T., and Hauschildt, P. H.: 2013, *A&A* **553**, A6
- Ida, S. and Lin, D. N. C.: 2004, *ApJ* **616**, 567
- Israelian, G., Santos, N. C., Mayor, M., and Rebolo, R.: 2004, *A&A* **414**, 601
- Jofré, P., Heiter, U., Soubiran, C., Blanco-Cuaresma, S., Worley, C. C., Pancino, E., Cantat-Gaudin, T., Magrini, L., Bergemann, M., González Hernández, J. I., Hill, V., Lardo, C., de Laverny, P., Lind, K., Masseron, T., Montes, D., Mucciarelli, A., Nordlander, T., Recio Blanco, A., Sobeck, J., Sordo, R., Sousa, S. G., Tabernero, H., Vallenari, A., and Van Eck, S.: 2014, *A&A* **564**, A133
- Johnson, J. A., Clanton, C., Howard, A. W., Bowler, B. P., Henry, G. W., Marcy, G. W., Crepp, J. R., Endl, M., Cochran, W. D., MacQueen, P. J., Wright, J. T., and Isaacson, H.: 2011, *ApJS* **197**, 26
- Jones, M. I., Jenkins, J. S., Rojo, P., and Melo, C. H. F.: 2011, *A&A* **536**, A71
- Jones, M. I., Jenkins, J. S., Rojo, P., Olivares, F., and Melo, C. H. F.: 2015, *A&A* **580**, A14
- Kasting, J. F.: 1997, *Origins of Life and Evolution of the Biosphere* **27**, 291
- Kasting, J. F. and Siefert, J. L.: 2002, *Science* **296**, 1066
- Kasting, J. F., Whitmire, D. P., and Reynolds, R. T.: 1993, *Icarus* **101**, 108
- Kaufer, A., Stahl, O., Tubbesing, S., Nørregaard, P., Avila, G., Francois, P., Pasquini, L., and Pizzella, A.: 1999, *The Messenger* **95**, 8
- Kennedy, G. M. and Kenyon, S. J.: 2008, *ApJ* **673**, 502
- Kipping, D. M., Bakos, G. Á., Hartman, J., Torres, G., Shporer, A., Latham, D. W., Kovács, G., Noyes, R. W., Howard, A. W., Fischer, D. A., Johnson, J. A., Marcy, G. W., Béky, B., Perumpilly, G., Esquerdo, G. A., Sasselov, D. D., Stefanik, R. P., Lázár, J., Papp, I., and Sári, P.: 2010, *ApJ* **725**, 2017
- Kjeldsen, H. and Bedding, T. R.: 1995, *A&A* **293**, 87
- Kopparapu, R. K., Ramirez, R., Kasting, J. F., Eymet, V., Robinson, T. D., Mahadevan, S., Terrien, R. C., Domagal-Goldman, S., Meadows, V., and Deshpande, R.: 2013, *ApJ* **765**, 131
- Kunitomo, M., Ikoma, M., Sato, B., Katsuta, Y., and Ida, S.: 2011, *ApJ* **737**, 66
- Kupka, F. G., Ryabchikova, T. A., Piskunov, N. E., Stempels, H. C., and Weiss, W. W.: 2000, *Baltic Astronomy* **9**, 590
- Kurucz, R.: 1993, *ATLAS9 Stellar Atmosphere Programs and 2 km/s grid. Kurucz CD-ROM No. 13. Cambridge, Mass.: Smithsonian Astrophysical Observatory, 1993*. 13
- Lebzelter, T., Seifahrt, A., Uttenthaler, S., Ramsay, S., Hartman, H., Nieva, M.-F., Przybilla, N., Smette, A., Wahlgren, G. M., Wolff, B., Hussain, G. A. J., Käuff, H. U., and Seemann, U.: 2012, *A&A* **539**, A109
- Lee, B.-C., Han, I., and Park, M.-G.: 2013, *A&A* **549**, A2

- Lee, B.-C., Han, I., Park, M.-G., Mkrtichian, D. E., Hatzes, A. P., and Kim, K.-M.: 2014, *A&A* **566**, A67
- Lindgren, S., Heiter, U., and Seifahrt, A.: 2016, *A&A* **586**, A100
- Maire, A.-L., Bonnefoy, M., Ginski, C., Vigan, A., Messina, S., Mesa, D., Galicher, R., Gratton, R., Desidera, S., Kopytova, T. G., Millward, M., Thalmann, C., Claudi, R. U., Ehrenreich, D., Zurlo, A., Chauvin, G., Antichi, J., Baruffolo, A., Bazzon, A., Beuzit, J.-L., Blanchard, P., Boccaletti, A., de Boer, J., Carle, M., Cascone, E., Costille, A., De Caprio, V., Delboulb , A., Dohlen, K., Dominik, C., Feldt, M., Fusco, T., Girard, J. H., Giro, E., Gisler, D., Gluck, L., Gry, C., Henning, T., Hubin, N., Hugot, E., Jaquet, M., Kasper, M., Lagrange, A.-M., Langlois, M., Le Mignant, D., Llored, M., Madec, F., Martinez, P., Mawet, D., Milli, J., M ller-Nilsson, O., Mouillet, D., Moulin, T., Moutou, C., Orign , A., Pavlov, A., Petit, C., Pragt, J., Puget, P., Ramos, J., Rochat, S., Roelfsema, R., Salasnich, B., Sauvage, J.-F., Schmid, H. M., Turatto, M., Udry, S., Vakili, F., Wahhaj, Z., Weber, L., and Wildi, F.: 2016, *A&A* **587**, A56
- Mayor, M., Lovis, C., and Santos, N. C.: 2014, *Nature* **513**, 328
- Mayor, M., Pepe, F., Queloz, D., Bouchy, F., Rupprecht, G., Lo Curto, G., Avila, G., Benz, W., Bertaux, J.-L., Bonfils, X., Dall, T., Dekker, H., Delabre, B., Eckert, W., Fleury, M., Gilliotte, A., Gojak, D., Guzman, J. C., Kohler, D., Lizon, J.-L., Longinotti, A., Lovis, C., Megevand, D., Pasquini, L., Reyes, J., Sivan, J.-P., Sosnowska, D., Soto, R., Udry, S., van Kesteren, A., Weber, L., and Weilenmann, U.: 2003, *The Messenger* **114**, 20
- Mayor, M. and Queloz, D.: 1995, *A Jupiter-mass companion to a solar-type star*
- McWilliam, A.: 1990, *ApJS* **74**, 1075
- Mordasini, C., Alibert, Y., Benz, W., Klahr, H., and Henning, T.: 2012, *A&A* **541**, A97
- Mortier, A., Santos, N. C., Sousa, S., Israelian, G., Mayor, M., and Udry, S.: 2013a, *A&A* **551**, A112
- Mortier, A., Santos, N. C., Sousa, S. G., Adibekyan, V. Z., Delgado Mena, E., Tsantaki, M., Israelian, G., and Mayor, M.: 2013b, *A&A* **557**, A70
- Mortier, A., Sousa, S. G., Adibekyan, V. Z., Brand o, I. M., and Santos, N. C.: 2014, *A&A* **572**, A95
- Motalebi, F., Udry, S., Gillon, M., Lovis, C., S gransan, D., Buchhave, L. A., Demory, B. O., Malavolta, L., Dressing, C. D., Sasselov, D., Rice, K., Charbonneau, D., Collier Cameron, A., Latham, D., Molinari, E., Pepe, F., Affer, L., Bonomo, A. S., Cosentino, R., Dumusque, X., Figueira, P., Fiorenzano, A. F. M., Gettel, S., Harutyunyan, A., Haywood, R. D., Johnson, J., Lopez, E., Lopez-Morales, M., Mayor, M., Micela, G., Mortier, A., Nascimbeni, V., Philips, D., Piotto, G., Pollacco, D., Queloz, D., Sozzetti, A., Vanderburg, A., and Watson, C. A.: 2015, *A&A* **584**, A72
- Moutou, C., Lo Curto, G., Mayor, M., Bouchy, F., Benz, W., Lovis, C., Naef, D., Pepe, F., Queloz, D., Santos, N. C., S gransan, D., Sousa, S. G., and Udry, S.: 2015, *A&A* **576**, A48
- Natta, A., Grinin, V., and Mannings, V.: 2000, *Protostars and Planets IV* pp 559–588
- Nelson, B. E., Ford, E. B., and Rasio, F. A.: 2017, *AJ* **154**, 106
- Neuforge-Verheecke, C. and Magain, P.: 1997, *A&A* **328**, 261

- Neveu-VanMalle, M., Queloz, D., Anderson, D. R., Charbonnel, C., Collier Cameron, A., Delrez, L., Gillon, M., Hellier, C., Jehin, E., Lendl, M., Maxted, P. F. L., Pepe, F., Pollacco, D., Ségransan, D., Smalley, B., Smith, A. M. S., Southworth, J., Triaud, A. H. M. J., Udry, S., and West, R. G.: 2014, *A&A* **572**, A49
- Newton, I.: 1687, *Philosophiae Naturalis Principia Mathematica. Auctore Js. Newton*
- Ngo, H., Knutson, H. A., Hinkley, S., Bryan, M., Crepp, J. R., Batygin, K., Crossfield, I., Hansen, B., Howard, A. W., Johnson, J. A., Mawet, D., Morton, T. D., Muirhead, P. S., and Wang, J.: 2016, *ApJ* **827**, 8
- Nicholls, C. P., Lebzelter, T., Smette, A., Wolff, B., Hartman, H., Käuff, H.-U., Przybilla, N., Ramsay, S., Uttenthaler, S., Wahlgren, G. M., Bagnulo, S., Hussain, G. A. J., Nieva, M.-F., Seemann, U., and Seifahrt, A.: 2017, *A&A* **598**, A79
- Niedzielski, A., Villaver, E., Nowak, G., Adamów, M., Kowalik, K., Wolszczan, A., Deka-Szymankiewicz, B., Adamczyk, M., and Maciejewski, G.: 2016, *A&A* **588**, A62
- Niedzielski, A., Villaver, E., Wolszczan, A., Adamów, M., Kowalik, K., Maciejewski, G., Nowak, G., García-Hernández, D. A., Deka, B., and Adamczyk, M.: 2015a, *A&A* **573**, A36
- Niedzielski, A., Wolszczan, A., Nowak, G., Adamów, M., Kowalik, K., Maciejewski, G., Deka-Szymankiewicz, B., and Adamczyk, M.: 2015b, *ApJ* **803**, 1
- Nowak, G., Niedzielski, A., Wolszczan, A., Adamów, M., and Maciejewski, G.: 2013, *ApJ* **770**, 53
- Önehag, A., Heiter, U., Gustafsson, B., Piskunov, N., Plez, B., and Reiners, A.: 2012, *A&A* **542**, A33
- Oshagh, M., Santos, N. C., Boisse, I., Boué, G., Montalto, M., Dumusque, X., and Haghighipour, N.: 2013, *A&A* **556**, A19
- Oshagh, M., Santos, N. C., Ehrenreich, D., Haghighipour, N., Figueira, P., Santerne, A., and Montalto, M.: 2014, *A&A* **568**, A99
- Penev, K., Bakos, G. Á., Bayliss, D., Jordán, A., Mohler, M., Zhou, G., Suc, V., Rabus, M., Hartman, J. D., Mancini, L., Béky, B., Csubry, Z., Buchhave, L., Henning, T., Nikolov, N., Csák, B., Brahm, R., Espinoza, N., Conroy, P., Noyes, R. W., Sasselov, D. D., Schmidt, B., Wright, D. J., Tinney, C. G., Addison, B. C., Lázár, J., Papp, I., and Sári, P.: 2013, *AJ* **145**, 5
- Pepe, F., Cameron, A. C., Latham, D. W., Molinari, E., Udry, S., Bonomo, A. S., Buchhave, L. A., Charbonneau, D., Cosentino, R., Dressing, C. D., Dumusque, X., Figueira, P., Fiorenzano, A. F. M., Gettel, S., Harutyunyan, A., Haywood, R. D., Horne, K., Lopez-Morales, M., Lovis, C., Malavolta, L., Mayor, M., Micela, G., Motalebi, F., Nascimbeni, V., Phillips, D., Piotto, G., Pollacco, D., Queloz, D., Rice, K., Sasselov, D., Ségransan, D., Sozzetti, A., Szentgyorgyi, A., and Watson, C. A.: 2013, *Nature* **503**, 377
- Pepe, F. A., Cristiani, S., Rebolo Lopez, R., Santos, N. C., Amorim, A., Avila, G., Benz, W., Bonifacio, P., Cabral, A., Carvas, P., Cirami, R., Coelho, J., Comari, M., Coretti, I., De Caprio, V., Dekker, H., Delabre, B., Di Marcantonio, P., D’Odorico, V., Fleury, M., García, R., Herreros Linares, J. M., Hughes, I., Iwert, O., Lima, J., Lizon, J.-L., Lo Curto, G., Lovis, C., Manescau, A., Martins, C.,

- Mégevand, D., Moitinho, A., Molaro, P., Monteiro, M., Monteiro, M., Pasquini, L., Mordasini, C., Queloz, D., Rasilla, J. L., Rebordão, J. M., Santana Tschudi, S., Santin, P., Sosnowska, D., Spanò, P., Tenegi, F., Udry, S., Vanzella, E., Viel, M., Zapatero Osorio, M. R., and Zerbi, F.: 2010, in *Ground-based and Airborne Instrumentation for Astronomy III*, Vol. 7735 of *Proceedings of the SPIE*, p. 77350F
- Perryman, M., Hartman, J., Bakos, G. Á., and Lindegren, L.: 2014, *ApJ* **797**, 14
- Piskunov, N. E., Kupka, F., Ryabchikova, T. A., Weiss, W. W., and Jeffery, C. S.: 1995, *A&A Supp.* **112**, 525
- Pollacco, D. L., Skillen, I., Collier Cameron, A., Christian, D. J., Hellier, C., Irwin, J., Lister, T. A., Street, R. A., West, R. G., Anderson, D. R., Clarkson, W. I., Deeg, H., Enoch, B., Evans, A., Fitzsimmons, A., Haswell, C. A., Hodgkin, S., Horne, K., Kane, S. R., Keenan, F. P., Maxted, P. F. L., Norton, A. J., Osborne, J., Parley, N. R., Ryans, R. S. I., Smalley, B., Wheatley, P. J., and Wilson, D. M.: 2006, *Publications of the ASP* **118**, 1407
- Pollack, J. B., Hubickyj, O., Bodenheimer, P., Lissauer, J. J., Podolak, M., and Greenzweig, Y.: 1996, *Icarus* **124**, 62
- Queloz, D., Henry, G. W., Sivan, J. P., Baliunas, S. L., Beuzit, J. L., Donahue, R. A., Mayor, M., Naef, D., Perrier, C., and Udry, S.: 2001, *A&A* **379**, 279
- Quinn, S. N., White, R. J., Latham, D. W., Buchhave, L. A., Torres, G., Stefanik, R. P., Berlind, P., Bieryla, A., Calkins, M. C., Esquerdo, G. A., Fűrész, G., Geary, J. C., and Szentgyorgyi, A. H.: 2014, *ApJ* **787**, 27
- Ramírez, I., Allende Prieto, C., and Lambert, D. L.: 2013, *ApJ* **764**, 78
- Ramírez, I., Fish, J. R., Lambert, D. L., and Allende Prieto, C.: 2012, *ApJ* **756**, 46
- Ramírez, I. and Meléndez, J.: 2005, *ApJ* **626**, 465
- Rauer, H., Catala, C., Aerts, C., Appourchaux, T., Benz, W., Brandeker, A., Christensen-Dalsgaard, J., Deleuil, M., Gizon, L., Goupil, M.-J., Güdel, M., Janot-Pacheco, E., Mas-Hesse, M., Pagano, I., Piotto, G., Pollacco, D., Santos, C., Smith, A., Suárez, J.-C., Szabó, R., Udry, S., Adibekyan, V., Alibert, Y., Almenara, J.-M., Amaro-Seoane, P., Eiff, M. A.-v., Asplund, M., Antonello, E., Barnes, S., Baudin, F., Belkacem, K., Bergemann, M., Bihain, G., Birch, A. C., Bonfils, X., Boisse, I., Bonomo, A. S., Borsa, F., Brandão, I. M., Brocato, E., Brun, S., Burleigh, M., Burston, R., Cabrera, J., Cassisi, S., Chaplin, W., Charpinet, S., Chiappini, C., Church, R. P., Csizmadia, S., Cunha, M., Damasso, M., Davies, M. B., Deeg, H. J., Díaz, R. F., Dreizler, S., Dreyer, C., Eggenberger, P., Ehrenreich, D., Eigmüller, P., Erikson, A., Farmer, R., Feltzing, S., de Oliveira Fialho, F., Figueira, P., Forveille, T., Fridlund, M., García, R. A., Giommi, P., Giuffrida, G., Godolt, M., Gomes da Silva, J., Granzer, T., Grenfell, J. L., Grotzsch-Noels, A., Günther, E., Haswell, C. A., Hatzes, A. P., Hébrard, G., Hekker, S., Helled, R., Heng, K., Jenkins, J. M., Johansen, A., Khodachenko, M. L., Kislyakova, K. G., Kley, W., Kolb, U., Krivova, N., Kupka, F., Lammer, H., Lanza, A. F., Lebreton, Y., Magrin, D., Marcos-Arenal, P., Marrese, P. M., Marques, J. P., Martins, J., Mathis, S., Mathur, S., Messina, S., Miglio, A., Montalbán, J., Montalto, M., Monteiro, M. J. P. F. G., Moradi, H., Moravveji, E., Mordasini, C., Morel, T., Mortier,

- A., Nascimbeni, V., Nelson, R. P., Nielsen, M. B., Noack, L., Norton, A. J., Ofir, A., Oshagh, M., Ouazzani, R.-M., Pápics, P., Parro, V. C., Petit, P., Plez, B., Poretti, E., Quirrenbach, A., Ragazzoni, R., Raimondo, G., Rainer, M., Reese, D. R., Redmer, R., Reffert, S., Rojas-Ayala, B., Roxburgh, I. W., Salmon, S., Santerne, A., Schneider, J., Schou, J., Schuh, S., Schunker, H., Silva-Valio, A., Silvotti, R., Skillen, I., Snellen, I., Sohl, F., Sousa, S. G., Sozzetti, A., Stello, D., Strassmeier, K. G., Švanda, M., Szabó, G. M., Tkachenko, A., Valencia, D., Van Grootel, V., Vauclair, S. D., Ventura, P., Wagner, F. W., Walton, N. A., Weingrill, J., Werner, S. C., Wheatley, P. J., and Zwintz, K.: 2014, *Experimental Astronomy* **38**, 249
- Rodríguez, E., Rodríguez-López, C., López-González, M. J., Amado, P. J., Ocando, S., and Berdiñas, Z. M.: 2016, *MNRAS* **457**, 1851
- Santerne, A., Hébrard, G., Lillo-Box, J., Armstrong, D. J., Barros, S. C. C., Demangeon, O., Barrado, D., Debackere, A., Deleuil, M., Delgado Mena, E., Montalto, M., Pollacco, D., Osborn, H. P., Sousa, S. G., Abe, L., Adibekyan, V., Almenara, J.-M., André, P., Arlic, G., Barthe, G., Bendjoya, P., Behrend, R., Boisse, I., Bouchy, F., Boussier, H., Bretton, M., Brown, D. J. A., Carry, B., Cailleau, A., Conseil, E., Coulon, G., Courcol, B., Dauchet, B., Dalouzy, J.-C., Deldem, M., Desormières, O., Dubreuil, P., Fehrenbach, J.-M., Ferratfiat, S., Girelli, R., Gregorio, J., Jaecques, S., Kugel, F., Kirk, J., Labrevoir, O., Lachurié, J.-C., Lam, K. W. F., Le Guen, P., Martinez, P., Maurin, L. P. A., McCormac, J., Pioppa, J.-B., Quadri, U., Rajpurohit, A., Rey, J., Rivet, J.-P., Roy, R., Santos, N. C., Signoret, F., Strabla, L., Suarez, O., Toubanc, D., Tsantaki, M., Vienney, J.-M., Wilson, P. A., Bachschmidt, M., Colas, F., Gerteis, O., Louis, P., Mario, J.-C., Marlot, C., Montier, J., Perroud, V., Pic, V., Romeuf, D., Ubaud, S., and Verilhac, D.: 2016, *ApJ* **824**, 55
- Santos, N. C., Adibekyan, V., Figueira, P., Andreasen, D. T., Barros, S. C. C., Delgado-Mena, E., Demangeon, O., Faria, J. P., Oshagh, M., Sousa, S. G., Viana, P. T. P., and Ferreira, A. C. S.: 2017, *ArXiv e-prints*
- Santos, N. C., Israelian, G., and Mayor, M.: 2004, *A&A* **415**, 1153
- Santos, N. C., Sousa, S. G., Mortier, A., Neves, V., Adibekyan, V., Tsantaki, M., Delgado Mena, E., Bonfils, X., Israelian, G., Mayor, M., and Udry, S.: 2013, *A&A* **556**, A150
- Sato, B., Izumiura, H., Toyota, E., Kambe, E., Ikoma, M., Omiya, M., Masuda, S., Takeda, Y., Murata, D., Itoh, Y., Ando, H., Yoshida, M., Kokubo, E., and Ida, S.: 2008, *PASJ* **60**, 539
- Sato, B., Omiya, M., Harakawa, H., Izumiura, H., Kambe, E., Takeda, Y., Yoshida, M., Itoh, Y., Ando, H., Kokubo, E., and Ida, S.: 2012, *PASJ* **64**
- Sato, B., Omiya, M., Harakawa, H., Liu, Y.-J., Izumiura, H., Kambe, E., Takeda, Y., Yoshida, M., Itoh, Y., Ando, H., Kokubo, E., and Ida, S.: 2013a, *PASJ* **65**
- Sato, B., Omiya, M., Wittenmyer, R. A., Harakawa, H., Nagasawa, M., Izumiura, H., Kambe, E., Takeda, Y., Yoshida, M., Itoh, Y., Ando, H., Kokubo, E., and Ida, S.: 2013b, *ApJ* **762**, 9
- Seager, S.: 2010, *Exoplanets*, University of Arizona Press
- Shetrone, M., Bizyaev, D., Lawler, J., Allende Prieto, C., Johnson, J. A., Smith, V., Cunha, K., Holtzman, J., Garcia Perez, A., Meszaros, S., Sobek, J., Zamora, O., Garcia-Hernandez, A., Souto, D., Chojnowski, D., Koesterke, L., and Majewski, S.: 2015, *ArXiv e-prints*

- Simpson, E. K., Faedi, F., Barros, S. C. C., Brown, D. J. A., Collier Cameron, A., Hebb, L., Pollacco, D., Smalley, B., Todd, I., Butters, O. W., Hébrard, G., McCormac, J., Miller, G. R. M., Santerne, A., Street, R. A., Skillen, I., Triaud, A. H. M. J., Anderson, D. R., Bento, J., Boisse, I., Bouchy, F., Enoch, B., Haswell, C. A., Hellier, C., Holmes, S., Horne, K., Keenan, F. P., Lister, T. A., Maxted, P. F. L., Moulds, V., Moutou, C., Norton, A. J., Parley, N., Pepe, F., Queloz, D., Segransan, D., Smith, A. M. S., Stempels, H. C., Udry, S., Watson, C. A., West, R. G., and Wheatley, P. J.: 2011, *AJ* **141**, 8
- Smiljanic, R., Korn, A. J., Bergemann, M., Frasca, A., Magrini, L., Masseron, T., Pancino, E., Ruchti, G., San Roman, I., Sbordone, L., Sousa, S. G., Tabernero, H., Tautvaišienė, G., Valentini, M., Weber, M., Worley, C. C., Adibekyan, V. Z., Allende Prieto, C., Barisevičius, G., Biazzo, K., Blanco-Cuaresma, S., Bonifacio, P., Bragaglia, A., Caffau, E., Cantat-Gaudin, T., Chorniy, Y., de Laverny, P., Delgado-Mena, E., Donati, P., Duffau, S., Franciosini, E., Friel, E., Geisler, D., González Hernández, J. I., Gruyters, P., Guiglion, G., Hansen, C. J., Heiter, U., Hill, V., Jacobson, H. R., Jofre, P., Jönsson, H., Lanzafame, A. C., Lardo, C., Ludwig, H.-G., Maiorca, E., Mikolaitis, Š., Montes, D., Morel, T., Mucciarelli, A., Muñoz, C., Nordlander, T., Pasquini, L., Puzeras, E., Recio-Blanco, A., Ryde, N., Sacco, G., Santos, N. C., Serenelli, A. M., Sordo, R., Soubiran, C., Spina, L., Steffen, M., Vallenari, A., Van Eck, S., Villanova, S., Gilmore, G., Randich, S., Asplund, M., Binney, J., Drew, J., Feltzing, S., Ferguson, A., Jeffries, R., Micela, G., Negueruela, I., Prusti, T., Rix, H.-W., Alfaro, E., Babusiaux, C., Bensby, T., Blomme, R., Flaccomio, E., François, P., Irwin, M., Koposov, S., Walton, N., Bayo, A., Carraro, G., Costado, M. T., Damiani, F., Edvardsson, B., Hourihane, A., Jackson, R., Lewis, J., Lind, K., Marconi, G., Martayan, C., Monaco, L., Morbidelli, L., Prisinzano, L., and Zaggia, S.: 2014, *A&A* **570**, A122
- Snedden, C. A.: 1973, *Ph.D. thesis*, THE UNIVERSITY OF TEXAS AT AUSTIN.
- Snellen, I. A. G., de Kok, R. J., le Poole, R., Brogi, M., and Birkby, J.: 2013, *ApJ* **764**, 182
- Soubiran, C., Le Campion, J.-F., Brouillet, N., and Chemin, L.: 2016, *A&A* **591**, A118
- Sousa, S. G., Fernandes, J., Israelian, G., and Santos, N. C.: 2010, *A&A* **512**, L5
- Sousa, S. G., Santos, N. C., Adibekyan, V., Delgado-Mena, E., and Israelian, G.: 2015, *A&A* **577**, A67
- Sousa, S. G., Santos, N. C., Israelian, G., Mayor, M., and Monteiro, M. J. P. F. G.: 2007, *A&A* **469**, 783
- Sousa, S. G., Santos, N. C., Israelian, G., Mayor, M., and Udry, S.: 2011, *A&A* **533**, A141
- Sousa, S. G., Santos, N. C., Mayor, M., Udry, S., Casagrande, L., Israelian, G., Pepe, F., Queloz, D., and Monteiro, M. J. P. F. G.: 2008, *A&A* **487**, 373
- Takeda, Y. and Kawanomoto, S.: 2005, *PASJ* **57**, 45
- Takeda, Y., Sato, B., and Murata, D.: 2008, *PASJ* **60**, 781
- Thiabaud, A., Marboeuf, U., Alibert, Y., Cabral, N., Laya, I., and Mezger, K.: 2014, *A&A* **562**, A27
- Torres, G., Andersen, J., and Giménez, A.: 2010, *Astronomy and Astrophysics Reviews* **18**, 67
- Torres, G., Winn, J. N., and Holman, M. J.: 2008, *ApJ* **677**, 1324

- Triaud, A. H. M. J., Collier Cameron, A., Queloz, D., Anderson, D. R., Gillon, M., Hebb, L., Hellier, C., Loeillet, B., Maxted, P. F. L., Mayor, M., Pepe, F., Pollacco, D., Ségransan, D., Smalley, B., Udry, S., West, R. G., and Wheatley, P. J.: 2010, *A&A* **524**, A25
- Tsantaki, M., Andreasen, D. T., Teixeira, G. D. C., Sousa, S. G., Santos, N. C., Delgado-Mena, E., and Bruzual, G.: 2017, *MNRAS* **555**, A150
- Tsantaki, M., Sousa, S. G., Adibekyan, V. Z., Santos, N. C., Mortier, A., and Israelian, G.: 2013, *A&A* **555**, A150
- Valenti, J. A. and Fischer, D. A.: 2005, *ApJS* **159**, 141
- Valenti, J. A. and Piskunov, N.: 1996, *A&A Supp.* **118**, 595
- Vanderburg, A., Montet, B. T., Johnson, J. A., Buchhave, L. A., Zeng, L., Pepe, F., Collier Cameron, A., Latham, D. W., Molinari, E., Udry, S., Lovis, C., Matthews, J. M., Cameron, C., Law, N., Bowler, B. P., Angus, R., Baranec, C., Bieryla, A., Boschin, W., Charbonneau, D., Cosentino, R., Dumusque, X., Figueira, P., Guenther, D. B., Harutyunyan, A., Hellier, C., Kuschnig, R., Lopez-Morales, M., Mayor, M., Micela, G., Moffat, A. F. J., Pedani, M., Phillips, D. F., Piotto, G., Pollacco, D., Queloz, D., Rice, K., Riddle, R., Rowe, J. F., Rucinski, S. M., Sasselov, D., Ségransan, D., Sozzetti, A., Szentgyorgyi, A., Watson, C., and Weiss, W. W.: 2015, *ApJ* **800**, 59
- Vigan, A., Bonnefoy, M., Ginski, C., Beust, H., Galicher, R., Janson, M., Baudino, J.-L., Buenzli, E., Hagelberg, J., D'Orazi, V., Desidera, S., Maire, A.-L., Gratton, R., Sauvage, J.-F., Chauvin, G., Thalmann, C., Malo, L., Salter, G., Zurlo, A., Antichi, J., Baruffolo, A., Baudoz, P., Blanchard, P., Boccaletti, A., Beuzit, J.-L., Carle, M., Claudi, R., Costille, A., Delboulbé, A., Dohlen, K., Dominik, C., Feldt, M., Fusco, T., Gluck, L., Girard, J., Giro, E., Gry, C., Henning, T., Hubin, N., Hugot, E., Jaquet, M., Kasper, M., Lagrange, A.-M., Langlois, M., Le Mignant, D., Llored, M., Madec, F., Martinez, P., Mawet, D., Mesa, D., Milli, J., Mouillet, D., Moulin, T., Moutou, C., Origné, A., Pavlov, A., Perret, D., Petit, C., Pragt, J., Puget, P., Rabou, P., Rochat, S., Roelfsema, R., Salasnich, B., Schmid, H.-M., Sevin, A., Siebenmorgen, R., Smette, A., Stadler, E., Suarez, M., Turatto, M., Udry, S., Vakili, F., Wahhaj, Z., Weber, L., and Wildi, F.: 2016, *A&A* **587**, A55
- Wang, J. and Fischer, D. A.: 2015, *AJ* **149**, 14
- West, R. G., Hellier, C., Almenara, J.-M., Anderson, D. R., Barros, S. C. C., Bouchy, F., Brown, D. J. A., Collier Cameron, A., Deleuil, M., Delrez, L., Doyle, A. P., Faedi, F., Fumel, A., Gillon, M., Gómez Maqueo Chew, Y., Hébrard, G., Jehin, E., Lendl, M., Maxted, P. F. L., Pepe, F., Pollacco, D., Queloz, D., Ségransan, D., Smalley, B., Smith, A. M. S., Southworth, J., Triaud, A. H. M. J., and Udry, S.: 2016, *A&A* **585**, A126
- Wilson, P. A., Hébrard, G., Santos, N. C., Sahlmann, J., Montagnier, G., Astudillo-Defru, N., Boisse, I., Bouchy, F., Rey, J., Arnold, L., Bonfils, X., Bourrier, V., Courcol, B., Deleuil, M., Delfosse, X., Díaz, R. F., Ehrenreich, D., Forveille, T., Moutou, C., Pepe, F., Santerne, A., Ségransan, D., and Udry, S.: 2016, *A&A* **588**, A144
- Winn, J. N., Noyes, R. W., Holman, M. J., Charbonneau, D., Ohta, Y., Taruya, A., Suto, Y., Narita, N., Turner, E. L., Johnson, J. A., Marcy, G. W., Butler, R. P., and Vogt, S. S.: 2005, *ApJ* **631**, 1215

Wolszczan, A. and Frail, D. A.: 1992, *Nature* **355**, 145

Zhou, G., Bayliss, D., Penev, K., Bakos, G. Á., Hartman, J. D., Jordán, A., Mancini, L., Mohler, M., Csubry, Z., Ciceri, S., Brahm, R., Rabus, M., Buchhave, L., Henning, T., Suc, V., Espinoza, N., Béky, B., Noyes, R. W., Schmidt, B., Butler, R. P., Shectman, S., Thompson, I., Crane, J., Sato, B., Csák, B., Lázár, J., Papp, I., Sári, P., and Nikolov, N.: 2014, *AJ* **147**, 144

Zhu, W., Wang, J., and Huang, C.: 2016, *ApJ* **832**, 196

Zieliński, P., Niedzielski, A., Wolszczan, A., Adamów, M., and Nowak, G.: 2012, *A&A* **547**, A91

Zurlo, A., Vigan, A., Galicher, R., Maire, A.-L., Mesa, D., Gratton, R., Chauvin, G., Kasper, M., Moutou, C., Bonnefoy, M., Desidera, S., Abe, L., Apai, D., Baruffolo, A., Baudoz, P., Baudrand, J., Beuzit, J.-L., Blancard, P., Boccaletti, A., Cantalloube, F., Carle, M., Cascone, E., Charton, J., Claudi, R. U., Costille, A., de Caprio, V., Dohlen, K., Dominik, C., Fantinel, D., Feautrier, P., Feldt, M., Fusco, T., Gigan, P., Girard, J. H., Gisler, D., Gluck, L., Gry, C., Henning, T., Hugot, E., Janson, M., Jaquet, M., Lagrange, A.-M., Langlois, M., Llored, M., Madec, F., Magnard, Y., Martinez, P., Maurel, D., Mawet, D., Meyer, M. R., Milli, J., Moeller-Nilsson, O., Mouillet, D., Origné, A., Pavlov, A., Petit, C., Puget, P., Quanz, S. P., Rabou, P., Ramos, J., Rousset, G., Roux, A., Salasnich, B., Salter, G., Sauvage, J.-F., Schmid, H. M., Soenke, C., Stadler, E., Suarez, M., Turatto, M., Udry, S., Vakili, F., Wahhaj, Z., Wildi, F., and Antichi, J.: 2016, *A&A* **587**, A57